DATE DUE	DATE DUE	DATE DUE
122		

ADHERENCE OF DIAMOND THIN FILMS ON SILICON WAFERS AND FTIR SPECTROSCOPY OF DAMAGED CERAMIC MATERIALS

By

Carol Ann Gamlen

A THESIS

Submitted to
Michigan State University
in partial fulfillment of the requirements
for the degree of

MASTER OF SCIENCE

Department of Metallurgy, Mechanics,
and Materials Science

November 1990

ABSTRACT

ADHERENCE OF DIAMOND THIN FILMS ON SILICON WAFERS AND FTIR SPECTROSCOPY OF DAMAGED CERAMIC MATERIALS

By

Carol Ann Gamlen

Adherence of diamond thin films to silicon substrates was investigated and properties which will improve the adhesion of the films were determined. Also, the Fourier Transform Infrared (FTIR) Spectrophotometer was developed as a nondestructive tool to characterize the damage in ceramic materials.

Vicker's indentation was used to induce delaminations on diamond thin film silicon wafers produced in a microwave plasma disk source reactor. Grain size and thickness of the coating were determined by the SEM. Grain size of the coatings exhibited the most significant influence on the adherence. Adherence of the film improved as the grain size decreased.

Infrared scattering from an air gap in a transmitting medium was the model used to theoretically determine the crack opening displacement in a Vicker's indented silicon specimen. Theoretical and experimental values of crack opening displacement were in good agreement.

DEDICATION

To my mother,

Lois V. Weiland-Gamlen.

ACKNOWLEDGEMENTS

I would like to thank Dr. Eldon Case for his guidance and assistance in this project. From the Electrical Engineering Department, I would like to thank Dr. Reinhard for his advice on the diamond thin film specimens.

Special thanks goes to Youngman Kim for his plotting expertise.

I would also like to thank my fellow researchers Mehmet Ali Gulgun, Subrato Dhar, Narendra Bettedpur, Chin Chen Chui, Karl Tebeau, Bohr-ran Huang, and Won Jae Lee for their assistance.

TABLE OF CONTENTS

List of Tables

List of Figures

1.0 Introduction

Diamond, a crystalline form of carbon, consists of a tetrahedral structure of carbon atoms. It's unique combination of electrical, optical, and physical properties have caused a great interest in the material [1]. A wide variety of applications exist for diamond coatings in military, industrial, and commercial markets due to it's unique properties [2].

In table 1, various properties of diamond are listed. The bond energy per unit volume in diamond is high since the radius of the carbon atoms is small (0.77 Angstroms) [3]. This high bond energy is responsible for the high value of hardness that diamond posesses. The high elastic modulus of the material is also a result of the strong covalent bonding and high atom-number density [4]. It is described as the least compressible substance known. A few other of it's superior qualities are it's high thermal conductivity, chemical inertness, and high electrical resistivity [1,5]. Diamond's thermal conductivity is five times greater than that of copper. Diamond is one of the rare materials that is both an electrical insulator and a thermal conductor.

Table 1. Properties of diamond [3,5,6].

Property	Diamond
crystal structure	cubic, a=0.3567 nm
density	3.51 g/cm^3
chemical stability	inert, inorganic acids
hardness (Vicker's)	7000-10000 Kg/mm^2
Young's modulus	1160 GN m^{-2}
thermal conductivity	900-2600 $Wm^{-1}K^{-1}$ at 293 K
refractive index:	
at 656.3 nm	2.41
at 226.5 nm	2.72
transparency	UV, VIS, IR
optical gap (ev)	5.5
resistivity (ohm-cm)	$>10^{16}$
dielectric constant	5.7
dielectric strength	$>10^{12}$ n/cm

1.1 Diamond Thin Film Coatings

Diamond's unique properties qualify the material for numerous applications in the form of a coating or thin film. Tribologically, since diamond is corrsion resistant, wear resistant, chemically inert, and hard it is a good choice for wear resistant coating on cutting tools [5]. High density computer disks could use very thin diamond films as impact resistant coatings. As a wear resistant coating valves, pistons, and bearings may also be coated with a diamond thin film [1].

Optical windows which are made from zinc selinide, germanium, and zinc sulfate are soft and can be easily damaged by rain and ice particles. Pits form on zinc selenide when it is impacted. The heat generated in supersonic flights also causes distortion in germanium. These problems may be reduced by coating the windows with diamond. At hypersonic speeds impact, diamond is not affected by rain or ice [1]. It is also transparent in the infrared. Optically, diamond coatings may be utilized as antireflective coatings on Ge and Si [2].

In the electronics industry diamond films have the potential to be used as heat sinks [1,2,5]. This would enable a denser integrated circuit to be produced, since currently circuit density is limited by the heat generated. The high electrical resistivity and high thermal conductivity

of diamond enables it to be used as a thin insulating layer in a high power semiconductor. At the present, avionics of missiles and aircrafts are cooled by refrigeration systems. If the refrigeration systems were replaced by diamond heat sinks, weight would be reduced and the design would be simplified. Diamond thin films can also be used as a protective layer on electronic devices.

Compared to silicon, diamond can withstand more heat and electrical power [1]. Diamond's band gap of 5.45 ev allows it to be used in a high energy electrical system without leakage or failure. Silicon, having a band gap of 1.3 ev, will fail or leak when a high amount of energy is passed through it since the electrons can be promoted through the small band gap..

Although the list of applications for diamond thin films is long, they have not been used to their full extent to this time due to some problems that need to be addressed. Compressive stresses, surface smoothness, and adhesion limit the use of the diamond films [7]. In this investigation the adhesion of a diamond thin film to a silicon substrate is studied.

1.1.1 History of Diamond Synthesis

In 1955 General Electric successfully produced diamonds under high pressure and high temperature (HPHT) conditions in

the diamond stable region [7]. The procedure used by General Electric started with nondiamond carbons [4]. The HPHT method is very successful and is used around the world. Each year a few tons of diamond abrasive grain is produced by the HPHT procedure [7].

Growth of diamond thin films is accomplished under metastable conditions, in the graphite stable region [7]. Under ambient conditions the small free energy difference between graphite and diamond (500 cal/mole) enables diamond to form in the graphite stable region [7]. With sufficiently high activation barriors to the graphite stable phase, precursors with high chemical potential are used to form the metastable diamond phase [4]. The precursors are held in a metstable configuration as their energy decreases. At least three decades of research have been conducted on the synthesis of metastable diamond in order to determine appropriate processing conditions. The conditions must be determined such that the rate of formation of the stable phase is low [8].

W.G. Eversole, in 1949, was the first person to successfully grow diamond at low pressures [4]. Eversole, at the Union Carbide Company, grew diamond on diamond seed crystals. His method was slow and not very practical, but was reproduced by Angus and co-workers at Case Western Reserve University [9]. Angus was unable to improve on the low growth rate of .001 μm/hr, which Eversole obtained. The

process used by Eversole and Angus involved two different steps. First a layer with a small amount of diamond bonds (<1 percent) was produced. Then a selective hydrogen reduction process was used to remove the large amount of graphitically bonded material. This process was repeated several times to form a thick enough film for analysis. A 59.5 weight percent increase required 85 repitions [7].

The longest continued research on the growth of diamond in the metastable region has been conducted by Deryagin of the Soviet Union, which started in 1956 [4,9]. He studied the epitaxial growth of diamonds from hydrocarbon-hydrogen mixtures and hydrocarbons. He also investigated various kinds of vapor transport reactions. The ability of atomic hydrogen to act as a selective etchant in order to remove graphite and not diamond, was observed by Deryagin [9]. Graphite that formed during depostion was continuously removed by atomic hydrogen. The equilibrium concentration of atomic hydrogen related to the thermal dissociation of hydrocarbon-hydrogen gases was too low to accelerate diamond growth. Therefore higher concentrations of atomic hydrogen were used to accelerate diamond growth.

Hydrogen played an important part in the early research on the growth of metastable diamond. Hydrogen may stabilize sp^3 bonds of carbon [7]. Lander and Morrison conducted a low energy electron diffraction study which exhibited a unreconstructed LEED pattern from a (111) diamond surface

[4]. Hydrogen atoms were connected to the dangling bonds normal to the surface. The hydrogen atoms maintain the integrity of the lattice and in their absence the surface reconstructs into more complex structures. As compared to the growth rate of diamond, graphite's growth rate is decreased much more with the addition of hydrogen. Using hydrogen additions, several researchers have therefore been able to increase the amount of diamond produced [4]. In 1974, the growth of diamond at a rate of several micrometers per hour was achieved by Matsumoto, Setaka, and co-workers at the National Institute of Research in Inorganic materials in Japan [10]. During the growth, atomic hydrogen was near the surface that the film was grown on.

1.1.2 Current Deposition Techniques

Many different processes have become established in the growth of metastable diamond. The processes can be grouped into three general categories: chemical vapor deposition process (CVD), plasma assisted chemical vapor deposition process (PACVD), and ion beam deposition process [5].

The chemical vapor deposition process can be subdivided into the following categories: electron assisted chemical vapor deposition (EACVD), hot filament thermal chemical vapor deposition, and chemical transport method. Deryagin and co-workers were the first to use the chemical transport process

[11]. The hot filament thermal CVD process was just a modification of the chemical transport method [12]. In this method a hot tungsten filament is placed near the substrate and a mixture of methane and hydrogen gas is used. The hot filament heats the substrate and eases the dissociation of the hydrocarbon. The increase in the diamond film growth rate with this technique is related to the improved dissociation of the hydrocarbon. A hot filament thermal CVD is used in the set up of the EACVD process. With respect to the hot filament the substrate is biased as positve, which allows the electrons to bombard the substrate surface. High growth rates were obtained with this method (5-10 μm/hr), but the UV and optical transmision of these films was low. This limits the optical and electronic applications.

Microwave, direct current, or radio frequency excitation may be used in the PACVD technique. In this technique the hydrocarbon gas is decomposed in the plasma. The microwave plasma assisted CVD produces rough and transparent diamond thin films. The rate of deposition is low with this method and a high deposition temperature is required.

The ion beam sputtering technique produces smooth transparent films on a variety of materials including silicon. Two disadvantages of this technique are the fact that only a small area can be deposited and the rate of deposition is low. Dual ion beam sputtering has also been used but it mainly produces diamondlike carbon films with the

same disadvantages as the single ion beam technique. Both magnetron and rf sputtering have also been tried, but were not very successful [5]. Magnetron sputtering did not succeed due to negligible substrate bombardment. The rf sputtering technique was restricted by the substrate overheating.

1.1.3 Nucleation and Morphology of Synthetic Diamond

To the present most the research on the growth of metastable diamond involved the nucleation of diamond on a solid surface [13]. In order to produce a film with little or no gaps (continuous coating), the nucleation density was increased by pretreating the surface of the solid. Without pretreatment diamond growth is slow and nucleation density is low. Various methods of pretreatment have been used such as polishing the surface with diamond paste or powder, placing the substrate in an ultrasound tank with diamond powder, or coating the substrate with diamondlike carbon [14,15,16]. Mo, WC, and Si substrates exhibited a high nucleation density of 10^8 sites/cm^2 when pretreated with a diamond powder polishing [14]. One theory developed by Yugo and Kimura [17] for this increase in nucleation density is that many high energy sites are created, from the damage to the substrates, that act as nucleation sites. Some researchers also believe that residues from the pretreatment act as nucleation sites

for the diamond [18].

Mitsuda, et al. [19] enhanced nucleation of diamond via surface pretreatment. A microwave plasma CVD system deposited diamond on the (100) surface of a silicon substrate placed on a boron nitride holder. An optical pyrometer measured the substrate temperature. Before deposition, fine uniform scratches were made on the surface of the substrate by a mechanical vibration technique. The Si was attached to the bottom of a container and 30 g of a particular size of SiC grit was added, (the SiC grit sizes ranged from 100 grit to 2000 grit). The container was then sealed and put in a mechanical vibrator for one hour. The temperature of the substrate during deposition ranged from 1000-1400 K for an unscratched specimen and was 1170 K for the scratched specimen. Deposition on the scratched specimen resulted in a greater density of diamond particles than on the unscratched specimen. The specimen scratched with size 1000 grit SiC powder exhibited the highest nucleation density. The specimens treated with a SiC powder size which was coarser or finer than 1000 exhibited a lower nucleation density. Using electron microscopy to view the surface of the substrate before pretreatment, after pretreatment, and after deposition, the high density distribution was determined to be caused by the surface crystal defects.

Another important aspect of the investigation was that a specimen that was polished with 1000 grit SiC was placed in

the microwave plasma CVD system for twenty hours [19]. Diamond particles approximately ten microns in diameter were deposited on the silicon. The film was about fifteen microns thick. When a diamond cutter was used on the specimen, the film was easily removed. The poor adhesion of the film could have been caused by the growth mechanism [19] since the number of contact points between the substrate and film were low. Each diamond grain contacted the silicon only at the vertex of a single crystal. In the early stage of deposition the growth rate of diamond is faster in diameter than it's vertical growth. Growth of the diamond vertical to the substrate occurs in the next stage. Mitsuda, et al. [19] suggests that an increase in the number of contact points would result in improved adhesion of the film. This could be accomplished by increasing the pretreatment vibration time to increase the number of nucleation sites and produce a finer grain film.

Kawarda, et. al [20] used a scanning electron microscope to study the morphology of diamond particles deposited in a magneto-microwave plasma and typical microwave plasma system. Diamond was depsited on (100) Si substrates with CH_4 molar concentrations ranging from 0.3-2.0 percent. Substrate temperatures ranged from 850-900^{o}C. The diamond particles grown in the microwave plasma CVD at 900^{o}C exhibited {100} facets. At 850^{o}C the diamond particles grown in the magneto-microwave plasma CVD exhibited flat {111} facets. The

deposition system, concentration of the methane, and substrate temperature were determined to be the conditions which controlled the morphology.

Williams and Glass [21] also used the scanning electron microscope to investigate the surface morphology of diamond particles grown in a microwave plasma enhanced CVD system. At about 800^{o}C the diamond was deposited on 2 cm x 1 cm n-type Si (111) surfaces. The CH_4/H_2 ratio ranged from 0.2-3.0 percent. Surfaces were pretreated with a 0.25 micron diamond paste polish for one hour. The 1.0 percent CH_4/H_2 sample exhibited a large change in surface morphology in relation to the location on the substrate. A highly faceted polycrystalline film was present at the center of the specimen, but at 2.5 mm away from the edge the diamond became less faceted. Here, behind the faceted particles, microcrystalline and cauliflower type particles were observed. As the field of view was moved to within 0.5 mm of the edge, only the cauliflower type texture was present. Raman spectroscopy indicates that sp^2 bonds are more frequent in the cauliflower texture than in the microcrystalline regions. Williams and Glass [21] conclude that the change in surface morphology was the result of variation in temperature across the specimen. The surface morphology of the diamond film was also affected by the methane concentration used. On the 1.0 and 2.0 percent CH_4/H_2 specimens, fourfold {100} facets dominated. Threefold {111} facets were dominant on

the 0.3 percent CH_4/H_2 specimens.

1.1.4 Methods of Diamond Identification.

Many different instruments have been used to determine if the film grown in one of the previously discussed processes is actually diamond. One of the most widely used nondestructive tools is Raman spectroscopy [22]. Diamond, amorphous carbon, and other related carbons are all strong Raman scatters. Cubic diamond can be identified in a large amount of graphitic carbon by sharp Raman lines. The graphitic carbon can also be characterized by Raman spectroscopy. Diamond exhibits a single sharp line at 1332 cm^{-1} [22], representing the first order band. A sharp band at 1580 cm^{-1} [22] indicates the presence of single crystal graphite. Single crystal graphite exhibits a Raman line at 1357 cm^{-1} if the particle size is small. Broad bands are typical of diamond-like carbon spectra.

Some researchers believe that testing the film with only Raman spectroscopy is not enough to accurately identify it as diamond. Matsumoto, et. al [10] used Raman spectroscopy and the reflection electron diffraction pattern of the film to characterize it as diamond. Matsui [23] argued that the film could not be labled as diamond until the ions which formed the film were determined to be carbon. Matsui suggests that the transmission electron microscope with the electron energy

loss spectrometer (EELS) or the energy dispersive x-ray spectrometer (EDX) could be used to determine if the ions were carbon. The films in question were then tested with the EELS and the EDX. Hydrofluoric acid dissolved the Si away from the coating. The particles deposited were verified as carbon with EELS and EDX.

Williams and Glass [21] included many different methods of testing the film to determine if it was cubic diamond. Composition of the film was found using Auger electron spectroscopy (AES) and secondary ion mass spectrometry (SIMS). AES and Raman Spectroscopy investigated the type of bonding in the film. Crystal structure and lattice spacing was studied with x-ray diffraction snd transmission electron diffraction.

Vitkavage, et. al [24] also concluded that diamond films had been deposited by plasma enhanced chemical vapor deposition. One method used for the diamond identification in this study was reflection high-energy electron diffraction. The ring pattern resulting from this method was sharper for specimens processed at higher temperatures. Chemical bonding of the film was investigated by x-ray photoelectron spectroscopy. Raman spectroscopy and EELS were also performed on the specimen in order to verify that the film was diamond.

1.1.5 Gas Compositions.

Most of the deposition processes being used today use a gas mixture of methane and hydrogen. As discussed by Setaka [25] the hydrogen is converted into atomic hydrogen by electric or thermal energy and is used to etch away the non-diamond carbon. Setaka measured the rate of consumption of vitreous carbon, natural diamond, and artificial graphite in hydrogen plasma. The consumption rate of artificial graphite and vitreous carbon was much higher than diamond. Since diamond growth is performed in the graphite stable region, both diamond and non-diamond particles may deposit at the same time. Hydrogen is used to etch away the non-diamond deposits.

Celii, et. al [26] used infrared absorption spectroscopy to determine the gas phases present during diamond deposition. Filament assisted CVD was used to grow the diamond on Si and Ni substrates. CH_4/H_2 ranged from 0.3 percent to 1.0 percent and the substrates were heated to 800-900^{o}C in the system. Above the substrate CH_3, C_2H_2, and C_2H_4 were detected during processing. Of these phases detected, acetylene (C_2H_2) was the predominate gas. Proposals have been made for the use of acetylene in diamond synthesis [27].

The effect of adding O_2 to the hydrogen and methane mixture was investigated by Chen, et. al [28]. The microwave

plasma CVD process was used to deposit diamond on Si substrates. As O_2 was added to the system in varying amounts the deposition rate was affected. A critical amount of O_2 produced a maximum deposition rate. Below or above this amount the rate of deposition decreased. The maximum rate of deposition occurred between 11 and 22 percent O_2/CH_4 for CH_4/H_2 concentrations between 3 and 9 percent. These ratios are relavent for the H_2 flow of 1.67 cm^3/s. The small addtion of O_2 was also found to improve the crystallinity of the deposited diamond and allow higher concentrations of methane to be used.

1.1.6 Adhesion of the Coating.

According to Valli [29], the most important property of a coating is it's ability to adhere to the substrate. There are a wide varity of techniques that have been used to test the adhesion of coatings. Today, physical and chemical vapor deposition is used to produce films with adhesion levels that were unthought of in the past. This increase in adhesion limits the number of tests that can be applied. Adhesion testing methods include acceleration testing, scratch testing, laser techniques, acoustic imaging, indentation tests, tape tests, shock wave testing, tensile testing, and electromagnetic stressing [29]. Further development to

standardize these testing techniques is needed in order to increase the use of the well adhered coatings. Adhesion tests should be quick and easy. All adhesion test methods which exist involve the measurement of coating, interface, or substrate properties which affect the adhesion of the coating.

A rough method of adhesion testing is the tape test [29]. This test is limited by the connection between the tape and the coating. It is therefore used only when the coating is soft or the adhesion is poor. To determine the adherence a pressure sensitive tape is applied to a coating and pulled off. Many techniques of adhesion testintg involve the use of a bond to a coating and the application of a force to pull off the coating. These techniques are limited by the fact that the maximum adhesion measurable has to be less than the strength of the bonding agent which is usually an epoxy [29]. Also the interface between the film and the substrate may be affected by the bonding agent if it penetrates the coating.

Acceleration and deceleration forces have been used to measure the adhesion of a coating to a substrate [29]. One example, the ultracentrifugal method, invólves the rotation of a small coated rotar in a vacuum at a continuously increasing speed until coating detachment occurs. Forces on the film at the moment of decohesion are calculated. This method is limited in the fact that various components cannot

be used.

A nondestructive technique used to determine coating adhesion is acoustic imaging [29,30]. In an acoustic microscope an acoustic plane wave is produced by a piezoelectric transducer when activated by a short radio frequency pulse. A lens is used to focus the wave. After being reflected the sound pulse passes through the lens and is picked up by the transducer which produces an electric signal.

An increasing number of techniques have been developed which involve the use of lasers in order to produce or detect delamination [29]. The advantages of lasers are that they can produce a thermal gradient that is representative of real operating conditions for coatings and they are nondestructive on coatings that have a strong adherence. Loh, Rossington, and Evans [31] have used the laser to determine the spall resistance of brittle coatings. Useful properties of a coating are removed during spallation because it locally exposess the substrate. The steps involved in spalling of a coating include: initial delamination, buckling, further crack propagation, and spalling. Spalling is completed in a specimen when the interface crack is deflected through the coating to the surface. Void formation or contamination in the coating or interface causes the initial delamination. Defective regions of the coating were heated with a laser to induce spalling. Compressive stresses produced by the laser

heating result in spallation of the coating. In the investigation [31] a control method of indention testing was used. The specimens tested were Y_2O_3-stablized ZrO_2 coatings on a Ni-based superalloy. The CO_2 laser used in this investigation produced spallation only where an initial delamination was produced by indentation. Successful spallation only occurred if the initial delamination diameter was greater than 250 microns.

The scratch test for adhesion is based on the indentation test [29]. In this method under increasing normal load the indenter is pulled across the surface of the coating. Indentaion generates a sufficiently high stress in order to break the bond between the coating and the substrate. The critical normal force is that which causes the coating to de-adhere from the substrate. This value is used as a measure of adhesion. Detachment of the coating is then observed by scanning electron microscopy, optical micoscopy, accoustic emission, and friction force measurements. Data acquired from scratch tests have typical standard deviations of 10-20 percent of the mean. Coating thickness and hardness, substrate hardness, suface roughness, loading rate, and indenter tip radius are all factors in the determination of the critical normal force. It is important to note that a high surface roughness will cause a loss in reproducible results of the scatch test. Burnett and Rickerby [32] used the scratch test on pysical vapor

deposited TiN coatings on steel substrates. The critical load measured [32] depended on interfacial adhesion, type of substrate, and thickness.

Scaglione and Emiliani [33] used the scratch test to determine the adhesion of 2.0 micron thick amorphous carbon films deposited by dual ion beam sputtering onto silicon and silica glass substrates. When the coated silicon substrates were tested failure occured at small tip loads of 4 N. The scratch test is therefore not applicable to these specimens. Results were obtained from the coated glass substrates. A critical load of 11 N was determined.

According to Clarke and Wolf [34] nondestructive techniques to measure adhesion cannot be applied usefully until the nature of flaws which cause adhesion failure are determined. Failure of adhesion initiates and grows at a flaw since the stress required to separate an interface is less than the bonding force of the interface. Adhesion failure is considered to be a fracture phenomenon. Due to the variety of flaw sizes, adhesion measurements have a large variability. To avoid this problem Clarke and Wolf suggest that controlled and reproducible indentation induced flaws should be used in measurements of adherence.

Argon, et al. [35], reported that changes in interface adhesion can be monitored by a measurement of interface toughness during spontaneous delamination testing. When SiC coatings on Si substrates exceed a critical value of

thickness and contain residual tensile or compressive stress, spontaneous delamination occurs starting at the defects. The driving force for delamination is the elastic strain energy of the material misfit in the coating. Plasma assisted CVD was used to deposit the SiC coatings on to (100) surfaces of single crystal Si. After deposition a large amount of hydrogen was found in the coating which produced biaxial residual compressive stresses. Outgassing treatments of 600^{o}C were carried out on some of the specimens in order to remove the hydrogen. These specimens then developed residual tensile stresses. The change in curvature of the silicon wafer after deposition was measured, using a Dektak II profilometer, and the following equation was used to determine the residual compressive stress:

$$\sigma = (E_s h^2)/[6(1-\nu_s)tR] \qquad (1)$$

where E_s = Young's modulus of the substrate

ν_s = Poisson's ratio of the substrate

h = substrate thickness

t = coating thickness

R = spherical radius of curvature

For all levels of residual stress measured, the coatings with submicron thickness did not delaminate from the substrate. The driving force for delamination increased almost linearly

with thickness. The critical thickness value for delamination was different for coatings in tension and compression. The time that elapsed before delamination decreased, as the thickness increased. Spontaneous delamination of the coating under tensile stress occured when the elastic strain energy per unit area, which increased with thickness, was equal to the critical energy release rate. G_{co}, the critical energy release rate is given by:

$$G_{co} = [\sigma^2(1-\nu)t_c]/E \qquad (2)$$

where σ = biaxial residual tensile stress

ν = Poisson's ratio of the coating

t_c = critical coating thickness

E = Young's modulus of the coating

The critical energy release rate is also called the intrinsic interface toughness. Values of the critical energy release rate were slightly higher for the coatings in compression than those in tension [36]. Indicating that coatings in compression slipped with respect to the substrate before decohesion.

Hu, et al. [37], also agree that coatings under residual stress are likely to de-adhere from the substrate. They state that the flaw distributions near the interface, fracture resistance of the substrate and interface, amount of

residual stress, and the film thickness all play a role in the film's susceptibility to de-adhere. In this experiment electron beam evaporation was used to deposit Cr films on glass disks. A surface profiler measured the residual stress in the coatings. The relative humidity exhibited a strong influence on the rate of decohesion (velocity of crack propagation). The rate of decohesion was observed at 10 percent, 55 percent, and 100 percent relative humidity for approximately 800 nm thick Cr films. As the relative humidity increased the rate of decohesion, velocity of the crack, also increased. Coatings larger than 650 nm in thickness broke their adhesive bond by edge splitting of the film, initial decohesion of the interface, and cracking of the substrate parallel to the interface.

Evans, Drory, and Hu [38] used a nondimensional parameter governed by film thickness, fracture resistance, and residual stress to charaterize the decohesion and cracking of thin films. The critical nondimensional parameter is given by [38]:

$$\Omega_c = K_c/(\sigma_o/h^{1/2}) \qquad (3)$$

where K_c = fracture resistance

σ_o = the stress in the film

h = film thickness

Ω is referred to as the decohesion number. The elastic moduli, ductility of the film and substrate, and residual stress all affect the values of Ω_c and and K_c. Cr films on glass were observed in this experiment [38]. Film decohesion often occurred with substrate cracking when the films were in residual tension. The path of the crack is determined by the plane at which the phase angle of loading is equal to zero. This plane is a function of substrate thickness. Buckling and spallation were the forms of decoherence exhibited by the films in residual compression.

During the deposition process residual stresses are often induced into the film. After delamination, Marshall and Evans [39] state that buckling of the film above the indentation crack occurs due to the presence of residual deposition stresses. An additional crack driving force is then acquired from these stresses. The delamination of a film from a substrate is charaterized as a brittle fracture. Therefore, both a strength parameter and a fracture resistance parameter are needed in order to fully describe the adhesion of a film to a substrate. Marshall and Evans have investigated the fracture of indentation induced delaminations using a point loaded rigidly clamped disc model for the segment of film above the delamination crack. During indentation, lateral cracks propagate along the interface. If buckling of the film occurs at the delamination then strain energy is released as the crack

advances, thereby decreasing the energy of the system. Residually stressed films that buckle have a higher crack extension force than those that do not, and exhibit an increase in the delamination crack velocity with indentation load.

Rossington and Evans, et al. [40] used the indentation induced delamination technique on ZnO coated Si substrates containing a 0.1 micron thick intermediate layer of SiO_2. Reactive magnetron sputtering was used to deposit the ZnO coatings ranging from five to ten microns in thickness. In the residually stressed films the indentation load and the thickness of the film determined the path of the indentation induced lateral cracks relative to the interface. For the 10 micron thick films subject to loads from 1-15 N and for five micron thick films subject to loads greater than 3 N, cracks occurred in the film adjacent to the interface. Cracks along the film/substrate interface were exhibited in the five micron thick films which were under indentation loads of 1-3 N. The cracks existed at two different positions, at the interface and adjacent to the interface, due to buckling of the film. Buckling results in the deflection of the interface crack towards the surface. This investigation also used the following equation to estimate the interface fracture toughness:

$$G_c = [\sigma_R^2 (1-\alpha)(1-\nu)t]/(E^*R) \qquad (4)$$

where R = normalized residual deposition stress

α = a material constant (0.383)

ν = Poisson's ratio of the film

t = film thickness

E = Young's modulus of the film

σ_R = biaxial residual compression stress

Evans and Hutchinson [41] found that at interfaces between precompressed films and their substrates, shear and normal tensile stresses were not able to develop. In order for initial delamination of the film to occur, shear or normal tensile stress are required at the interface. Therefore a preexistent separation between the film and substrate is necessary for delamination to occur. Specimens formed by deposition techniques may contain initial separation due to contamination of the substrates surface.

Matthewson [42] investigated the adhesion of polyester coated glass blocks by using a steel sphere indenter. In the study the specimens did not exhibit interfacial cracking under large indentation loads until a critical load P_c was reached. The following equation is used to express P_c [42]:

$$P_c = H*\Pi*(a_c)^2 \qquad (5)$$

where H = hardness

a_c = contact radius

The failure of the bond seems to be therefore related to the crack initiation. After indentation the disc shaped region of film under the indenter often remained in contact with the substrate. The size of this region was approximately ten percent larger than the contact radius of the indenter.

1.2 FTIR Testing of Ceramic Materials.

Due to their brittleness, ceramic materials often encounter damage by contact or impact. The total damage sustained by a ceramic may be the result of many individual events. For example, single contact events may be used to produce the deformation and surface cracking that a ceramic undergoes during grinding. Also, the damage that rain drops cause on ceramic aircraft components may be produced by an accumulation of single impact events [43]. Point contact loading (Vicker's indention) and impact loading are both used to produce the damage suffered by ceramics in practical use.

The Fourier Transform Infrared Spectrophotometer is a tool which can be used to measure the transmittance in an infrared transparent material, as a function of wavelength. Previous studies [44] show that there is a loss in infrared transmittance for damaged materials. Two different models are used to describe the transmittance loss in specimens that have undergone point contact loading and impact loading. An air gap in a transmitting medium is used as a model of

scattering for specimens which have sustained point contact loading [45].

The scattering model used for transmittance loss due to impact damage is an inhomogeneous solid [46]. Applications of infrared transmitting materials include windows for missles, tanks, and aircrafts. These materials are also utilized in science instrumentation.

1.2.1 Transmittance and Reflectace of Electromagnetic waves, Including IR

Oscillations of electrons within atoms produce light waves which are characterized as propagating electromagnetic disturbances [47]. Maxwell developed the theory of the electromagnetic nature of light while calculating the speed of electromagnetic waves, such that, c, the speed of light in a vacuum is given by:

$$c = (\mu_o \epsilon_o)^{-1/2} \qquad (6)$$

where μ_o = permeability of free space

ϵ_o = permeativity of free space

Light waves are electromagnetic waves, and the measured speed of light agreed with Maxwell's calculation of the electromagnetic wave speed.

When an electromagnetic wave is incident on a solid, a reflected wave and a transmitted wave may result [48]. The wave transmitted into a second medium, changes velocity, which results in a direction change for the wave's motion. This is known as refraction. Snell's Law is used to determine the relative index of refraction:

$$n = v_1/v_2 = \sin\theta/\sin\phi \qquad (7)$$

where v_1 = speed of the wave in medium 1

v_2 = speed of the wave in medium 2

θ = angle of incidence of the wave

ϕ = angle between the refracted wave and the surface normal

The index of refraction for a particular medium, for example n_1, is calculated by:

$$n_1 = c/v_1 \qquad (8)$$

Where c is the speed of light in a vacuum. If θ is equal to the critical angle, θ_c, the incident wave will graze the surface of the second medium [49]. The value of the critical

angle is obtained from the following equation:

$$\sin\theta_c = n_2/n_1 \qquad (9)$$

Here n_2 is the index of refraction in the second medium. If the incident angle is less than the critical angle refraction will occur. When the incident angle is greater than the critical angle, total internal reflection will occur. This means that nothing is transmitted into the second medium.

When an electromagnetic wave is incident on a dielectric medium, such that the incident angle is zero, the portion of light reflected is described by [50]:

$$R = (n-1/n+1)^2 \qquad (10)$$

where R = reflectivity

n = index of refraction of the dielectric

The angle of incidence will be equal to the angle of reflection when light is incident on a smooth surface. This is known as specular reflection. In contrast to specular reflection, diffuse reflection will occur when light is incident on a rough surface.

1.2.2 Transmittance, Absorbence, and Reflectance in Layered Media

As illustrated in figure 1, light is incident on medium I having index of refraction n_1. The thickness of medium II, with index of refraction n_2, is given by d. Medium III also has index of refraction n_1. The wave having normal incidence on one edge of medium I is partially transmitted into medium III. The amount transmitted into medium III depends on the distance, d, between the first and third medium. This phenomenon is called frustrated total internal reflection [51].

If medium I and III are the same material and medium II (the gap of distance d between media I and III) is considered to be air, this can model a crack in a optically transmitting solid, such as a ceramic. It is therefore understood that a crack in a solid causes a decrease in transmittance, with respect to that of an undamaged solid of the same material, since only a fraction of the wave is transmitted into medium III.

The weakening in the intensity of electromagnetic radiation propagating through a solid may also result from absorption [52,53]. During absorption part of the incident electromagnetic radiation is transformed into a different form of electromagnetic energy. Factors which affect the amount of electromagnetic radiation absorbed include the

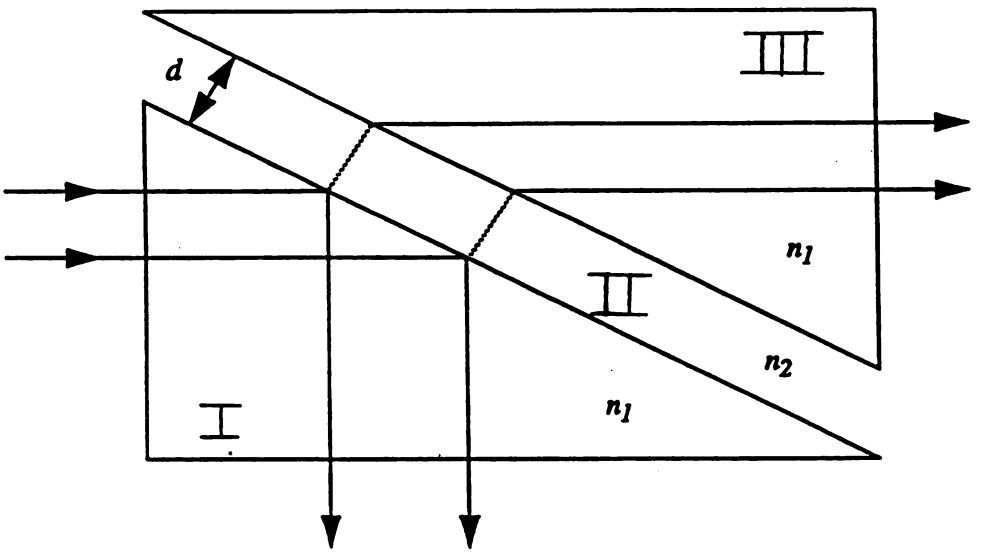

Figure 1. Frustrated total internal reflection [50].

density, thickness, and temperature of the solid. The wavelength of the incident radiation also affects the absorption. In a homogeneous solid the intensity, I, of an electromagnetic wave after travelling through thickness d of the solid, can be expressed as:

$$I = I_o \exp(-\alpha d) \qquad (11)$$

where I_o = the intensity of the incident radiation

α = the absorption coefficient

The fraction of the wave which is transmitted, T, is then expressed as:

$$T = I/I_o \qquad (12)$$

Molecules and atoms in an absorbing medium gain vibrational and rotational energy as the internal energy is increased during absorption of electromagnetic radiation.

1.2.3 Models Used to Describe the IR Transmittance of Damaged Materials

Vicker's indentation is used in the point contact loading of a specimen to produce a model crack system.

Median, lateral, and radial cracks are induced in a specimen by Vicker's indentation. A plastically deformed zone also exists beneath the indentation [54,55]. Starting at the plastically deformed zone, the lateral crack runs parallel to the specimens surface and the median and radial cracks run normal to the surface. In studying the transmissivity of an isolated crack, for example a lateral crack produced by Vicker's indentation, we can use a model [44] consisting of an air gap between two media with index of refraction n. Kodre and Strand [56] quantitativly interpreted the transmissivity of an air gap between a plano-convex lens and a glass medium. They obtained the following equation for the transmissivity, T_p, of an air gap:

$$T_p = 1/(A_p \sinh^2 q+1) \qquad (13)$$

where A_p = thickness independent parameter

$q = 2\Pi(n^2 \sin^2 i-1)^{1/2} Z/ó$

with Z = gap thickness

n = refraction index of the prism

i = angle of incidence

$ó$ = the vacuum wavelength

The value of A_p depends on the polarization of incident radiation. The polarization state can be transverse magnetic

or transverse electric [56].

Another model is used to describe the loss in infrared transmittance when radiation is incident on impact damaged specimens. Previous studies have been preformed on ceramics which have sustained liquid jet impact damage [57]. The damage induced in these specimens is exhibited as an undamaged central zone, surrounded by a ring of short circumferential cracks. Transmittance loss in the infrared scattering of impacted specimens can be described by Debye's theory of scattering from an inhomogeneous material.

Debye investigated electromagntic scattering from a two phase solid [46]. The size of inhomogeneous regions and the change in the index of refraction effect the distribution and intensity of the scattered radiation. Debye determined the intensity of scattered light, i, to be:

$$i = V\langle\eta^2\rangle_{av}w \tag{14}$$

where η = electron density of the material

V = volume illuminated by electromagnetic radiation

and w, the correlation volume, is expressed as:

$$w = (8\Pi a^3)/(1+k^2s^2a^2)^2 \tag{15}$$

where a = length of the scattering center

k = the wavenumber

s = $\sin\theta$

θ = the scattering angle

The correlation volume depends on the direction of observation and the wavelength of the radiation. If one of the two phases is a void phase [44] then,

$$\langle\eta^2\rangle_{av} = \eta_o\phi(1-\phi) \qquad (16)$$

where η_o = electron density of the matrix

ϕ = volume fraction of the void

thereby we obtain,

$$i = [8\Pi a^3\eta_o\phi(1-\phi)V]/(1+k^2s^2a^2)^2 \qquad (17)$$

1.2.4 The Fourier Transform Infrared Spectrophotometer

The wavelength range for infrared radiation is 10^{-6} to 10^{-3} m [58]. Energies of some of the vibrational modes solid lattices coincide with specific frequencies in infrared radiation. Infrared spectroscopy is used to study the interaction of infrared radiation with a solid.

In Fourier Transform Spectrscopy, an interferometer

emits a signal of a specified frequency range. The signal emitted varies due to interference in the interferometer. The measure of the signal variation is an interferogram. Fourier transformation of the interferogram produces a spectrum of the transmitted or absorbed intensity as a function of frequency. A Fourier transform infrared spectrophotometer measures the transmittance of a specimen at each frequency, by taking a ratio of the energy transmitted to the amount of energy transmitted when no sample is present [59].

1.2.5 Thermally Shocked Specimens

Specimens undergo thermal shock when subjected to a rapid temperature change. In this investigation, the Fourier Transform Infrared (FTIR) Spectrophotometer is used to study the damage in alumina specimens due to thermal shock.

Two methods are used to determine the resistance to thermal stresses in ceramics [60]. One method is based on thermoelastic theory. Using this method, materials are chosen with particular properties in order to avoid fracture due to thermal stresses. These properties include low values of Young's modulus, Poisson's ratio, emissivity, and thermal expansion coefficient, along with high values of thermal diffusivity, thermal conductivity, and tensile strength. The second method is based on the amount of crack propagation and

the subsequent change in the physical behavior of the specimen. For example, a decrease in weight, change in permeability, or change in strength can be used to determine thermal stress resistance.

Hasselman [61] developed a theory of crack propagation under thermal stress conditions. The stress field within a thermally shocked specimen is the only source for the driving force of crack propagation. A complete fracture will not occur as long as the amount of fracture energy necessary for a crack to propagate over the cross sectional area of a specimen is greater than the total elastic energy in the specimen. Therefore, at fracture, materials with low elastic energy and high values of fracture energy will have high values of thermal shock resistance.

Kingery, Bowen, and Uhlman [50], state that nucleation of a crack occurs when the thermal stresses in a specimen equals the fracture stress. The change in temperature required for fracture, ΔT_f, is calculated by the following general equation:

$$\Delta T_f = S\sigma_f(1-\mu)/(Ea) \qquad (18)$$

where σ_f = fracture stress

μ = Poisson's ratio

a = linear expansion coefficient

E = modulus of elasticity

S = shape factor

Hasselman [60] used a model consisting of a body stressed to the maxium value of thermal stress, to study the propagation of cracks. He developed the following equation for critical temperature difference, ΔT_c, required for crack instability:

$$\Delta T_c = [(\pi G(1-2\mu)^2)/(2E_o a^2(1-\mu^2)]^{1/2} * [1+(16(1-\mu^2)Nl^3/9(1-2\mu))]c^{-1/2} \quad (19)$$

where c = crack length

E_o = Young's modulus of the crack free material

G = shear modulus

N = cracks per unit volume

Crack initiation and propagation occurs at a temperature difference of ΔT_c. At this point there is also an instantaneous decrease in strength. For cracks which are initilly short in length and propagate kinetically at ΔT_c, the temperature difference must be increased to $\Delta T_c'$ for further crack propagation. At $\Delta T > \Delta T_c'$ crack growth is quasistatic. The specimen's strength gradually decreases at $\Delta T > \Delta T_c'$ [60].

Hasselman [60] also suggests that the extent of kinetic and quasistatic crack propagation is a function of the number

of propagating cracks. The specimen size, shape, material, and type of thermal shock are all factors which determine the number of cracks.

T. K. Gupta [62] studied the propagation of cracks and decrease in strength of thermally shocked Al_2O_3 specimens. Gupta's results agreed with the theory of thermal shock in ceramics developed by Hasselman. In the study, the extent of crack propagation, after thermal shock, was observed to decrease with increasing grain size. The strength of the specimens was also decreased, after thermal shock, with increasing initial strength.

One method which is used to study the damaged incurred by a specimen after thermal shock is to make Young's modulus and internal friction measurements by the flexural vibration technique [63,64]. This technique is a nondestructive process. In this investigation another nondestructive method is used to study thermally shocked specimens. This method is based on IR transmittance measurements using a Fourier Transform Infrared Spectrophotometer.

2.0 Experimental Procedure

Diamond thin film coatings were deposited on to silicon wafers. The indentation technique was then used to observe the adherence of the diamond thin film. Infrared transmittance of non-coated silicon, diamond coated silicon, alumina, zinc selinide, and zinc sulfide specimens which have sustained damage due to indentation, thermal shock, or water jet impact was obtained using the Fourier Transform Infrared Spectrophotometer.

2.1 Diamond Thin Film Specimens

A microwave plasma disk reactor was used to deposit the diamond films on silicon wafers. After deposition, Vicker's indentation (with a 9.8 N load) was used to induce delaminations of the diamond thin film and measurements of the delamination diameter were made. Film thickness, grain size, and surface morphology were determined using a scanning electron microscope. Raman Spectroscopy was used to prove that the films were actually diamond.

2.1.1 Specimen Preparation

Circular p and n type silicon wafers having 100 surface, approximately 8 cm in diameter, and having a thickness of

0.4 mm were obtained from Monsanto Company. The silicon was cleaved into approximately 2 cm X 2 cm and 2.5 cm X 2.5 cm square specimens. To increase the initial nucleation density of the diamond, the silicon specimens were polished by hand with a 0.25 micron diamond paste. The specimens were then rinsed with acetone to remove any residue.

After polishing, each specimen was cleaned using the RCA silicon cleaning procedure [65]. In this procedure the specimens are first placed in boiling TCE for three minutes. They are then rinsed with acetone, methanol, deionized water, and blown dry with nitrogen. Next the specimens were put in a degrease etch for ten minutes at a temperature of $70 \pm 5^{o}C$. The composition of the degrease etchant was: 75 ml deionized water, 15 ml hydrogen peroxide, and 15 ml amonium hydroxide. Following the degrease etch the silicon wafers were rinsed with deionized water and blown dry with nitrogen. The specimens were then placed in a demteal etchant for ten minutes again, at $70 \pm 5\ ^{o}\ C$. The demetal etchant consisted of 80 ml deionized water, 20 ml hydrogen peroxide, and 10 ml hydrochloric acid. After the demetal etch, the specimens were again rinsed with deionized water and blown dry with nitrogen. A fume hood was used when working with the TCE, degrease etch, and demetal etch.

2.1.2 Deposition of Diamond

Diamond thin films were deposited on the (100) surfaces of silicon substrates using a microwave plasma disk reactor [66,67], as illustrated in figure 2. The system was operated at 2.45 GHZ, using a cylindrical cavity with a 17.8 cm inner diameter. The plasma was contained in a quartz chamber having a 9.25 cm inner diameter.

The silicon wafers were positioned on a graphite plate which was 2.25 mm thick on the edges and 1.85 mm thick on the recessed area corresponding to the size of the silicon. The graphite holder was put on a quartz tube which had a 18.67 mm outside diameter and 1 mm wall thickness. For specimens CP1, CP2, CP3, and CP6 the length of the quartz tube was 3.5 cm. Specimens NDFP1, NDFN13, and NDFP13 were processed using a 3.25 cm quartz tube. A 2.6 cm quartz tube was used during the diamond depostion for WDF31.

First the microwave cavity was pumped down to 10^{-4} Torr by a roughing pump. When the digital pressure gauge (MKS Instruments Inc., Burlington, MA) indicated approximately zero pressure, a mixture of CH_4 and H_2 was allowed to flow into the chamber through twelve small gas inlets. The CH_4/H_2 ratios ranged from 0.5 to 1.0 percent in this investigation. A type 286 Flow Controller (MKS Instruments Inc., Burlington, MA) was used to measure and control the amount of each gas introduced into the chamber. The total gas flow ranged from

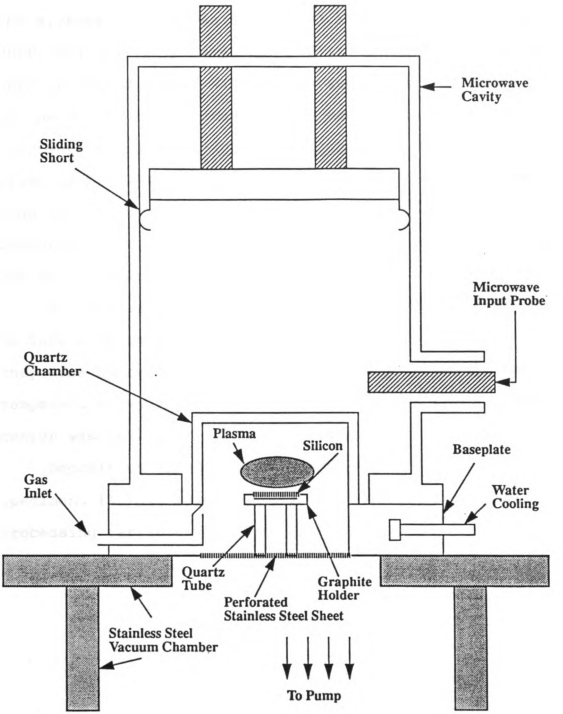

Figure 2. Microwave plasma disk reactor system used to deposit the diamond thin films [68].

100 to 250 standard cubic centimeter. A coaxial power input probe was used to couple the microwave power to the cavity. The microwave power was maintained at 750 W for specimen NDFP1 and 1000 W for specimen WDF31. The remaining specimens were processed at 700 W. A perforated stainless steel sheet, at the bottom of the chamber, was used to terminate the microwave energy. Cavity excitation mode, TM 011, was selected by adjusting the sliding short and input probe to tune the cavity. To maintain the desired plasma pressure, as measured by the Baratron pressure gauge, the roughing valve was adjusted accordingly.

An optical pyrometer (Ircon Inc., model UX20) was used to take temperature readings of the silicon substrates as they were heated by the plasma. In order to obtain the temperature readings, a sliding short with a hole in the center was utilized.

Deposition times ranged from four to eight hours for the specimens in this investigation. Table 2 contains the processing variables for each specimen.

Table 2. Processing Variables for Diamond Film Deposition

Specimen label	Si Type	CH_4/H_2 (%)	Plasma Pressure (Torr)	Time (hrs.)
NDFP1	p	1.0	65-70	4.0
WDF31	n	0.67	*	4.0
NDFN13	n	0.5	70	6.0
NDFP13	p	0.5	70	6.0
CP1	p	1.0	70	5.5
CP2	p	0.5	60	8.0
CP3	p	0.5	60	7.0
CP6	p	0.5	60	7.0

* unknown

2.1.3 Delamination

A microhardness indenter (by Buehler Limited) was used to produce Vicker's indentations on the diamond thin film coated silicon specimens. L. Flowers, K. Meyers, and N. Maguire are three undergraduate students at Michigan State University that conducted a portion of Vicker's indentation study. The indentations were made at a 9.8 N load, at a loading speed of 45 μm/sec, and a load time of ten seconds. Circular delaminations of the film resulted from the indentations. As illustrated in figure 3, the diameter of the delaminations, a, was recorded for each indentation. At least four different measurements of delamination diameter were taken at each indent site in order to determine a mean value. Indentation patterns across the specimen were either grids or crosses. The indentaions were spaced approximately 2 mm apart.

2.1.4 SEM Observation

Grain size, coating thickness, and surface morphology were observed using the JEOL JSM-35C Scanning Electron Microscope (SEM). In order to determine the coating thickness, the specimens were fractured using the microhardness indentor at an increased load of 49 N. A line was made of alternating 9.8 N and 49 N indentations in order

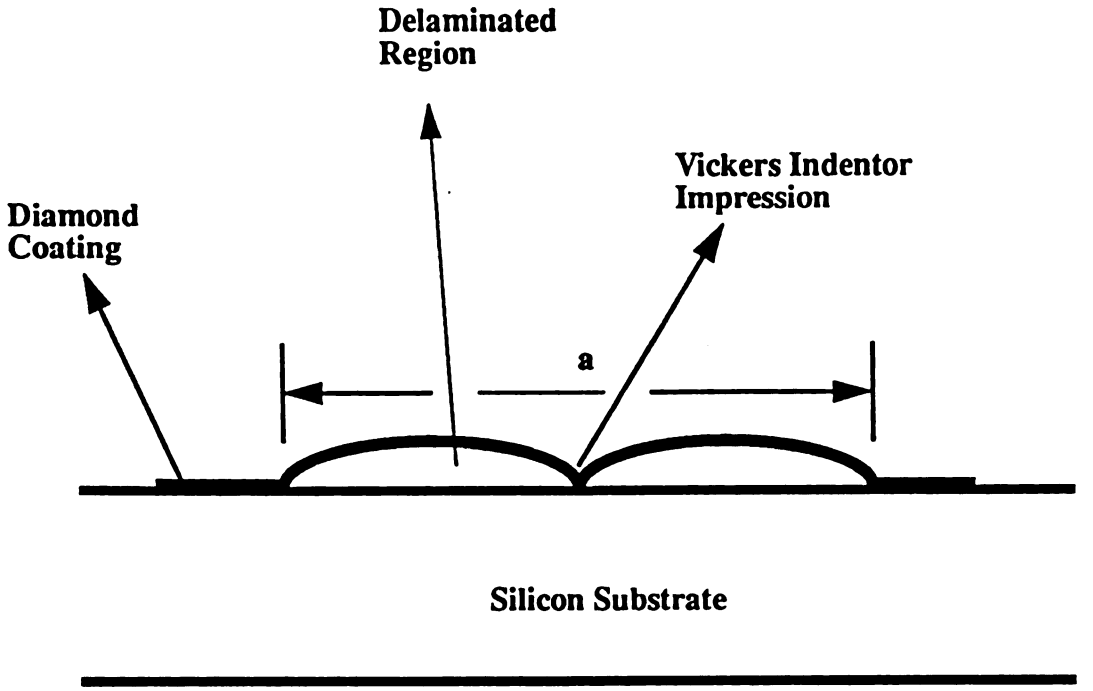

Figure 3. Diamond thin film delamination after Vicker's indentation.

to produce a nearly straight macrocrack to fracture the specimens. The specimens were then mounted on edge, using Duco cement (by Devcon, Wood Dale, IL), such that the fracture surfaces could be observed in the SEM. Observations of the grain size and surface morphology were made on specimens mounted parallel to the surface of the stub. To prevent charging during SEM observation, a fine line of colloidal graphite (Electron Microscopy Sciences, FT. Washington, PA) was drawn from the specimen to the edge of the metal stub. The specimens were coated with gold in the sputter coater to make them conductive. The deposition time for the gold coating of each specimen was three minutes at a coating rate of seven nm per minute. A fifteen kV accelerating voltage was used during the SEM observation.

The thickness of the diamond coating was recorded as a function of position for each micrograph. Ten to fifteen measurements were made on each micrograph to determine a mean value and standard deviation of coating thickness in the region included in the micrograph. Magnifications for the SEM micrographs ranged from 4000 to 10000, and thus the field of view in each micrograph ranged from 16.9 to 6.64 μm.

The grain size of the polycrystalline diamond coatings was determined using the linear intercept method. The grain size, g, is given by:

$$g = L/(N*M) \qquad (20)$$

where L = length of the line on the micrograph

N = number of boundries the line intercepts

M = magnification

For each measurement of grain size at least 100 intercepts were counted by randomly drawing lines on the micrograph.

2.1.5 Raman Spectroscopy

The sp^3 bonding of carbon which is characteristic of diamond was identified using Raman Spectroscopy. Dr. Gray (Norton Company, Northboro, MA) conducted the Raman spectroscopy on specimens obtained from Bohr-ran Huang, a PhD student in the Electrical Engineering Department at Michigan State University. These specimens were pretreated in the same manner as the specimens in this investigation, and the diamond deposition system was also the same. Dr. Gray's work utilized a 400 mW argon beam with a wavelength of 488 nm and a double pass one-eighth meter monochrometer with a grating of 1800 lines per mm. A 1024 element diode array detector was also used in conducting the Raman spectroscopy.

2.2 FTIR Spectroscopy

The Fourier Transform Infrared (FTIR) Spectrophotometer was used on a variety of specimens in order to obtain the

infrared transmittance of damaged and undamaged areas on the specimens. Thermally shocked alumina specimens, indented silicon, indented zinc sulfide, and indented diamond coated silicon were tested in the FTIR spectrophotometer. Infrared spectra was also obtained for a zinc selinide specimen damaged by water jet impact and a zinc sulfide specimen damaged by compression.

2.2.1 Description and Preparation of Al_2O_3, ZnS, and ZnSe

Rectangular plates of alumina, with dimensions of 11.5 cm x 11.5 cm x 0.1 cm, were obtained from Saxonburg Ceramic Incorporated, Monroe, North Carolina. Won Jae Lee, a Ph.D. student in the Metallurgy, Mechanics, and Materials Science Department at Michigan State University prepared the alumina specimens. Using a low speed diamond saw, the rectangular plates were cut into prismatic bars. SiC paper (600 grit) was used to polish the edges of the cut specimens, to achieve a uniform width. Specimen preparation or processing could have induced residual stresses in the specimens. To relieve the specimens of residual stresses, the specimens were annealed in an electrical resistance at 1150 degrees Celsius in air for twelve hours. The linear intercept technique on SEM micrographs of fracture surfaces, was used to determine the average grain size (10 μm) of the prismatic bars. The average mass for the prismatic bars, with approximate

dimensions 110.82 mm x 12.66 mm x 1.07 mm, was 5.6306 g. In this investigation, the alumina has a mass density of 3.71 g/cm^3 which corresponds to a volume fraction porosity of about 6.7 percent. Three substrates labeled REF, C1, and A5 were used in the investigation.

The alumina specimens were held, at a specified temperature, in a vertical-muffle electric furnace for twenty minutes and then quenched in a container of distilled water. The temperature of the distilled water was maintained at approximately twenty-one degrees Celsius. Before starting another thermal shock cycle, specimens were kept in the water bath for fifteen minutes. For specimen C1, ΔT, the difference between the furnace temperature and the temperature of water bath was 284 degrees Celsius. ΔT for specimen A5 was 310 degrees Celsius. Specimen C1 was thermally shocked for a preselected number of cycles, tested in the FTIR, and then shocked for another preselected number of cycles. Specimen A5 was thermally shocked forty times and then tested in the FTIR spectrophotometer.

The water jet impacted zinc selinide and damaged zinc sulfide specimens were obtained from Dr. Eldon Case (Associate Professor, Metallurgy, Mechanics, and Materials Science, Michigan State University). A disk-spaced ZnSe specimen 6.83 mm thick with a 18.9 mm diameter sustained impact damage by a water jet apparatus with a 0.8 mm oriface diameter. During impact the gauage pressure was 240 psi and

the velocity was 375 m/s. This specimen was labled ZSE3. For the ZnS specimen a 10 Kg load was used to produce a Vicker's indentation on the specimen. The ZnS specimen was 3.84 mm thick and 15.08 mm in diameter. Another zinc sulfide specimen was damaged using a brass specimen holder capable of applying a compressive load to the specimen via a sliding jaw tightened with allen screws.

2.2.2 Equipment Description

The model 1850 Perkin-Elmer Fourier Transform (FTIR) spectrophotometer is a double beam instrument with a frequency range of 4000 cm^{-1} to 150 cm^{-1} and maximum resolution of .2 cm^{-1} [69,70]. The system consists of an optical unit, a PP1 plotter/printer, a Perkin-Elmer 7700 personal computer, and the CDS-3 Applications software. The optical unit is software controlled. It is capable of single beam, single-beam ratio, and double-beam recording of spectral data. The source of the infrared radiation is a heated wire element operating at 1050 degrees Celsius. For thermal stability, the source is insulated and air cooled.

Radiation from the source goes to the source toroid, which directs it through the Jaquinot stop, a variable sized aperature that controls the shape of the beam and the amount of energy allowed to enter the interferometer. Six different aperature sizes are available.

The radiation then travels to the interferometer, where a paraboloidial mirror collimates the beam and directs it toward the beamsplitter. Two different beamsplitters are available. The first consists of Germanium on a KBr substrate and the second is a mylar beamsplitter. Germanium on a KBr substrate is useful in the wavenumber range of 4500 to 450 cm^{-1}. The mylar beamsplitter is useful in the range from 500 to 150 cm^{-1} wavenumbers. The beam of electromagnetic radiation is divided on the beamsplitter, causing half of the radiation to travel to the fixed mirror and the other half to be directed to the moving mirror. Fifty-percent of each of the two components of the original beam are recombined at the beamsplitter, after being reflected by both mirrors. The two beams interfer at the beamsplitter when recombined and then are partially reflected toward the sample compartment. Therefore only half of the source energy is incident on the sample.

The beam is directed toward the detector after leaving the sample compartment. The standard detector has a two millimeter diameter. It is a 1-alanine doped deuterated triglycine sulfate (DTGS) element with a cesium iodide window. A mercury cadmium telluride (MCT) detector is also available, which has a better signal to noise ratio. The CDS-3 application software is used to operate the spectrophotometer. Various components of the optical system are controlled by mode and instrument commands. Five pre-

def

use

sel

bef

var

tha

bec

cha

on

A l

pu

af

wa

sp

mi

or

te

of

li

de

co

in

co

Fr

defined modes are availabe for particular situations, and the user can also create a particular mode. It is important to select the detector to be used, under the instrument command, before selecting a particular mode since the mode settings vary according to the chosen detector. User created modes that are used frequently can be stored on a disk.

Water vapor in the sample chamber must be minimized because water is a strong IR absorber [70]. The sample chamber is therefore purged with dry air. Pressure measured on the purge gas regulator should be maintained at ten psi. A humidity indicator, exhibits the extent to which the purging has progressed. Each scan in this study was run only after the chamber had been purged.

In part of this investigation the infrared microscope was utilized. The IR Plan infrared microscope has a maximum spatial resolution of ten microns and is a research grade microscope [69]. The microscope can be used in transmission or reflectance mode to obtain FTIR spectra from areas from ten to one hundred microns in diameter. Since a low amount of energy is put through the microscope, a very sensitive liquid nitrogen cooled Mercury-Cadmium-Tellurium (MCT) detector is used. For proper operation of the IR microscope, correct alignment is very important. Proper alignment insures that the visible light and infrared beams are coincident and the area viewed will be that from which the FTIR spectra is obtained. One method used to check the

alingment was to type "align meter front" to observe the beam energy. During operation the beam energy was maintained between 0.50-1.00. To measure the performance of the microscope the peak to peak signal to noise ratio was used. This value should be greater than 1000 to insure proper alignment of the microscope. A plastic enclosure was used around the microscope to purge the air surrounding the specimen, before scanning. The following list includes instrument parameters and mode parameters used for operation of the infrared microscope.

Instrument Parameters

Detector: MCT
Internal source: on
External source: out
Sample beam: front
Zero crossings: 2
Neutral density filter: None 3
Optical filter: None None
Polarizer: None
Bidirectional scanning: on

Mode Parameters

Optimal range: 4000 cm^{-1} 600 cm^{-1}

Nominal resolution: 4.00

Jaquinot stop: 6

Aquire mode: single beam

Number of cycles: 200

Spectrum type: Real

Interferogram: Double sided

Phase Correction: self 128

OPD velocity: 1.50 1.50

Gain: 8 8

Apodization: medium 1.00

cycle: 0 1 0 0 1

It should be noted that this is a single beam mode. Before the specimen is put into place, a background spectrum is taken and stored. The FTIR spectrum for the specimen is then obtained and stored. Finally the ratio of the specimen's transmittance to the background transmittance is computed.

2.2.3 Testing of Alumina Specimens

Specimen REF was used as the reference specimen. Each time specimen C1 was tested, specimen REF was also tested. Two sample holders consisted of rectangular pieces of

cardboard (114.76mm x 50.43mm), which contained rectangular openings (82.45mm x 11.28mm). During the acquisition of all spectra the reference specimen was fixed in one position, with tape, on a specimen holder. This made it easy to test the same region for each spectra obtained. The same three regions were scanned on specimen C1, each time it was tested in the FTIR spectrophotometer. After 1, 3, 5, 10, 20, 40, 60, 80, and 100 thermal shock cycles, specimen C1 was tested in the FTIR spectrophotometer. The ratio of percent transmittance of C1 to percent transmittance of REF was computed for each scan. Specimen A5, containing a large amount of damage, was scanned in three different specific regions.

A letter b was placed at one of the ends of the specimens. The following table lists the approximate positions of the incident electromagnetic radiation, as measured from the "b" end.

Table 3. Locations Where IR Spectra Were Obtained With Respect to the "b" End on the Alumina Specimens.

Specimen	distance (mm)		
label	region 1	region 2	region 3
C1	37.00	78.70	21.30
A5	28.97	52.27	14.46
REF	31.99	*	*

* only one region was used for the reference specimen.

The following list of instrument and mode parameters were used each time the alumina specimens were scanned.

Instrument Parameters

Detector:	DTGS
Internal Source:	on
External Source:	out
Sample Beam:	Front
Zero Crossings:	2
Neutral Density Filter:	none 3 none none
Optical Filter:	none none none none
Polarizer:	none
Bidirectional scanning:	off

Mode Parameters

Optimal Range:	4000 cm^{-1} 450 cm^{-1}
Nominal Resolution:	4.00
Jaquinot Stop:	6 6
Aquire Mode:	Double Beam
Number of cycles:	2
Spectrum Type:	Real
Interferogram:	Double Sided
Phase Correction:	self 128

OPD Velocity:	0.05		0.50		0.50		0.50		
Gain:	auto		auto		auto		auto		
Apodization:	Medium				1.0				
Cycle:	3	4	2	4	2	4	2	4	1

The OPD velocity is the optical path difference velocity measured in cm/sec. Cycle is used to define the variables such as delay between obtaining sample and reference spectra, the number of iterations used in obtaining the sample spectra, and the number of iterations used for the reference spectra. The Perkin-Elmer 1800 Series FTIR manual [69] may be refered to for a detailed description of the parameters.

After one hundred thermal shock cycles, C1 and the reference specimen were also scanned at a 10, 12, and 20 degree angle θ, as measured from the normal to the IR beam with a protractor. Additional angles of 2.0, 5.0, and 7.5 degrees were tried for the alumina specimens, but the specimens placement could not be done with a protractor. Using the data that the length of C1 is 70.5 millimeters and the length of the reference specimen is 75.61 millimeters, the distances (d) that the specimen's base had to be moved from the position of normal incidence were calculated and are listed in Table 4 in units of millimeters.

Table 4. Distances That the Alumina Specimen's Base was Moved From the Position of Normal Incidence.

Distance	Angles (degrees)		
(mm)	2.5	5.0	7.5
d_{Ref}	3.298	6.590	9.870
d_{C1}	3.075	6.140	9.200

2.2.4 Specimens Tested With the Infrared Microscope

Silicon specimens were Vicker's indented in the same manner as the diamond coated Si specimens, and then tested in the Fourier Transform Infrared Spectrophotometer. The radial crack, indentaion impression, and lateral crack were three damaged regions on the silicon specimens that were scanned. An undamaged region was also scanned and ratios of damaged to undamaged spetra were computed. For the diamond coated silicon specimens film delamination regions and undamaged regions were scanned and ratios were calculated.

Damage on the zinc selinide specimen, which underwent water jet impact, consists of an annular ring of cracks. There is a high density of small cracks at the inner radius and there are a few large cracks at the outer radius of the ring. Three different regions of this ring were scanned starting at the inner radius, proceeding outward, and passing

over 100 μm between each scan. An undamaged area was also scanned on this specimen and ratios of damaged area to undamaged area spectra were obtained.

Two damaged regions and one undamaged region were scanned on the indented ZnS specimen. This specimen was indented with a 98 N load. Damaged regions were tested at 50 and 200 microns from the indentation impression. Damaged to undamaged spectra ratios were again computed. After initial data was obtained the indentaion impression was removed by polishing with 3 micron diamond paste for 30 minutes. The polishing wheel was rotating at approximately 180 rpm's during the removal of the indentaion impression. After the rough polish the specimen was ultrasonically cleaned (with a 150 W ultrasonic cleaner) for five minutes using Alconox detergent. The specimen was observed at a 200X magnification on the Vicker's Indenter microscope before and after ultrasonic cleaning. From the observation it was found that particles were removed from the site of the previously existing indentaion impression by ultrasonic cleaning. The specimen was then fine polished for twenty-five minutes with 0.3 micron alpha alumina powder and rinsed with water.

3.0 Results and Discussion

3.1 Diamond Thin Film Specimens Produced

The microwave plasma disk source reactor was used seven times by the author in attempts to grow diamond thin films on silicon substrates. Of the seven specimens, two of them, CP4 and CP5, exhibited non-uniform coatings. The nonuniformity of coating on these specimens may be related to the fact that during processing the silicon wafers for CP4 and CP5 did not fit within the bevelled edges of the graphite holder. This in turn could cause a large point to point variation in temperature for the silicon substrate, since the edges of the graphite holder were observed by eye to be extremely hot. Another possible cause for the lack of uniformity is that the two specimens might not have had enough scratches induced during polishing. As observed in figure 4 the SEM micrograph exhibits preferential growth in the scratches on specimen NDFP1. The number density of scratches present is therefore important in the growth of the diamond coating.

In general, the temperature ranged from 990-1062 ^{o}C during the deposition of the films as measured by an optical pyrometer. The polycrystalline surface of a uniform diamond coating is exhibited in figure 5. To determine whether or not the coatings produced during deposition were actually

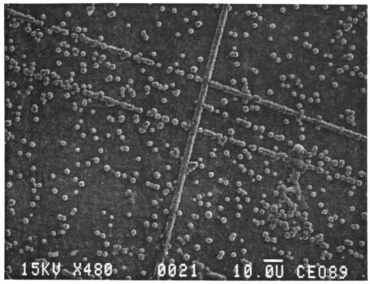

Figure 4. Nucleation of the diamond thin film coating on specimen NDFP1.

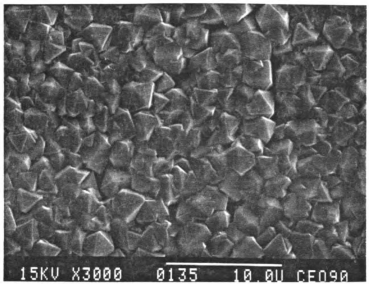

Figure 5. Polycrystalline surface of diamond thin film.

diamond, Raman spectroscopy was conducted by Dr. Kevin Gray from Norton Company, Northboro, MA. During aquisition of the Raman spectrum, a 400 mW Argon beam was utitlized wtih a 488 nm wavelength. A double pass one eighth meter monochrometer with a grating of 1800 lines/mm and a 1024 element diode array detector were also used. A typical Raman Spectrum from the diamond thin film specimens is shown in figure 6. The peak in intensity at 1332 inverse cm indicates the presence of diamond. At 520 cm^{-1} a peak in intensity is also exhibited which is characteristic of silicon. The presence of amorphous graphite was also exhibited by the broad hump in intensity at approximately 1540 cm^{-1}. It was therefore proven that the coatings were actually diamond.

3.1.1 Film/Substrate Interface

The film/substrate interface is very important in the adhesion of the film to the silicon substrate. XPS analysis was therefore obtained on samples from which the silicon substrate had been removed. Bohr-ran Huang (PhD student, Electrical Engineering, Michigan State University) prepared the samples for XPS analysis in the following manner. The coated silicon was cleaved into 5 mm by 5 mm samples which were placed diamond film down in an epoxy mixture. After an epoxy anneal, the silicon was removed by etching. Both NaOH and KOH based silicon etches were

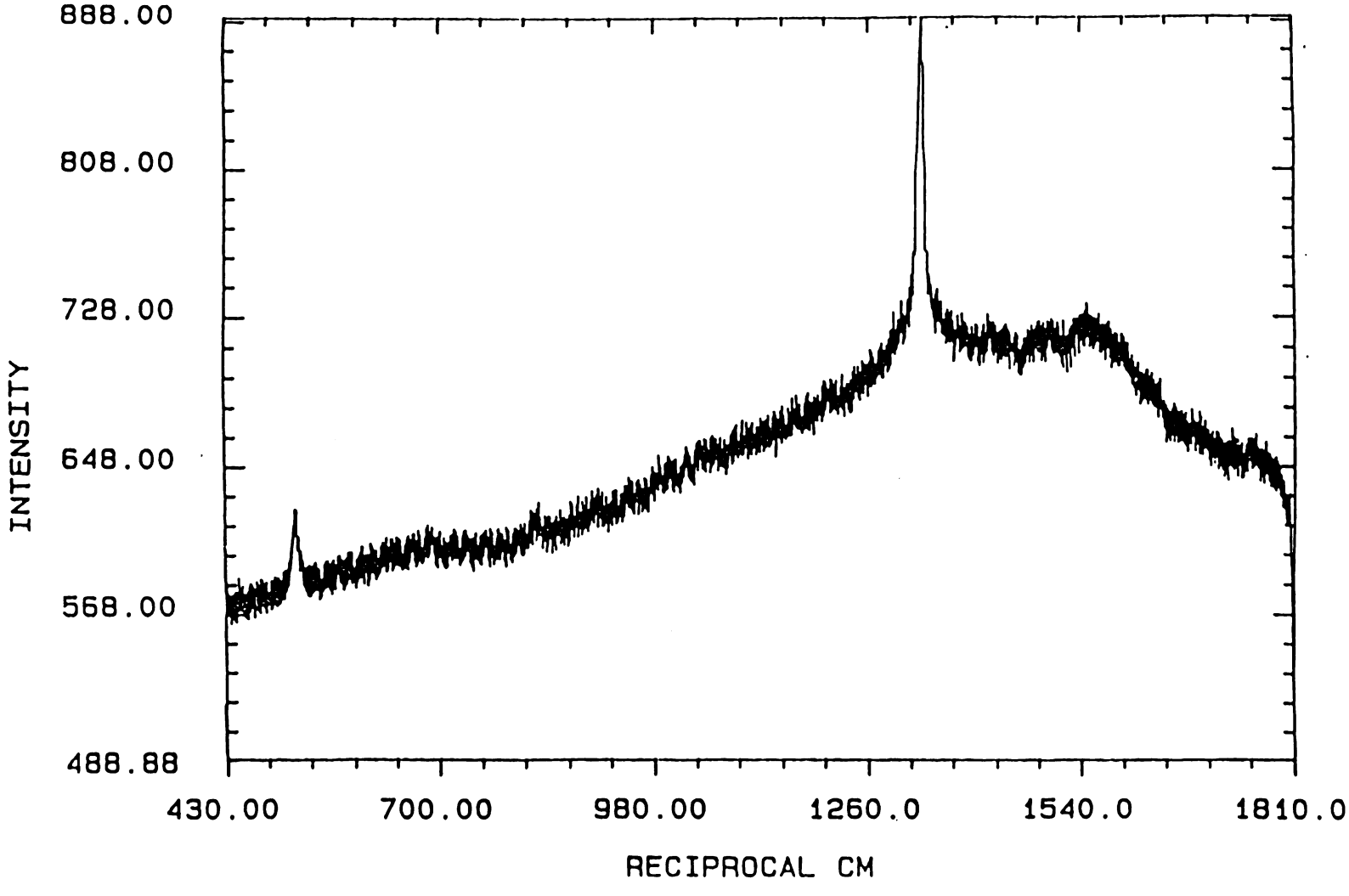

Figure 6. Raman Spectrum of a diamond thin film coated Si wafer [71].

successfully used.

XPS analysis [72] showed a shoulder on the principal main carbon peak at 282.75 eV binding energy, in agreement with an XPS study by Mizokawa et al. on sputtered silicon carbide films [73]. After a thirty second sputter of the diamond film sample with a 3 KeV argon beam, the film's silicon carbide peak was removed from the XPS spectrum. Based on the characteristics of the argon sputtering process, it was estimated that, an interfacial SiC layer approximately 30 Angstroms thick exists between the diamond coating and the silicon substrate [72]. It is important to note that the amount of interfacial layer may depend on the CH_4/H_2 ratio used during deposition. As the CH_4/H_2 ratio is decreased the deposition rate of the diamond coating also decreases. This may allow more time for the SiC interfacial layer to form, and therefore the layer may be thicker.

3.1.2 Delamination of the Diamond Thin Film

At a 9.8 Newtons load, as previously stated, Vicker's indentation successfully induced circular delaminations on eight different diamond thin film coated silicon specimens. The number of Vicker's indentations made on each specimen ranged from 13-49. In Appendix A, tables A1-A8 list the diameters of the resulting delaminations. For each specimen except NDFP1, five different measurements for delamination

diameter were made for each delamination site and an average value was calculated. Four measurements were made each delamination site for specimen NDFP1. In Appendix A, occasionally "No Delamination" is stated in place of the delamination diameter measurements. This means that the particular Vicker's indentation did not result in a visible delamination of the diamond thin film. Figure 7 illustrates the delamination that results from a 49 N load used to fracture a specimen for SEM observation. For the 49 N load, the maximum air gap between the substrate and film was approximately 3.3 microns (figure 7).

The effect of residual stress fields on delamination size was also investigated. The residual stress fields associated with Vicker's indentation can generate stress assisted slow cack growth in ceramics [74]. In addition, residual stress that may occur in the diamond film as a consequence of deposition could lead to slow crack growth [75]. Slow crack growth could potentially make the delamination diameter a function of elapsed time after indentation. To check the effect of residual stress, the diameters of 16 indent-induced delaminations were measured immediately after indenting. Each of the 16 delaminations were remeasured after exposure to the laboratory air for three weeks. For a mean indent diameter of 155 microns, the mean change in indent diameter was a negligible -0.7 ± 4.3 microns. Thus possible residual stresses from either the

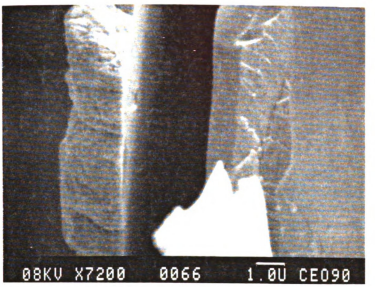

Figure 7. Diamond film delamination from 49 N Vicker's indentaion.

indentation or deposition do not appreciably change the delamination size as a function of time.

The delamination diameters observed varied with respect to film thickness, methane/hydrogen ratio used, and grain size of the diamond coating. Each specimen was fractured and observed in the SEM to determine both film thickness and grain size. Figure 8 is a typical micrograph of the fracture surface used to measure the thickness of the coating. Film thickness ranged from 1-4 μm.

In figures 9a-9e delamination diameters versus corresponding film thickness were plotted for each specimen. Table 5 contains the indentation identification numbers, from appendix A, that corresponded to the delamination diameters plotted for each specimen. In order to obtain coating thickness values corresponding to the delaminations, the specimen was fractured along a row of pre-existing delaminations (figure 10a) and the fracture surface was viewed in the SEM. The fracture was induced using higher indentaion loads (as stated in 2.1.4 SEM Observation). The coating thickness values were measured on the mirographs of these fracture surfaces. Error bars in the plot exhibit the calculated standard deviations for each variable. Comparing the graphs for the 0.5 percent methane/hydrogen processed specimens shows that CP6, NDFN13, NDFP13, and CP2 had an average delamination diameter lower than that of CP3. The thickness of the film for CP3 ranged from 3.25 to 4.0

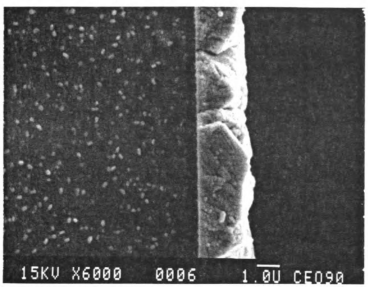

Figure 8. Fracture surface of diamond thin film coated Si wafer.

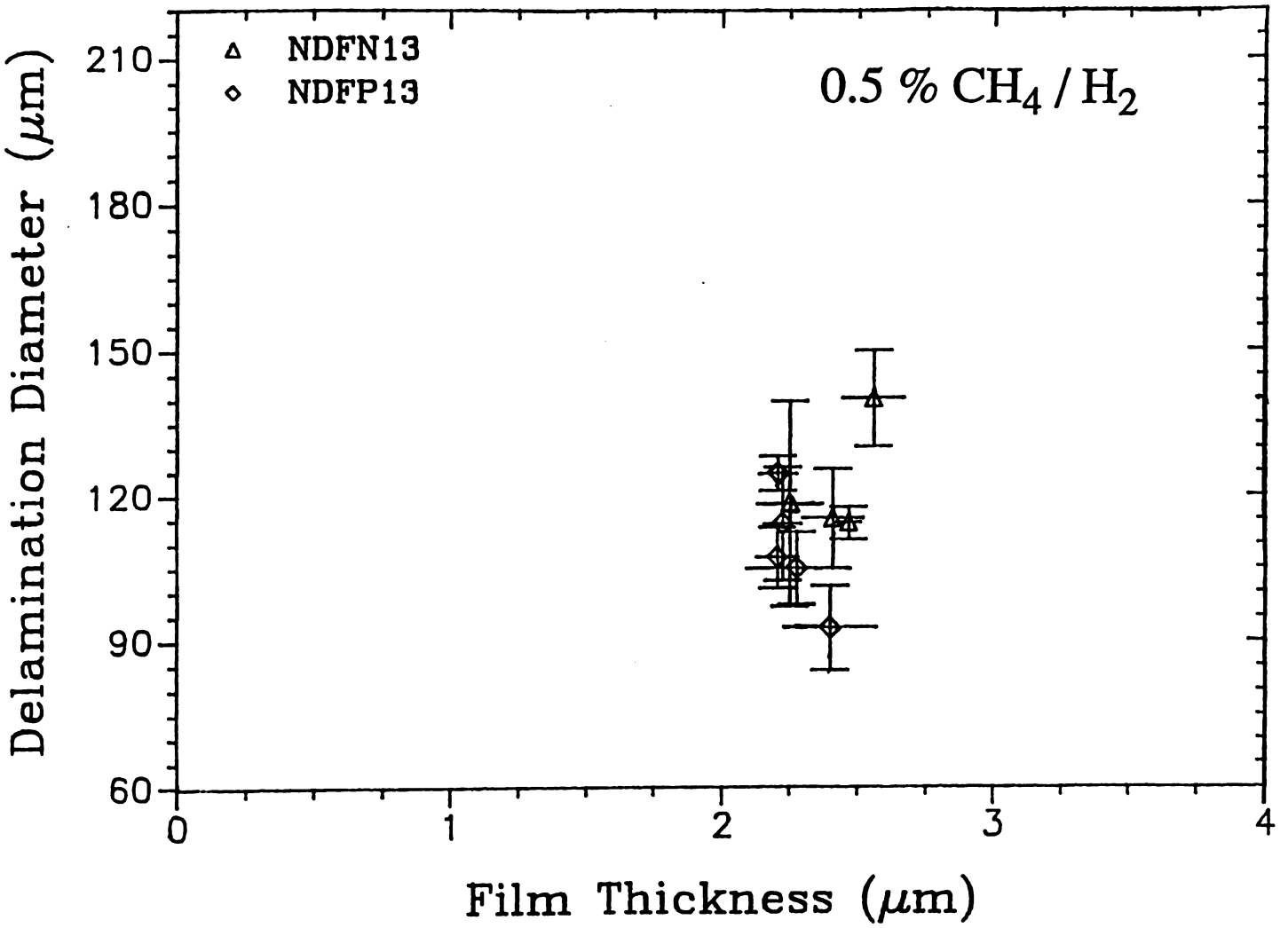

Figure 9a. Delamination diameter versus film thickness data for specimens NDFN13 and NDFP13.

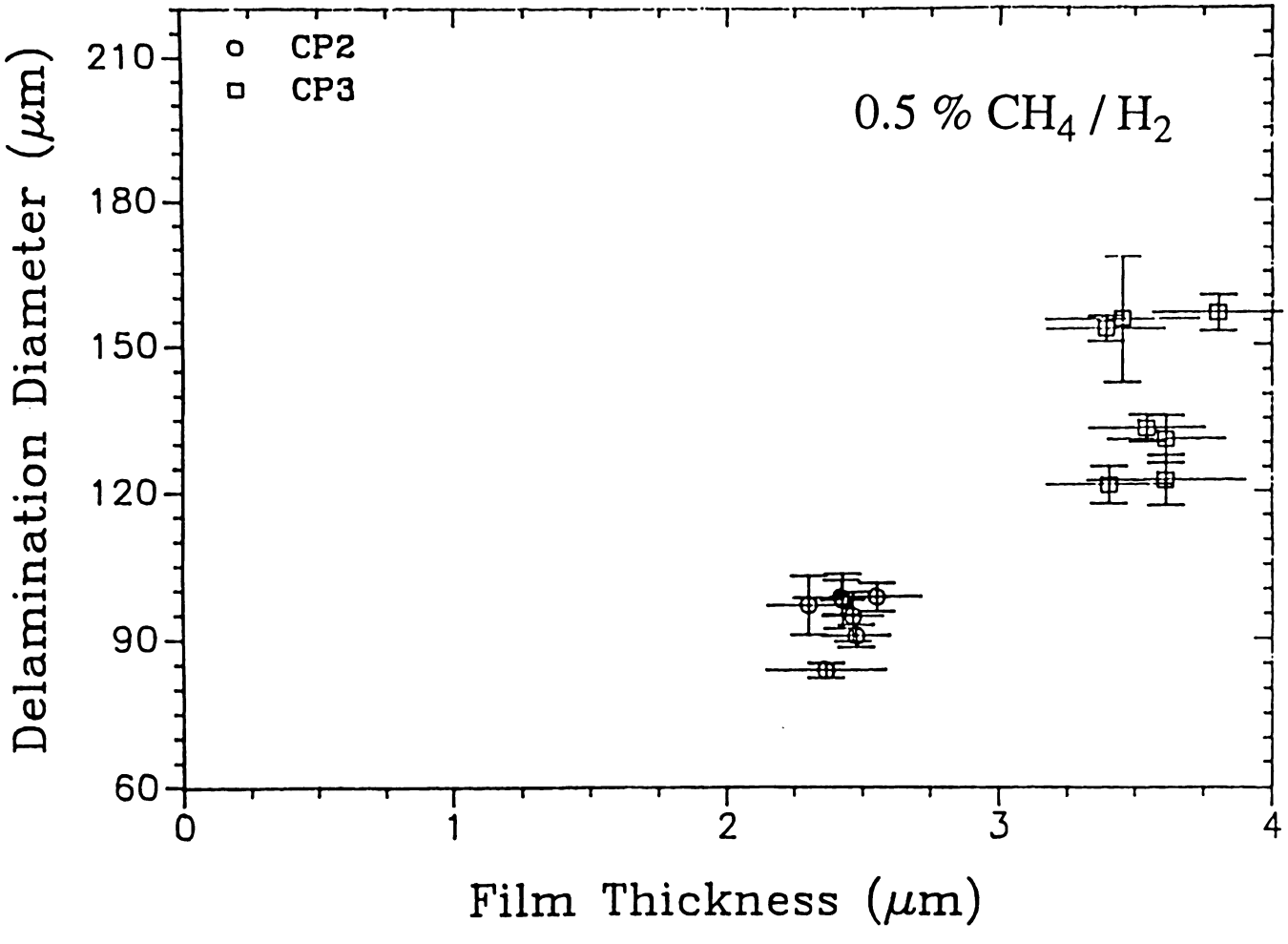

Figure 9b. Delamination diameter versus film thickness data for specimens CP2 and CP3.

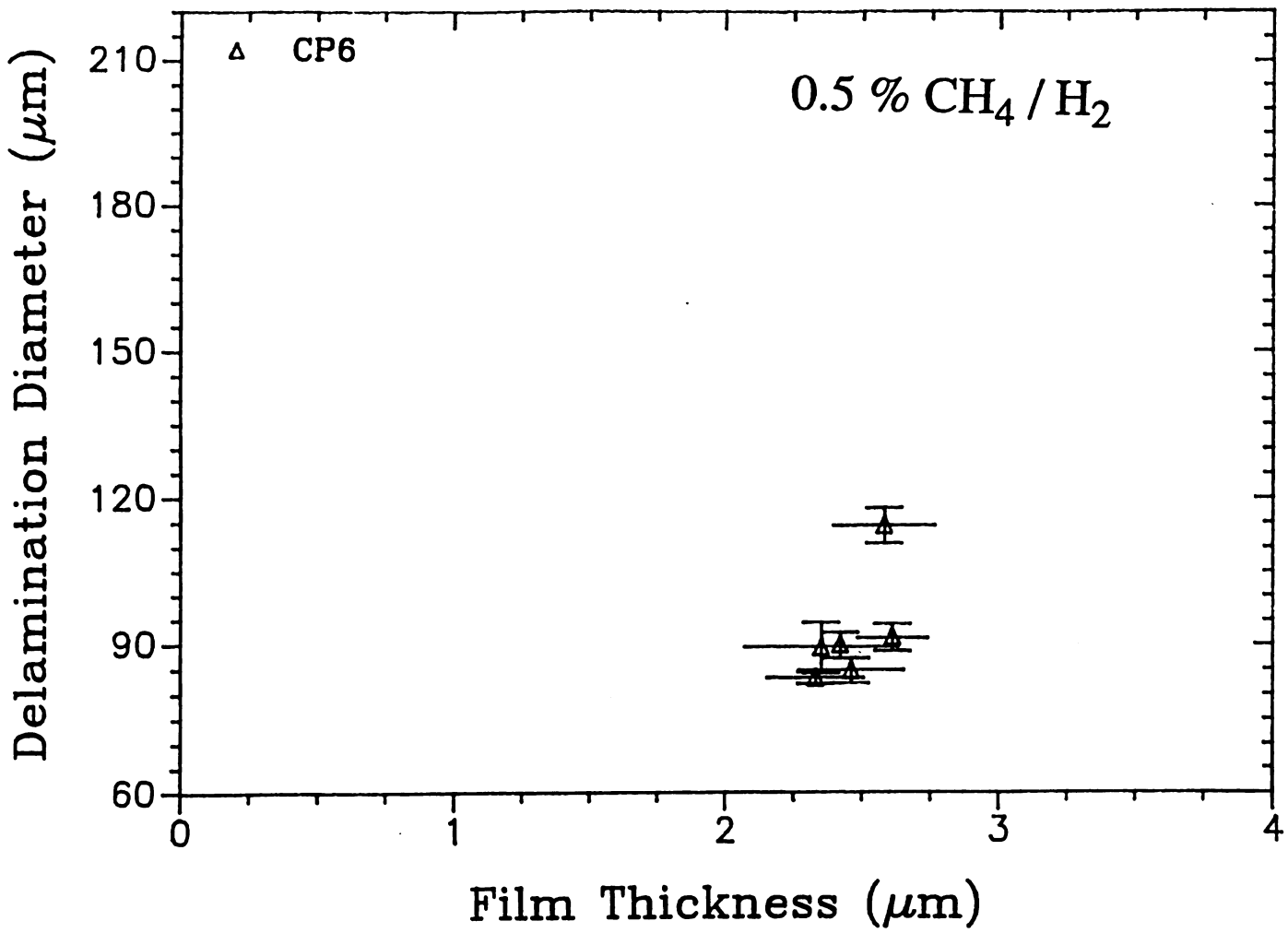

Figure 9c. Delamination diameter versus film thickness data for specimen CP6.

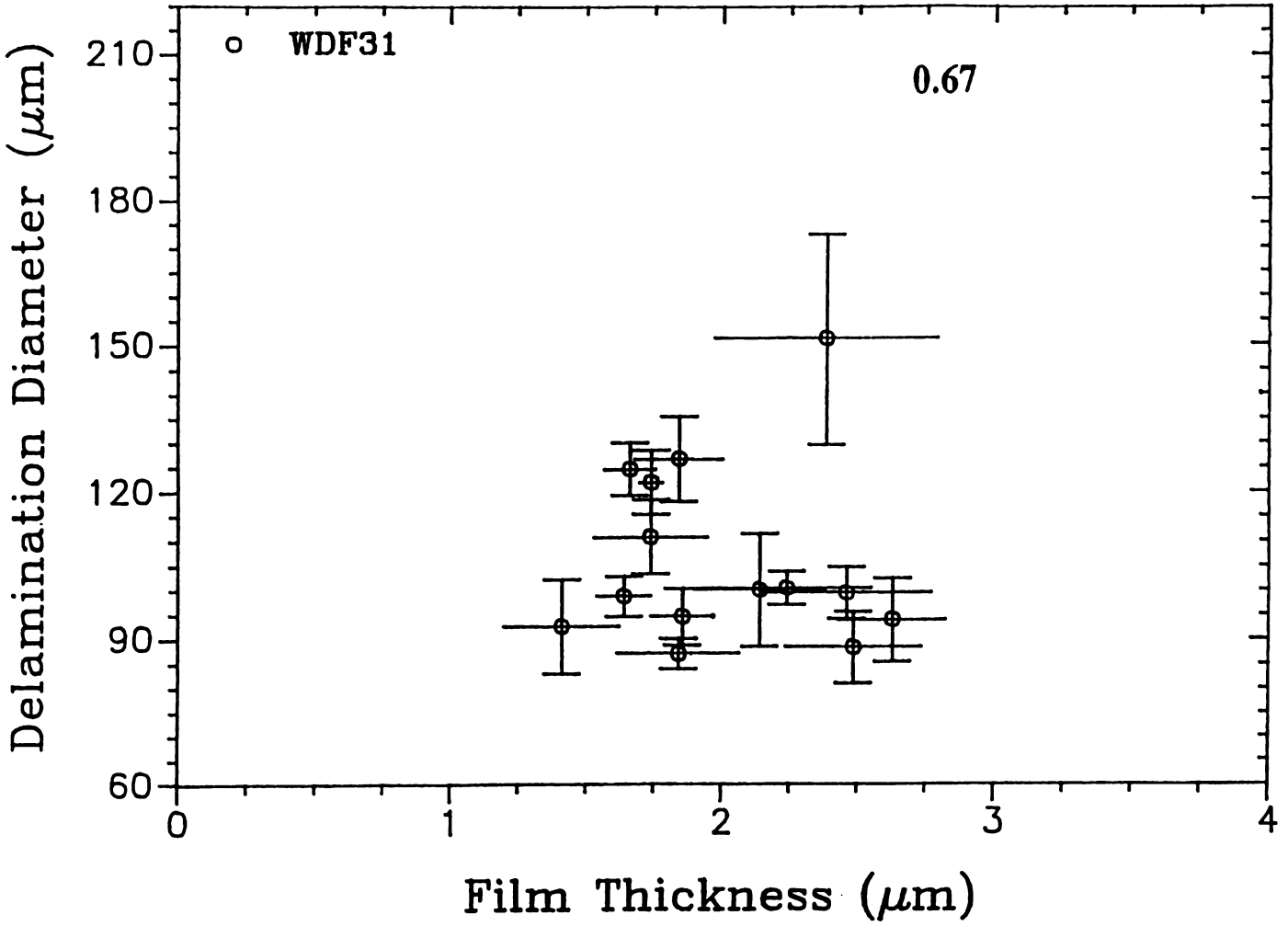

Figure 9d. Delamination diameter versus film thickness data for specimen WDF31.

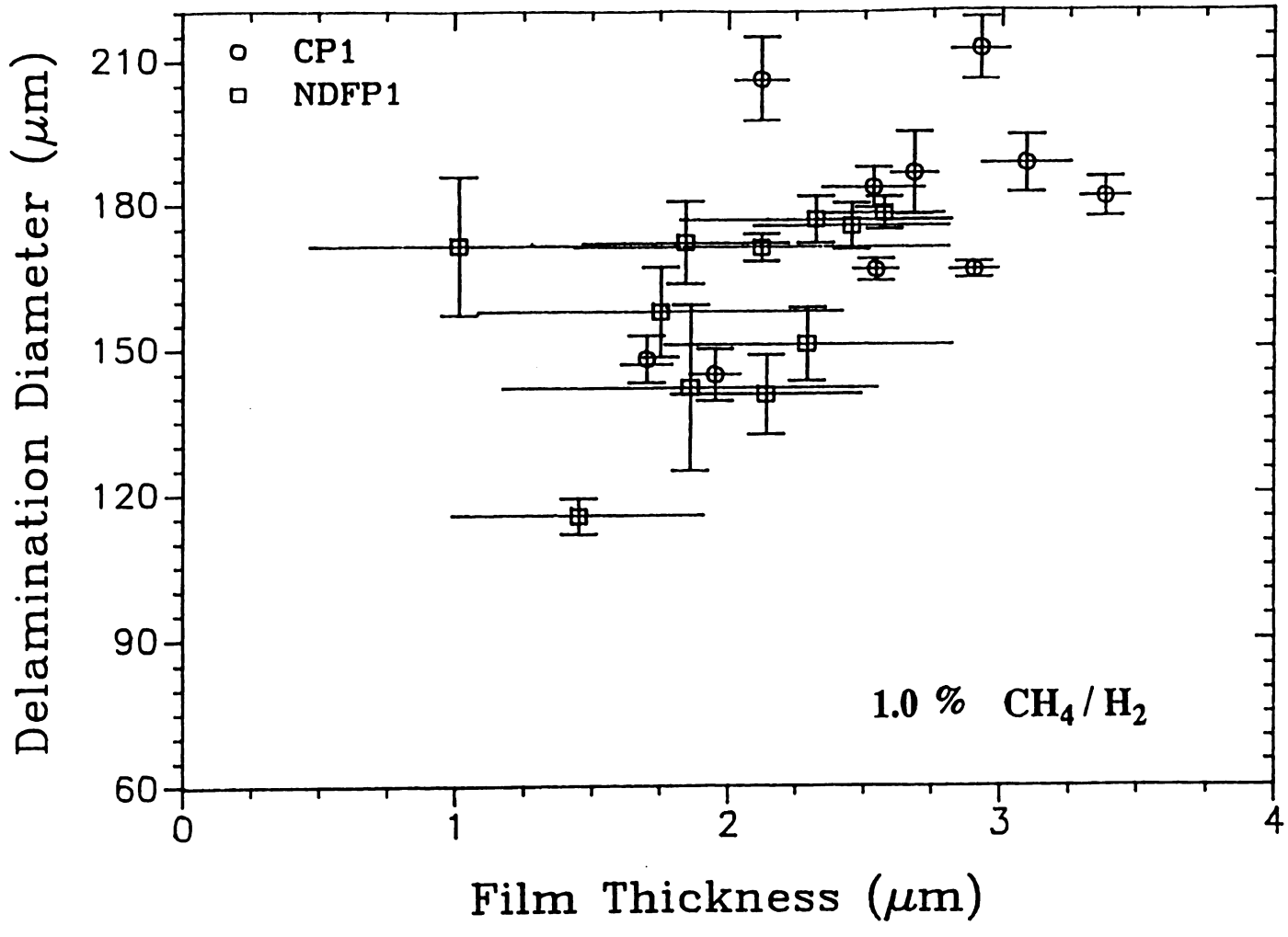

Figure 9e. Delamination diameter versus film thickness data for specimens CP1 and NDFP1.

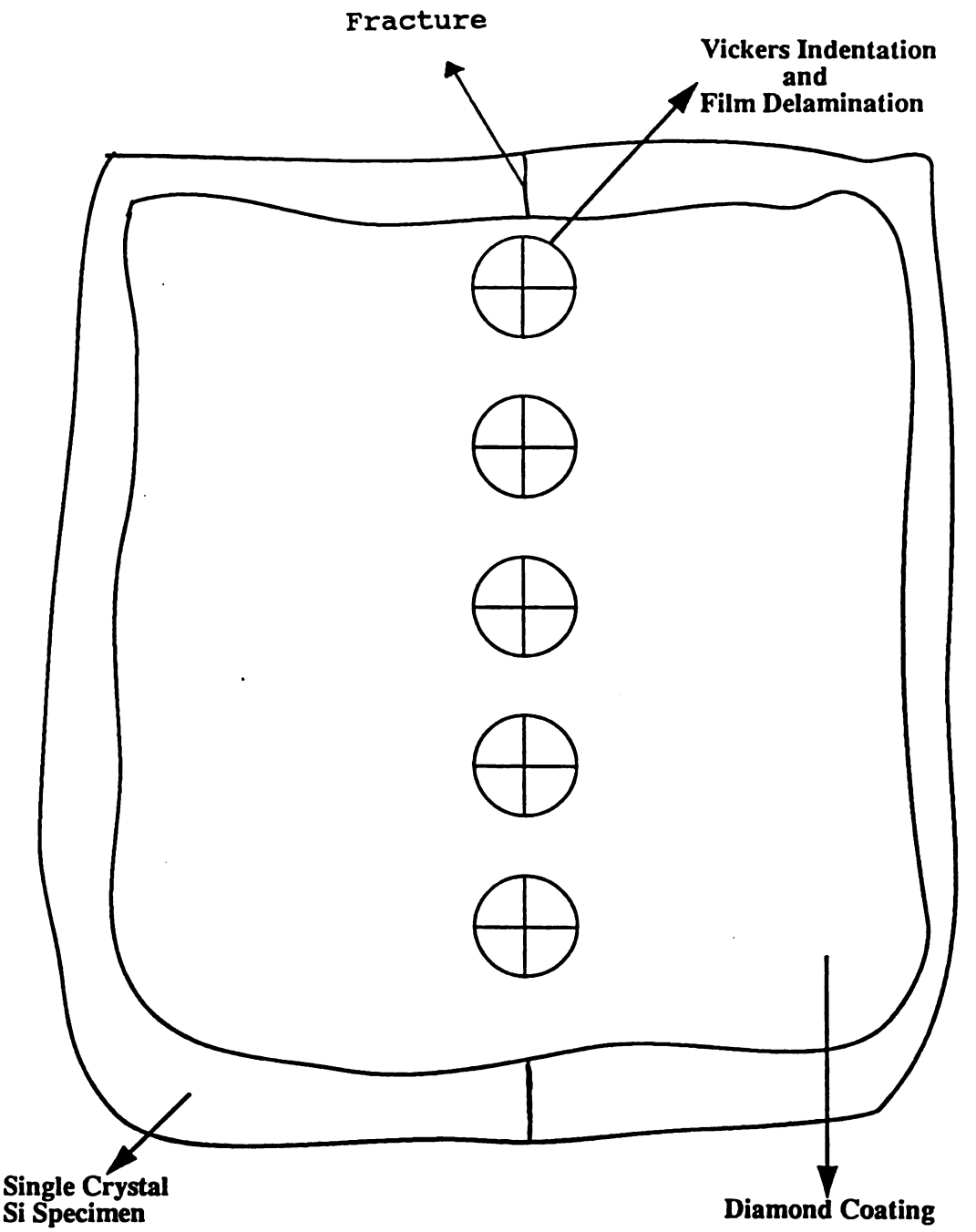

Figure 10a. Position of the delaminations analyzed with respect to fracture surface.

microns. The other four specimens exhibited a coating thickness between 2.2 and 2.7 microns.

Figure 9e, for the 1 percent methane/hydrogen processed specimens shows a general trend of increasing delamination diameter with respect to thickness. The adherence of the film to the silicon wafer therefore increases with the decreasing film thickness for the 0.5 percent and 1.0 percent processed specimens.

In figure 10b the average delamination diameter versus average film thickness was plotted for each specimen along with standard deviations. The average delamination diameter was calculated for each specimen from the delamination diameters corresponding to the indentation sites in table 5 and illustrated in figure 10a. Error bars representing the standard deviations for film thickness and average delamination diameter are also included. This figure does not exhibit a specific relationship between delamination diameter and thickness.

When considering the data from specimens processed at the same methane/hydrogen ratio, a decrease in delamination diameter is exhibited as the thickness of the coating is decreased. For specimens processed at the same methane/hydrogen ratio, the adherence of the film is therefore improved as the thickness of the coating decreases.

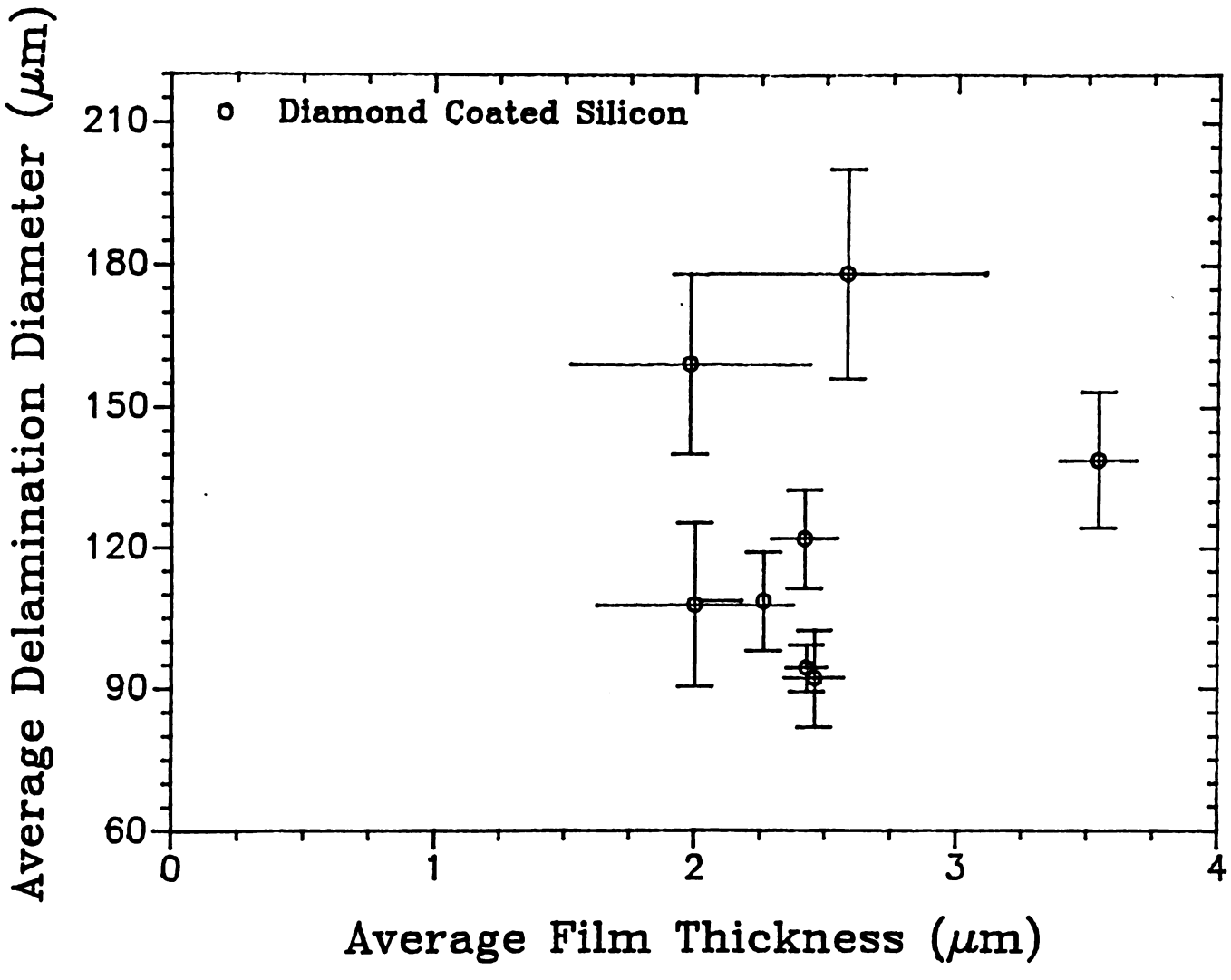

Figure 10b. Average delamination diameter versus average film thickness for all diamond coated specimens.

Table 5. Indentation Identification Numbers Corresponding to the Delaminations Used in the Analysis of the Data.

Specimen	Identification Numbers
NDFP1	13-23
NDFN13	11-14
NDFP13	5,10-13
WDF31	7,15-27
CP1	26-35
CP2	22-28
CP3	4,11,18,25,32,39,46
CP6	7-12

The adherence of the film also improves as the methane/hydrogen ratio is decreased. Again looking at the four 0.5 percent methane/hydrogen processed specimens, at a thickness of 2.5 microns the delamination diameters ranged from 80 to 140 μm. Also at the 2.5 micron thick region specimens CP1 and NDFP1, processed at 1.0 percent methane/ hydrogen, exhibited delamination diameters ranging form 140-210 microns. Specimen WDF31, which was produced at 0.67 percent methane/hydrogen, showed delamination diameters ranging from 85 to 155 microns, also at a thickness of 2.5 microns. Therefore at a constant film thickness of 2.5 microns, the adhesion of the film increased as the methane/hydrogen ratio decreased from one percent to 0.5 percent.

The improvement in adherence at 0.5 percent methane/hydrogen may result from an increase in thickness of the SiC interfacial layer that exists between the diamond coating and the silicon substrate. The slower deposition rate associated with the 0.5 percent methane/hydrogen ratio may allow more time for the plasma to react with the substrate, therefore producing a thicker SiC layer. Each specimen processed at 0.5 percent CH_4/H_2 ratio had a deposition time greater than six hours. Specimen NDFP1 processed at one percent CH_4/H_2 ratio had a deposition time of only four hours and the thickness of it's coating was greater than all the 0.5 percent CH_4/H_2 processed specimens

except CP3. In comparing values of the average deposition rate (average film thickness/deposition time) CP2 and CP6, processed at 0.5% CH_4/H_2, exhibited rates of 0.30 and 0.35 microns/hour respectively. Specimen NDFP1, processed at one percent CH_4/H_2, exhibited a deposition rate of 0.50 microns/hour.

A relationship between grain size and delamination diameter was also examined in this study. Table 6 includes the grain size and average delamination diameter for each specimen. Figure 11a is a plot of this data for the four specimens processed by the author. Figure 11b is a plot of the data for the four specimens processed by the Electrical Engineering Department and used in this investigation. Althouugh there are a large number of processing variabilities (table 2, table 7) during the production of diamond thin films both figures 11a and 11b exhibit a steady increase in average delamination diameter with respect to increasing grain size. Also if the two plots are superimposed it is interesting to observe that a very smooth line can be formed by displacing figure 11b approximately 0.7 microns in grain size to the right with respect to figure 11a. All of the data in table 6 was plotted in figure 11c and the linear equation $y = 36.602x + 74.55$, y representing the average delamination diameter and x representing the grain size, was fit to the data with a correlation coefficient of 0.819. Error bars representing

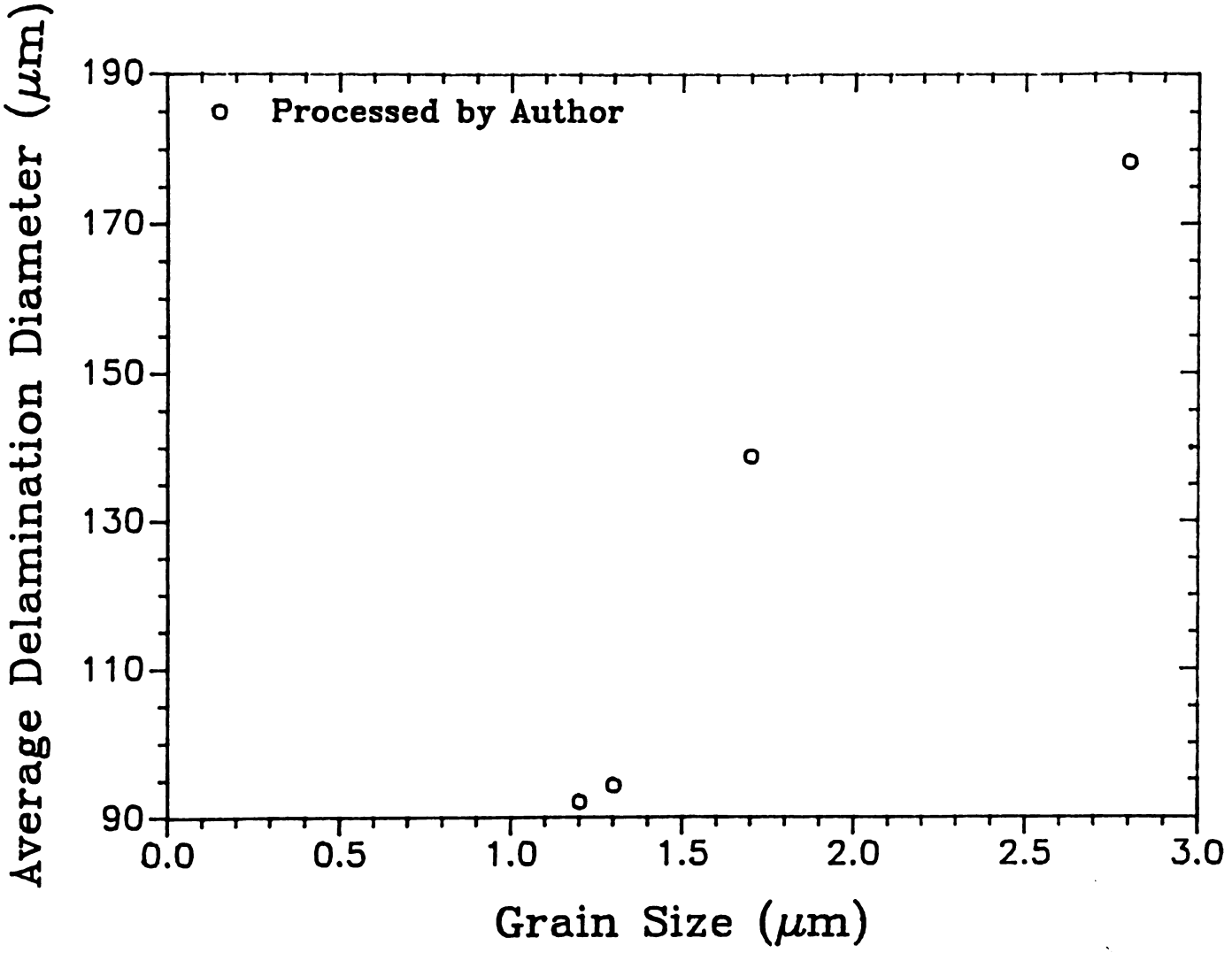

Figure 11a. Average delamination diameter versus grain size data for specimens processed by the author.

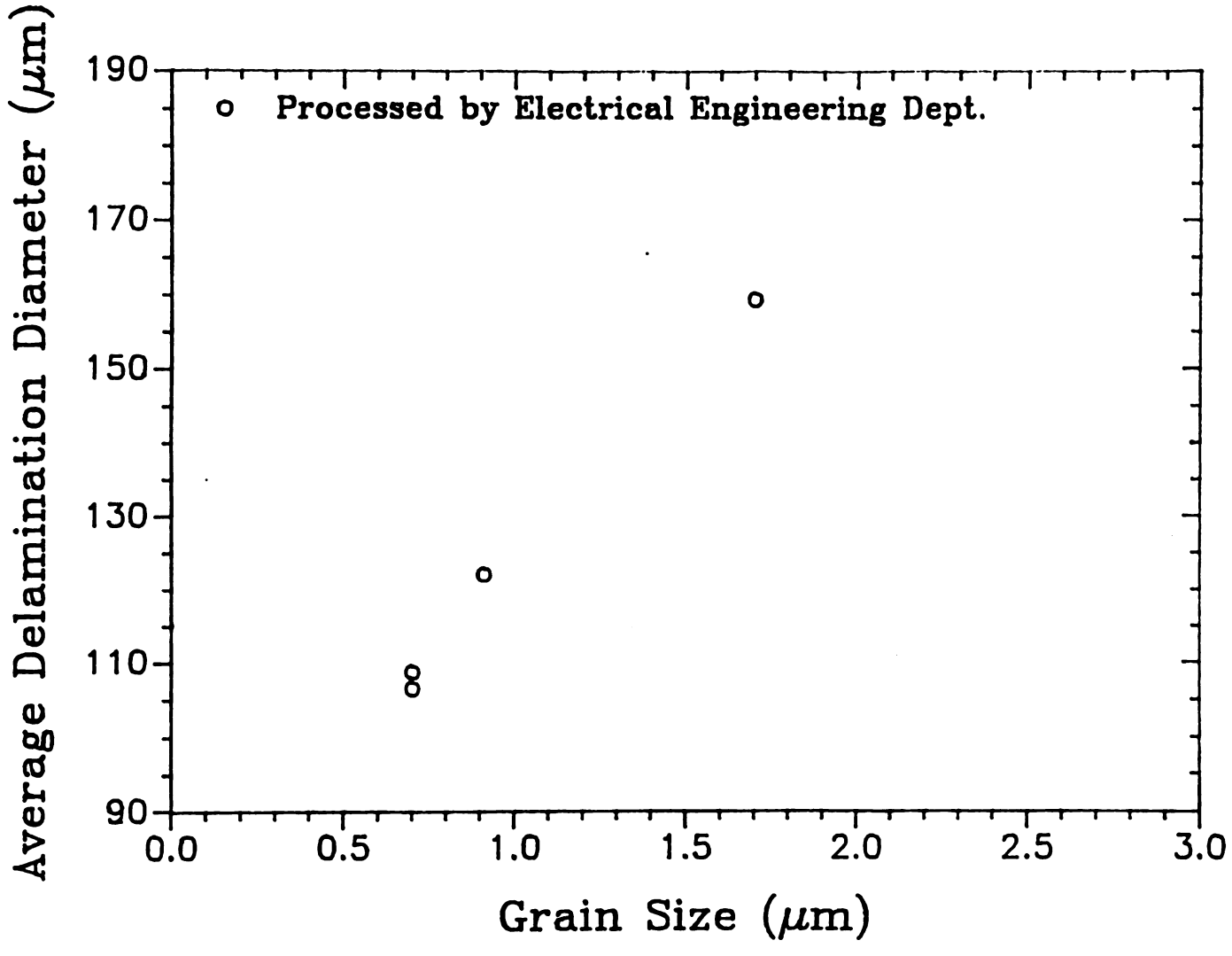

Figure 11b. Average delamination diameter versus grain size data for specimens processed by the Electrical Engineering Department.

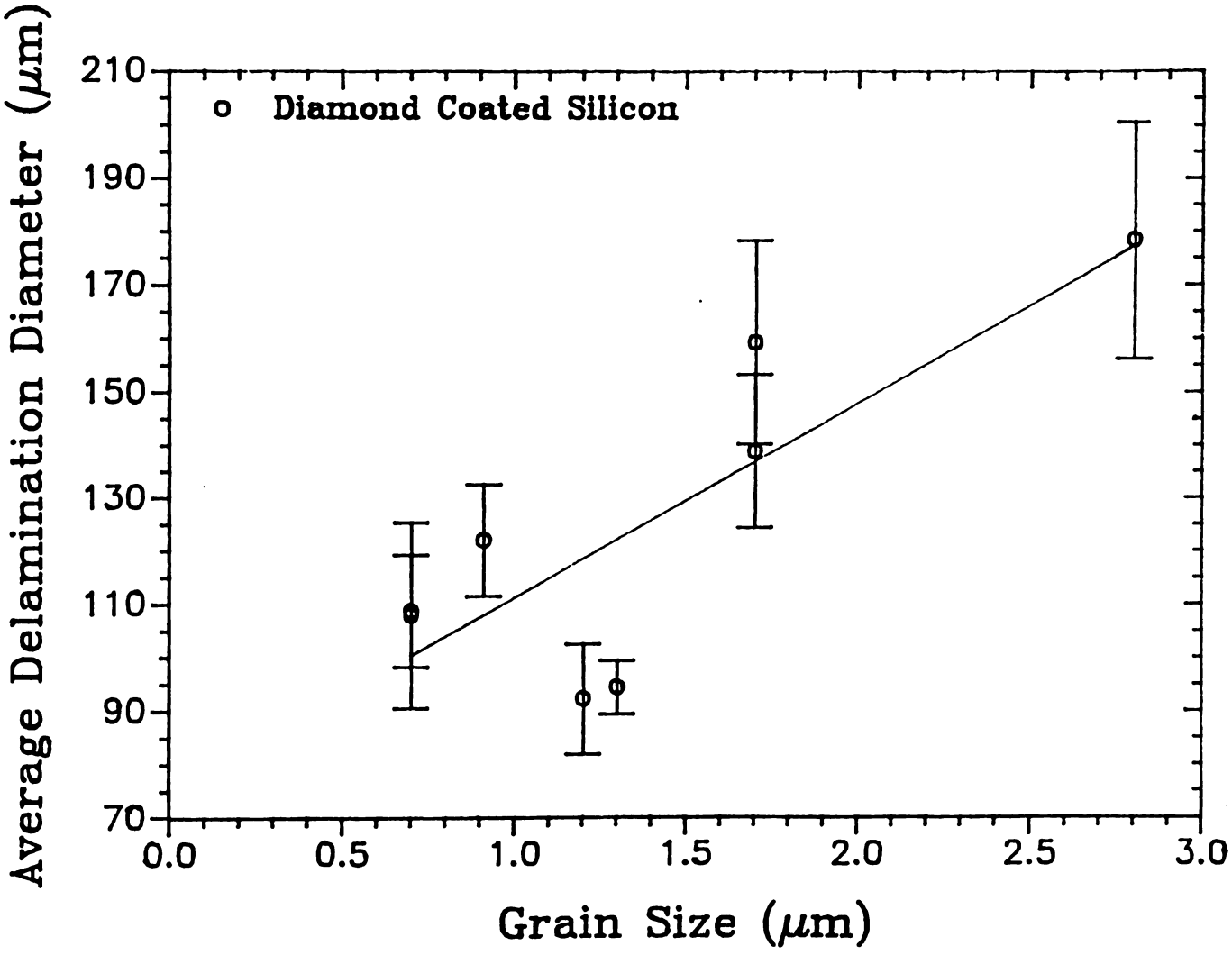

Figure 11c. Average delamination diameter versus grain size.

Table 6. Average delamination Diameter and Grain Size.

Specimen	a_{ave} (μm)	grain size (μm)
NDFP1	159.19	1.7
WDF31	106.37	0.7
NDFP13	108.60	0.7
NDFN13	121.93	0.9
CP1	178.27	2.8
CP2	94.23	1.3
CP3	138.77	1.7
CP6	92.01	1.2

the standard deviation for the average delamination diameter are also included. The average delamination diameter increases with increase in grain size. Thus the adherence of the diamond thin films to the silicon substrate is improved as the grain size of the diamond coating decreases.

As described by the Orowan and Petch relationships [50,76,77] the strength of a ceramic, being brittle and semibrittle materials, varies with respect to a change in grain size. The Orowan relationship is given by [77]:

$$\sigma_f = k_2 d^{-1/2} \qquad (21)$$

where σ_f = fracture strength

k_2 = a constant

d = grain size

Orowan's theory suggests that the size of initial flaws are limited by the grain size of the specimen [50]. Therefore smaller grain sized specimens are less likely to fracture. Petch's theory is based on the way in which the stress fields that form at the tips of microcracks interact with the grain boundries [50]. The grain boundries act as barriers where the stress builds up until the strength of the solid is overcome, resulting in fracture. Both the Orowan and Petch relaionships predict strength increases with decreasing $(\text{grain size})^{-1/2}$ [50].

The average delamination diameter for each specimen was then plotted with respect to (grain size)$^{1/2}$ (figure 12a). The error bars correspond to the standard deviations of the average delamination diameter. Figure 12a was then broken into two distinct plots: (1)figure 12b, specimens processed by the author, and (2) figure 12c, specimens processed by the Electrical Engineering department. For both figures 12b and 12c, linear regression was used to fit the general equation y = B(0) + B(1)x to the data, where y represents the average delamination diameter and x is the square root of grain size. For figure 12c B(0) = 17.67 $\pm$ 2.53 and B(1) = 108.75 $\pm$ 2.53. For figure 12b B(0) = -74.27 $\pm$ 31.0, B(1) = 153.66 $\pm$ 23.46, and the correlation coefficient was 0.977. The correlation coefficient for figure 12c was 0.999.

To check these values obtained for the intercept, B(0), and slope, B(1), of the figures 12b and 12c the four or five delamination diameter measurements listed in Appendix A for the indentation sites indicated in Table 5 were plotted with respect to (grain size)$^{1/2}$. Linear regression was then used to obtain the best fit linear equation to the data. For the specimens from the Electrical Engineering department, delamination diameter-(grain size)$^{1/2}$ data pairs were plotted. The correlation coefficient was 0.722 with B(0) = 25.97 $\pm$ 5.82 and B(1) = 88.36 $\pm$ 4.88. One hundred and fifty delamination diameter-(grain size)$^{1/2}$ data pairs were used in analyzing the data for the specimens processed by the author.

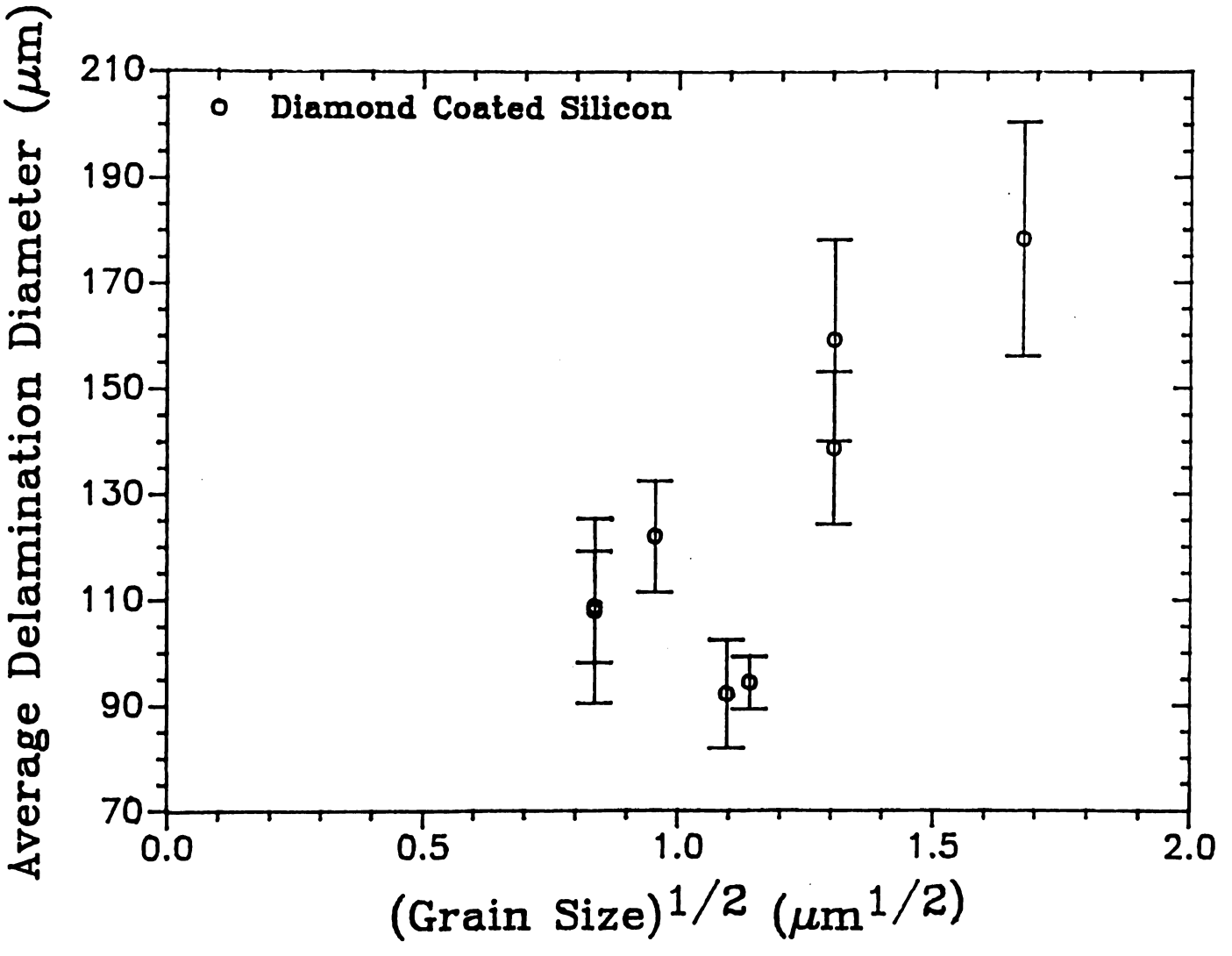

Figure 12a. Average delamination diameter versus the square root of grain size.

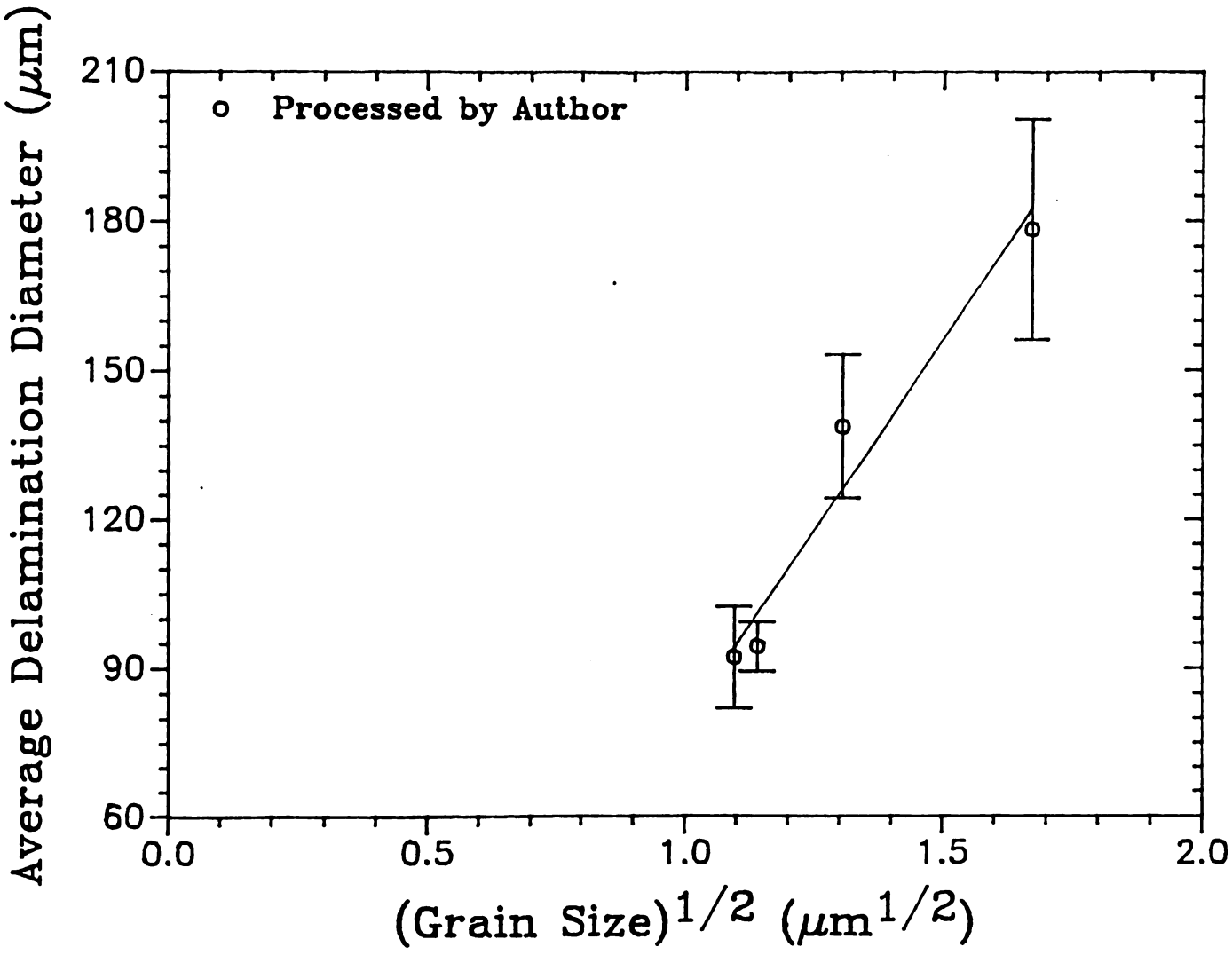

Figure 12b. Average delamination diameter versus the square root of grain size for specimens processed by the author.

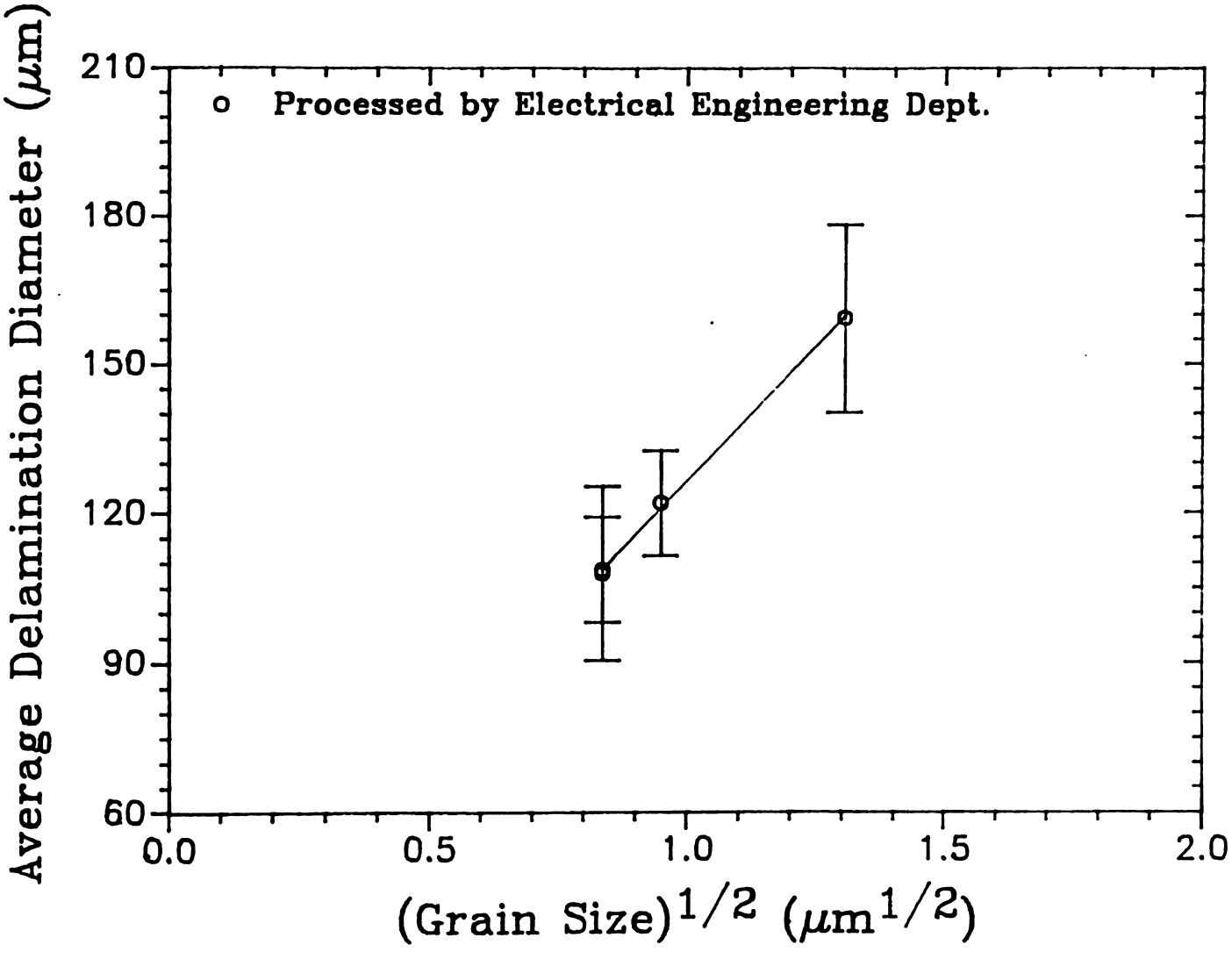

Figure 12c. Average delamination diameter versus the square root of grain size for specimens processed by the Electrical Engineering Department.

From this data a correlation coefficent of 0.90 was obtained with B(0) = -72.11 $\pm$ 8.23 and B(1) = 151.73 $\pm$ 6.02. The slope and the intercept values obtained for the two groups of specimens (processed by the author and processed by the Electrical Engineering department) indicate that there are definitely two distinct sets of parameters, one for each group of data.

The existence of two different equations to describe the data may result from changes in the processing variables. It is important to note that the specimens obtained from the Electrical Engineering Department were processed at least six months prior to those processed by the author. The difference in slope and intercept values could reflect alterations in the microwave plasma disk reactor system. With respect to processing variables, the outstanding difference between the two groups of data were that the gas flow rate during processing for the specimens from the Electrical Engineering department were higher than all the other specimens, as illustrated in table 7. The unit sccm means standard cubic centimeter.

The linear relationship between average delamination diameter and $(\text{grain size})^{1/2}$ might actually be the effect of residual stress. The residual stress associated with the smaller grains may be less than that of the larger grains and therefore cause the delamination size to be

Table 7. Flow Rates Used During Processing.

Specimen	H_2 (sccm)	CH_4 (sccm)
NDFP1	150	1.5
WDF31	300	2.0
NDFN13	250	1.25
NDFP13	250	1.25
CP1	100	1.0
CP2	100	0.5
CP3	100	0.5
CP6	100	0.5

smaller. Hence the improvement in adherence may be the result of a decrease in residual stress. However, no measurements of residual stress in the films were performed in this study, so that the possible connection between grain size and residual stress still needs to be established.

To determine if there is any underlying relationship between film thickness and grain size, a plot was made of average film thickness versus (grain size)$^{1/2}$ for all the specimens. This plot is shown in figure 13 along with error bars representing the standard deviations. There is no relationship exhibited between film thickness and (grain size)$^{1/2}$ when analyzing the combined data.

Although the Vicker's indentations produced successful delaminations one disadvantage to using this technique to study the adherance of the film is that breakage of the diamond tips occured. Both the indentor tip and the coating are diamond, but the surface of the coating was very rough which could result in damaging the tip. When indenting with a broken tip, non-circular delaminations, annular ring delaminations, or no delamination would result.

3.2 Fourier Transform Infrared Spectroscopy

Fourier transform infrared spectroscopy was used in the analysis of thermally shocked alumina specimens, indented zinc sulfide, indented silicon, indented diamond coated

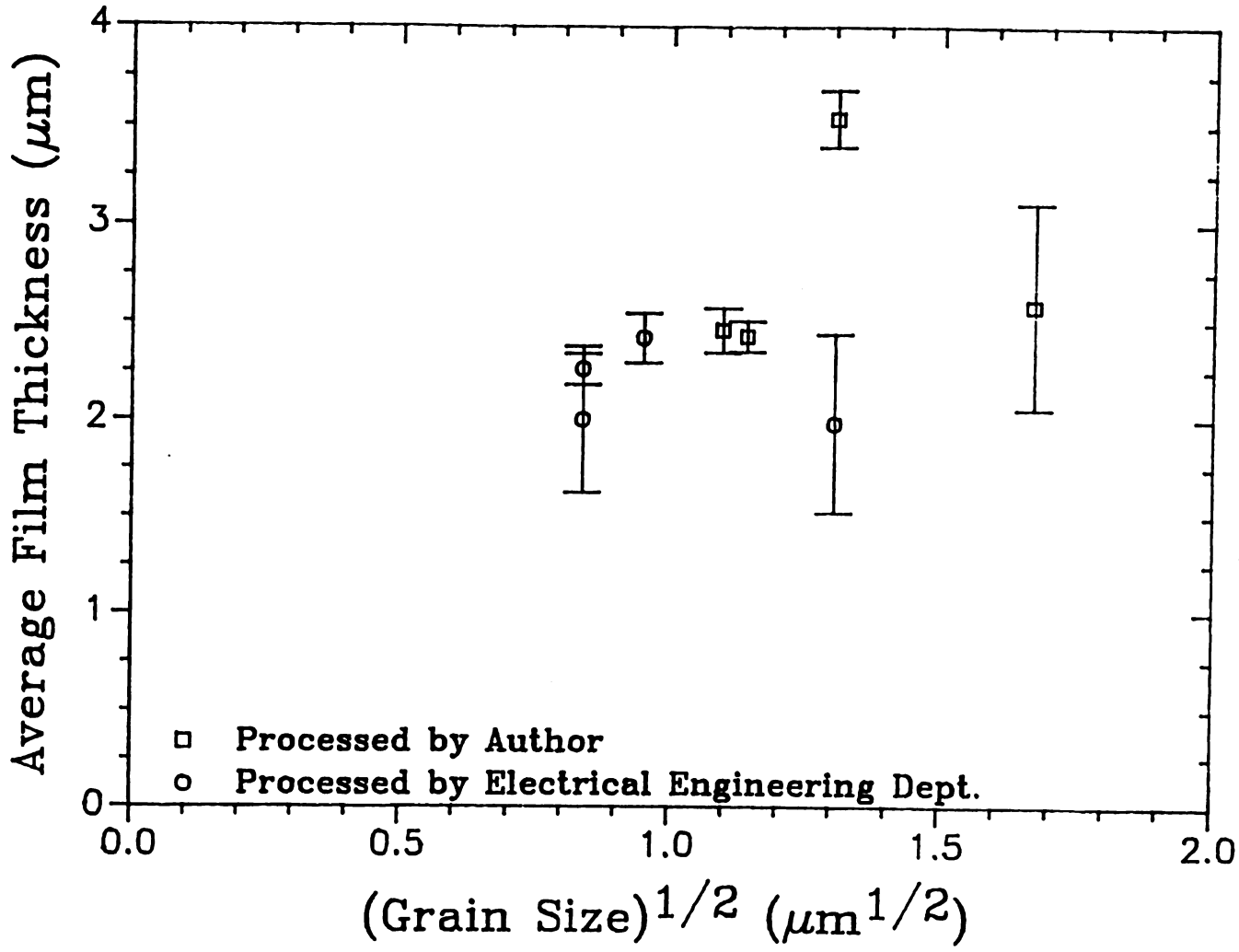

Figure 13. Average film thickness versus (grain size)$^{1/2}$.

silicon, water jet impacted zinc selenide, and side cracked zinc sulfide. Compared to the undamaged regions, there was a pronounced infrared scattering from the damaged regions for each specimen except the thermally shocked alumina specimens.

3.2.1 Alumina Specimens

Polycrystalline alumina specimen A5 was considered to have a large amount of damage, due to it's high ΔT (difference in temperature between furnace and water bath) value of 310° Celsius. To determine if the damage was concentrated in any specific area along the specimen, three different regions were tested, as specified in table 3 of section 2.2.3, in the FTIR Spectrophotometer. Comparing the three graphs of percent transmittance versus wavenumber for each region, we observed that the percent of radiation transmitted is generally the same at each region. The damage is therefore uniform along the specimen, since the transmittance values do not vary.

After 1, 3, 5, 10, 20, 40, 60, 80, and 100 thermal shock cycles, specimen C1 was tested in the FTIR spectrophotometer. Each time C1 was tested, a reference (undamaged) specimen was also tested. The ratio of percent transmittance of C1 to percent transmittance of REF was computed for each spectra obtained. It should be noted that after three thermal shock

cycles, part of specimen C1 broke off after regions one and two were tested. Therefore, only regions one and three were tested for the remaining cycles, but region two was not tested after the first three cycles.

From the two graphs obtained for region two, an increase was exhibited, between one and three cycles of transmitted radiation. For region one, the radiation transmitted increased slightly after three cycles and then decreased after five and ten cycles. The amount of transmitted radiation then increased after 20 thermal shock cycles and continued to alternate between increasing and decreasing for the remaining cycle increments. In reference to the graphs for region three, the change in transmittance was negligible in comparing all the spectra obtained.

After one hundred thermal shock cycles, C1 and the reference specimen were also scanned at a 10, 12, and 20 degree angle θ. The ratios were again computed for percent transmittance of C1 to percent transmittance of REF. Comparing the graphs of transmittance versus wavenumber the transmittance at normal incidence was greater then that for the ten, twelve, and twenty degree angle. One possible reason for this observed decrease, is that the IR beam may encounter a larger crack area when the specimen is tilted at an angle. This would result in a greater amount of scatter of the IR beam and therefore decrease the amount of infrared radiation transmitted.

Additional angles of 2.0, 5.0, and 7.5 degrees were tried for the alumina specimens. In comparing the spectrums of each angle with that at normal incidence, a slight decrease was exhibited in the ratioed transmittance when tested at an angle. The lowest percentage of transmittance was exhibited at 5.0^{o}.

3.2.2 ZnS, ZnSe, Silicon, and Diamond Coated Silicon Specimens

There was a significant amount of infrared scattering from the damaged zinc sulfide, zinc selinide, silicon, and diamond coated specimens. Infrared spectra obtained for the damaged regions in the range of 4000 to 700 cm^{-1} wavenumbers were ratioed to undamaged regions for further anlysis and interpretation. The ratioed data for the impacted zinc selinide specimen contained transmittance values above 1.0. This data was therefore not analyzed.

By ratioing the transmittance from a damaged region to an undamaged region a value for relative transmittance, τ_R was obtained. Since transmittance values were obtained for each wavenumber between 4000 and 700 cm^{-1} an average value for transmittance for ten consecutive wavenumbers at 98 wavenumber intervals was calculated to aid in analyzing the data. Thirty-four pairs of wavenumber-transmittance pairs were used in the data analysis.

As discussed in section 1.2.2, Kodre and Strand [56]

used the following equation for the transmissivity of an air gap.

$$T_p = 1/(A_p \sinh^2 z + 1) \tag{13}$$

According to Good and Nelson [78]

$$|E_T/E_i|^2 \sim \alpha^2 \tag{22}$$

where E_t = the transmitted wave

E_i = the incident wave

since $\alpha^2 = e^{-2Kd/r}$ (23)

with $r = \sin^2 i - \sin^2 i_o$

where d = thickness of the air gap

i = incident angle

i_o = critical angle

$k = 2\pi\nu$

with ν = wavenumber

when kd/r is large then

$$r_R \sim \alpha^2 \tag{24}$$

from equations (22) and (23) we see that an appropriate trial function for linear regression of the infrared data obtained in this investigation was:

$$r_R = C_1[\exp(-C_2\nu)] \qquad (25)$$

where C_1 = a constant

C_2 = a constant

C_1 and C_2 were determined using a nonlinear least squares fit program devloped by Dr. Eldon Case (Associate Professor, Michigan State University, E. Lansing, MI). Table 8 contains the infrared spectra file name along with the C_1 and C_2 parameters. Appendix B contains a description of the locations where each spectral file was obtained. Also included in table 8 is the correlation coefficient, r, for each curve fitting. A correlation coefficient of 1.0 would represent a perfect fit. Comparing the fit among the IR scattering data for the damaged specimens, the side-cracked zinc sulfide specimen exhibited the best fit to equation (25), with a correlation coeficient of 0.997.

Table 8. Curve Fitting Parameters and Correlation Coefficient for the infrared spectra.

File	C_1	C_2	r
SCZS	0.9178	9.1918	0.997
IZS50	0.9356	0.8487	0.862
NP1NI6	0.2396	4.0164	0.945
WDI11	0.5897	3.5678	0.976
FSI2	0.8293	1.6300	0.987
FSR2	0.9426	0.4627	0.946
FSN2	0.9694	0.4669	0.940
2ZS50	1.1766	9.1462	0.984

Plots of the relative IR transmittance versus wavenumber for each of the damaged specimens are shown in figures 14a-14f along with their corresponding regression curve. In figure 14a the experimental data for the side-cracked zinc sulfide forms a very smooth curve to which the exponential equation fits well. In comparing the plots of the indented zinc sulfide and silicon (figures 14b and 14e) the data points are displaced from the curve at 0.16 μm^{-1}, 0.23 μm^{-1}, and 0.36 μm^{-1} for both specimens. This may be related to the indentation impression itself, since this type of disturbance is not illustrated in the plots for the delaminated diamond coated silicon. The alternating increase and decrease in relative transmittance for the diamond coated specimens with respect to the best fit curve, in figures 14c and 14d, may be the effect of the delamination on the transmitted infrared radiation.

In figure 14e the data corresponding to indentation number 2 for the indented silicon specimen is illustrated. In this figure, the spectra taken while centering the infrared microscope above the indentation impression, exhibits a large decrease in transmittance as compared to the other two regions. This is due to the high amount of scattering from the indentation impression.

In reference to the displaced data points for the indented specimens from the best fit curve, a study conducted by G. White and J. F. Machiando [79] may explain these

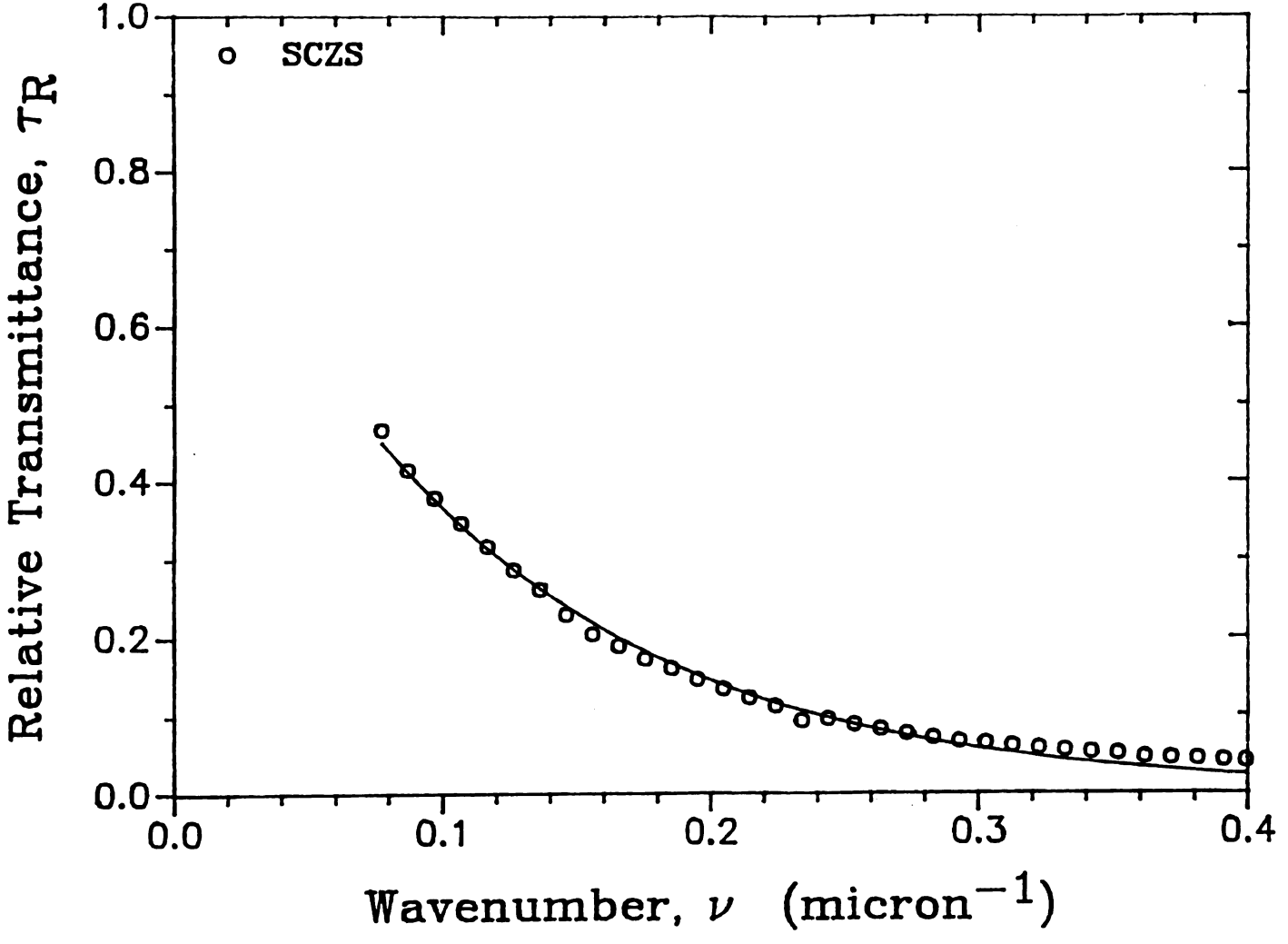

Figure 14a. Relative transmittance versus wavenumber data for SCZS.

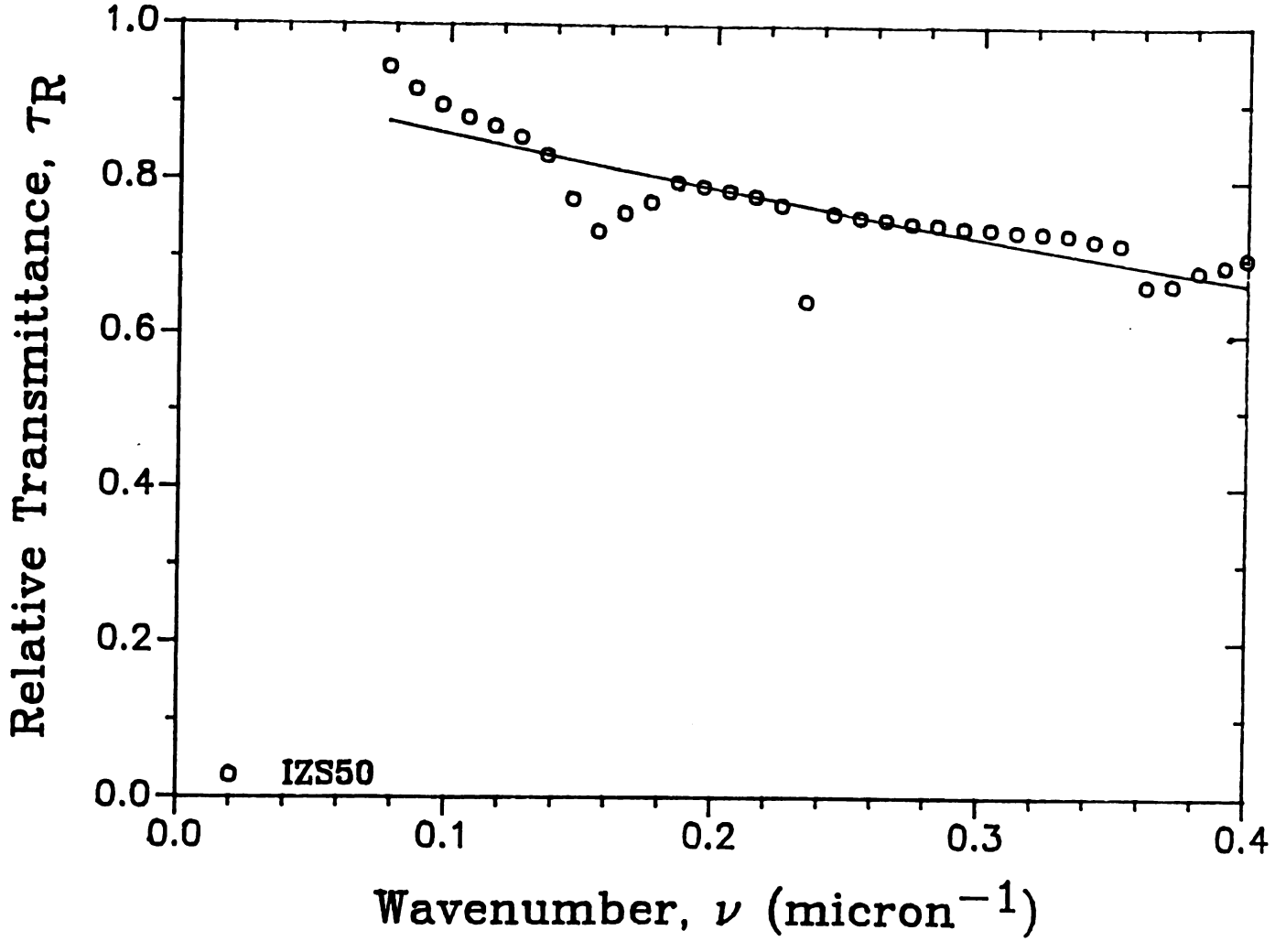

Figure 14b. Relative transmittance versus wavenuber data for IZS50.

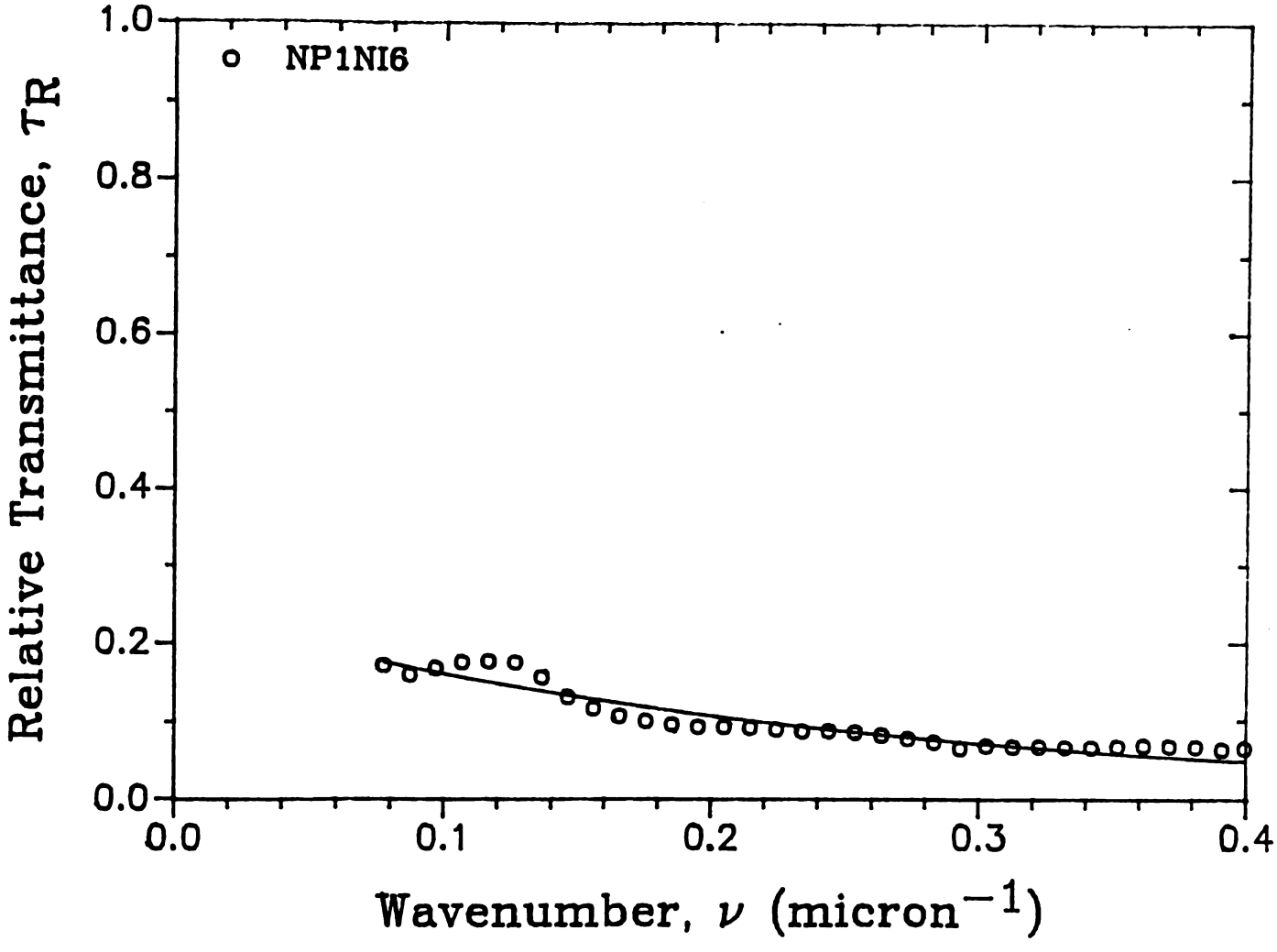

Figure 14c. Relative transmittance versus wavenumber data for NP1NI6.

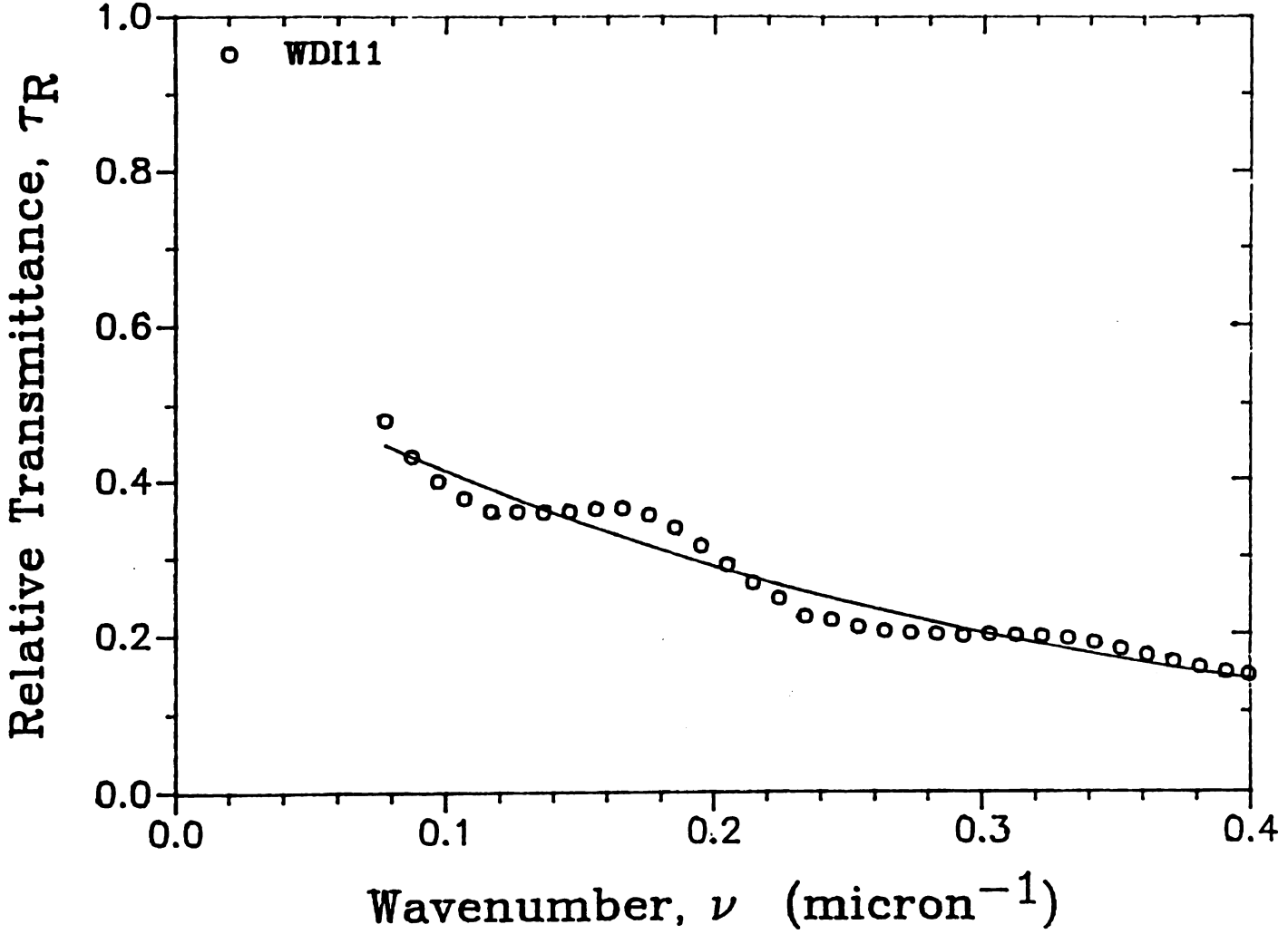

Figure 14d. Relative transmittance versus wavenumber data for WDI11.

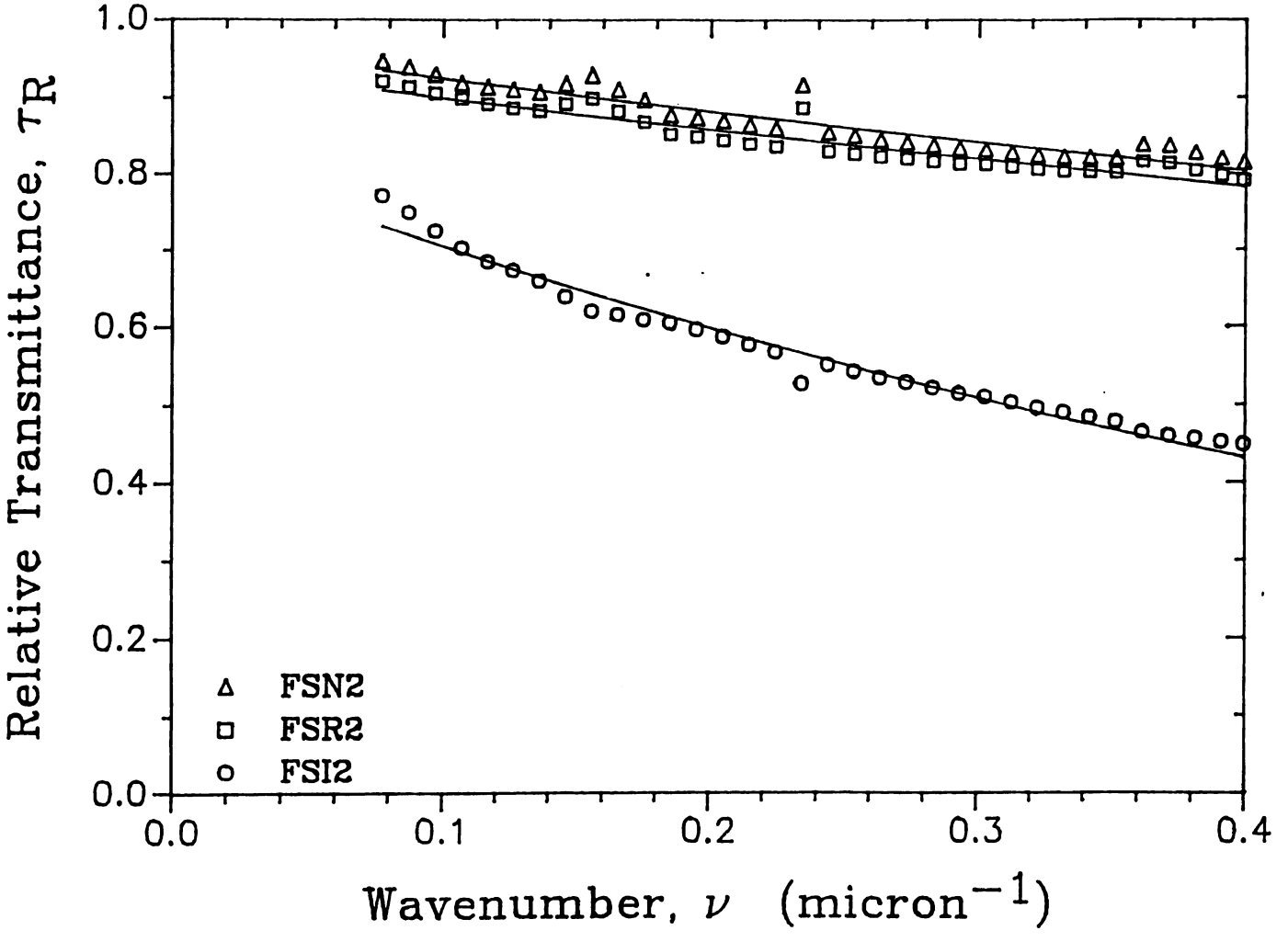

Figure 14e. Relative transmittance versus wavenumber data for FSN2, FSR2, and FSI2.

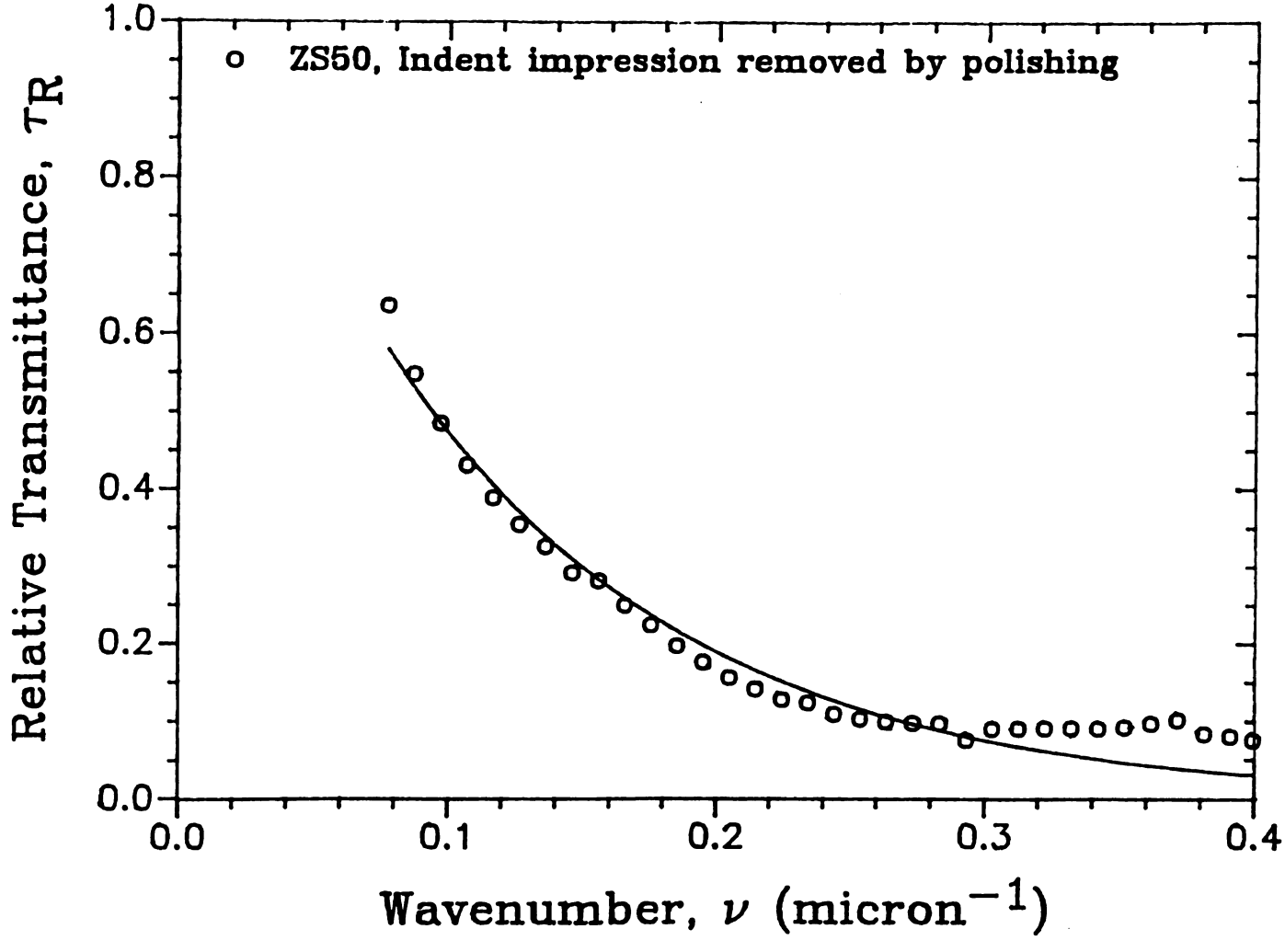

Figure 14f. Relative transmittance versus wavenumber data for 2ZS50.

values. White and Machiando measured radiation scattered from a V-shaped groove on a conductor in the resonance domain and compared these values to theoretical work developed by Maystre [80]. In the investigation a CO_2 laser producing infrared radiation with a 10.53 micron wavelength was utilized. The infrared radiation was incident on a vertically oriented V-shaped groove which was induced in a brass plate by diamond scribing. The depth of the groove was approximately equal to the wavelength of the radiation and the width was about three times the wavelength. Infrared radiation was detected by a piezeolectric detector which was passed at a constant radius at a plane normal to the groove length from -90^{o} to 80^{o}. A graph of the scattering was plotted which exhibited various peaks in intensities with respect to the scattering angle [79]. The position, number, and size of the peaks was determined to depend on the coarse features (width and depth) of the groove. The bottom of the V-shaped groove was relatively flat. Small variations in position and significant changes in peak size were the result of small variations in the deformed metal along the groove edge. White and Machiando also concluded that the theory accurately predicts the scattering observed in the resonance domain [79].

In this study infrared radiation in the wavelength range of 2.5 to 12.5 microns was utilized. The diamond indentation impression had a point to point width of 306.65 μm for the

zinc sulfide specimen and 45.55 μm for the silicon specimen. Since the angle of the Vicker's indentor tip was known (148^{O}), using trigonometry the depth of the indentation impression was calculated to be approximately 6.52 μm for the silicon and 43.97 μm for the zinc sulfide specimen. It should be noted that these calculated values are only approximations and may be over estimations if elastic recovery occurred. To experimentally determine if the displaced data was actually peaks resulting from radiation scattered from the indentation impression on the surface of a dielectric, the indentation impression was removed by polishing on the zinc sulfide specimen and the specimen was tested again. The infrared spectra obtained after removal of the indentation impression is shown in figure 14f, for 2ZS50. In comparing figure 14f with 14b we observed that the curve has become smooth with the removal of the indentaion impression and an increase in the correlation coefficient is obtained during the curve fitting. Therefore the data points displaced from the curve in figure 14b may result from IR scattering by the indentation impression.

In order to determine the crack opening displacement value for the indented silicon specimens, the power of the exponential in equations (23) and (25) were set equal to each other, since the relative transmittance is proportional to α. Thus,

$$C_2 \upsilon = 4\Pi\upsilon d/r \qquad (26)$$

where $r = \sin^2 i - \sin^2 i_o$

The crack opening displacement, d, is then given by:

$$d = C_2/[(4\pi)\sqrt{r}] \qquad (27)$$

The critical angle for silicon is 16.8^o. Using the C_2 value for FSN2, given in table 8, for incident angles ranging from $17\text{-}20^o$ the crack opening displacement ranged from 0.842-0.203 microns respectively. Using the C_2 values for FSI2, incident angles from 17 to 20 degrees result in a crack opening displacement of 2.94 - 0.709 microns. The theoretical values obtained were calculated using the air gap model to describe the loss in transmittance.

In order to compare theoretical and experimental crack opening displacement values, an indented silicon specimen, Si1, was fractured along a row of indentations observed in the SEM. Micrographs were taken of the lateral crack and measurements were made. Under the center of the indentation impression values of the crack opening displacement ranged from 0.9 to 2.7 microns. As the crack progressed away from the indentation impression the crack opening displacement ranged from 0.85 to 2.15 microns. Although the size of the crack could be altered by fracture of the specimen, the

experimental values obtained agree well with those calculated theoretically, for the FSI2 data. Theoretical values calculated for the crack opening displacement using FSN2 data predicted a smaller value than those obtained experimentally.

It is important to note that when testing the specimen in the FTIR spectrophotometer, specimen Si1 was first tested. This specimen was not cleaned before obtaining the infrared spectra and as a result there was a large amount of noise exhibited in the 1300 to 1950 wavenumber (cm^{-1}) range. By using the RCA cleaning procedure on Si2, previously discussed in section 2.1.1, the noise in the spectra was reduced significantly.

4.0 Conclusions

Diamond thin films have a wide variety of potential applications but their use has been limited due to poor adhesion of the films. In this investigation properties which affect the adherence of diamond thin films to silicon wafers were examined. Also in this investigation the damage sustained by ceramics in point contact loading was characterized using the Fourier Transfom Infrared Spectrophotometer as a nondestructive tool.

Diamond thin film silicon substrates were successfully produced in a microwave plasma disk source reactor. The films produced at a 0.5-1.0 percent methane/hydrogen ratio, exhibited a 0.7-2.8 micron grain size and were 1.0-4.0 microns thick. Vicker's indentaion on the specimens was shown to be a quick and easy method to determine the adherence of the coatings on the silicon wafers. One disadvantage of this method though, is the increase in indentor tip failure when indenting on rough diamond coatings.

Delamination diameters showed negligible change for up to a few weeks after the initial delaminations were made. The residual stress fields associated with diamond thin film deposition and Vicker's indentation therefore do not result in sufficient slow crack growth to change the delamination size as a function of time.

Adherence of diamond thin film coatings to silicon wafers is a function of film thickness, methane/hydrogen ratio used during processing, and grain size of the coating. At a constant methane/hydrogen processing ratio, the adherence of the films is improved as the thickness of the coating is decreased. Adherence of the diamond thin film coatings, at a constant thickness, is also improved as the methane/hydrogen processing ratio is decreased from 1.0 to 0.5 percent.

Considering the three factors (grain size, CH_4/H_2 processing ratio, and film thickness) which affect the adherence of the films, grain size of the coatings has the most significant influence on the adherence. A linear relationship exists between the delamination diameter and $(\text{grain size})^{1/2}$ of the diamond thin film. As $(\text{grain size})^{1/2}$ decreases, the adherence of the diamond thin film to the silicon substrate is improved.

In using the FTIR spectrophotometer as a nondestructive tool to characterize the damage in thermally shocked alumina specimens the infrared scattering from the specimens was negligible when one to three IR scans were made per run.

Relative transmittance of infrared radiation was obtained for indented silicon, indented zinc sulfide, delaminated diamond thin films on silicon wafers, and a zinc sulfide specimen containg cracks from compression. The equation $\tau_R=C_1\exp(-C_2\upsilon)$ exhibited a good fit to the

relative transmittance versus wavenumber data. Data points that are displaced from the curve are due to infrared radiation scatter from the indentaion impression.

Using the C_2 parameter obtained in the curve fitting, theoretical values for the crack opening displacement were determined. The experimental value for the crack opening displacement in silicon agreed well with that calculated theoretically.

Based on this investigation, it is recomended that submicron diamond coatings should be used in order to obtain the best possible adherence of the film. Fine grain films, having a smoother surface should be the focus of future adhesion studies using Vicker's indentation. This also might reduce the rate of indentor tip failure. The FTIR spectrophotometer has successfully been used to study the damage in ceramic materials, but further work on the characterization of the damage is needed.

APPENDIX A

Indentation Data

Table A1. Delamination Diameter Measurements for NDFP1.

Indentation Identification Number	a_1 (μm)	a_2 (μm)	a_3 (μm)	a_4 (μm)	a_{ave} (μm)
1	124.5	132.7	129.1	117.2	125.98
2	144.8	152.6	145.5	153.0	148.98
3	142.3	147,6	144.8	144.3	144.75
4	174.4	176.1	163.6	161.1	168.80
5	169.2	178.6	169.9	168.7	171.60
6	172.9	181.7	173.6	171.0	174.80
7	171.4	164.2	165.8	163.2	166.15
8	166.3	158.8	162.2	172.4	164.93
9	158.5	157.0	159.5	153.9	132.23
10	136.9	137.0	136.8	136.3	136.75
11	140.3	144.9	142.8	145.5	143.38
12	126.7	121.1	121.2	105.0	118.50
13	120.3	112.9	112.0	116.3	115.38
14	123.8	165.4	140.6	138.1	141.98
15	160.8	151.9	142.3	148.7	150.93
16	175.0	182.6	176.0	178.8	150.90
17	180.1	177.5	175.1	168.8	175.38
18	181.2	177.8	169.8	178.1	176.73
19	175.1	168.4	170.0	170.5	171.00
20	175.1	173.4	159.8	179.7	171.83
21	171.5	151.0	152.2	156.6	157.83
22	139.6	149.7	142.9	129.7	140.46
23	179.7	177.6	178.5	149.9	171.42

APPENDIX A (continued)

Table A2. Delamination Diameter Measurements for WDF31.

Indentation Identification Number	a_1 (μm)	a_2 (μm)	a_3 (μm)	a_4 (μm)	a_5 (μm)	a_{ave} (μm)
1	125.8	109.6	134.4	120.5	120.6	122.2
2	93.0	81.9	82.6	78.4	82.2	83.6
3	97.6	79.7	101.1	96.3	97.8	94.5
4	111.6	99.0	122.1	107.1	119.2	111.8
5	72.3	75.0	81.6	77.4	74.2	76.1
6	68.2	78.4	72.0	76.4	77.2	74.4
7	90.0	93.7	95.9	78.7	82.6	88.2
8	77.6	77.4	78.2	74.3	75.8	76.2
9	80.0	72.9	78.8	74.3	79.1	77.0
10	79.7	82.9	84.7	89.9	90.8	85.5
11	100.2	98.5	100.9	93.1	86.4	95.8
12	97.8	96.5	93.5	91.7	93.0	94.5
13	74.8	82.6	79.7	82.1	74.3	78.7
14	170.5	107.3	110.9	104.9	96.7	118.0
15	93.0	84.3	89.7	94.8	107.5	93.9
16	85.7	86.2	88.7	82.8	91.2	86.9
17	84.2	79.9	98.8	100.0	99.9	92.6
18	130.0	122.7	116.0	127.4	126.8	124.6
19	126.8	112.7	125.7	132.0	135.9	126.6
20	102.7	103.2	96.8	97.0	93.3	98.6
21	105.4	96.5	112.9	115.3	123.9	110.8
22	103.5	105.0	97.8	91.3	99.0	99.3
23	102.4	105.2	96.2	99.4	98.4	100.3
24	91.6	91.8	91.8	116.5	107.8	99.9
25	110.8	124.5	128.1	121.5	124.4	121.9
26	95.6	90.5	101.0	99.1	86.0	94.4
27	185.2	158.6	145.7	135.5	131.0	151.2

APPENDIX A (continued)

Table A3. Delamination Diameter Measurements for NDFP13.

Indentation Identification Number	a_1 (μm)	a_2 (μm)	a_3 (μm)	a_4 (μm)	a_5 (μm)	a_{ave} (μm)
1	130.1	141.5	121.2	128.8	122.4	128.8
2	138.0	137.8	120.3	136.1	136.8	133.8
3	112.2	109.2	113.8	110.3	110.7	111.2
4	147.7	157.6	135.8	148.2	132.2	144.3
5	126.6	120.1	128.2	127.1	121.1	124.6
6	123.9	123.9	114.8	137.1	115.7	123.1
7	107.3	119.0	105.8	108.8	106.9	109.6
8	133.6	135.8	125.8	117.8	116.0	125.8
9	98.9	105.3	98.6	100.8	107.3	102.2
10	128.1	116.8	104.8	121.5	99.1	114.1
11	114.6	111.2	101.6	108.2	99.3	107.0
12	95.8	101.6	78.1	94.9	92.1	92.5
13	107.9	110.6	108.8	105.3	91.6	104.9

APPENDIX A (continued)

Table A4. Delamination Diameter Measurements for NDFN13.

Indentation Identification Number	a_1 (μm)	a_2 (μm)	a_3 (μm)	a_4 (μm)	a_5 (μm)	a_{ave} (μm)
1	112.4	116.6	105.9	109.6	104.3	109.8
2	131.1	122.5	142.3	117.5	134.3	129.5
3	108.6	115.9	115.0	109.2	102.4	110.2
4	110.7	110.7	96.8	105.6	96.6	104.1
5	91.0	96.6	101.8	92.4	91.3	94.6
6	178.6	161.3	194.3	138.5	153.1	165.2
7	183.5	157.9	153.7	150.6	174.7	164.1
8	150.0	146.4	138.2	153.6	144.9	146.2
9	126.0	142.6	112.2	123.4	136.6	128.2
10	151.0	164.5	118.5	140.4	130.1	140.9
11	147.7	133.6	98.3	110.5	101.3	118.3
12	113.6	116.9	132.1	106.4	106.6	115.1
13	117.1	95.9	112.2	100.4	107.7	106.7
14	151.3	143.6	129.4	146.5	129.8	140.1

Table A5. Delamination Diameter Measurements for CP1.

Indentation Identification Number	a_1 (μm)	a_2 (μm)	a_3 (μm)	a_4 (μm)	a_5 (μm)	a_{ave} (μm)
1	136.6	136.6	111.7	126.2	124.2	127.06
2	112.8	111.3	114.3	119.5	116.8	114.94
3	117.2	119.1	117.3	113.6	117.1	116.86
4	136.4	132.8	141.7	123.0	134.4	133.66
5	122.3	121.1	124.2	120.8	122.3	122.14
6	123.7	122.3	120.1	118.7	118.3	120.62
7	139.9	126.0	133.0	131.6	132.9	312.68
8	146.6	126.7	136.2	133.0	140.6	136.62
9	132.5	123.5	132.2	125.8	127.3	128.26
10	127.5	126.7	124.3	123.0	125.5	125.40
11	140.6	134.5	137.6	138.3	142.1	138.62
12	118.3	109.2	116.9	106.1	110.7	112.24
13	128.3	123.0	122.8	127.5	127.8	125.88
14	133.9	136.2	136.5	139.1	138.4	136.82
15	116.6	118.3	118.2	123.6	120.4	119.38
16	92.9	100.1	94.9	101.1	90.1	95.82
17	88.9	92.3	87.9	90.9	90.2	90.04
18	79.9	81.0	77.8	72.5	72.8	76.80
19	78.1	71.8	73.4	74.3	74.8	74.48
20	115.7	108.9	115.3	111.7	112.5	112.82
21	125.7	123.0	117.0	122.2	127.3	123.04
22	106.7	106.1	110.4	109.7	117.8	110.14
23	101.5	100.5	100.9	103.5	102.8	101.84
24	109.1	106.2	116.7	104.5	111.5	109.60
25	*					
26	168.8	168.1	163.3	164.6	167.3	166.40
27	188.3	188.8	196.9	173.2	184.6	186.40
28	216.1	217.0	204.9	205.6	217.5	212.20
29	189.3	196.9	186.5	180.1	188.2	188.20
30	182.7	187.8	177.9	179.5	177.9	181.20

* No Delamination

Table A5. (continued)

Indentation Identification Number	a_1 (μm)	a_2 (μm)	a_3 (μm)	a_4 (μm)	a_5 (μm)	a_{ave} (μm)
31	166.0	164.7	169.3	165.9	165.6	166.30
32	179.3	188.7	186.3	183.5	179.1	183.40
33	210.8	192.1	203.6	209.3	214.9	206.10
34	145.9	148.4	149.4	135.8	143.3	144.60
35	145.3	151.8	145.5	151.8	140.2	146.90
36	167.0	162.2	166.0	163.0	163.9	164.40
37	188.4	192.8	182.2	197.5	191.8	190.50
38	186.1	183.1	183.1	183.8	183.5	183.90
39	168.4	171.9	170.6	171.5	162.4	169.00
40	170.2	166.1	171.9	169.6	165.4	168.60
41	172.8	180.1	168.9	175.2	176.0	174.60
42	179.8	173.5	179.5	170.4	174.0	174.60
43	171.0	177.9	167.5	179.3	179.8	175.10
44	156.1	165.4	155.8	159.5	155.2	158.40
45	142.7	136.6	142.9	132.4	140.5	139.00

APPENDIX A (continued)

Table A6. Delamination Diameter Measurements for CP2.

Indentation Identification Number	a_1 (μm)	a_2 (μm)	a_3 (μm)	a_4 (μm)	a_5 (μm)	a_{ave} (μm)
1	86.3	73.3	83.4	82.9	87.8	82.74
2	82.4	81.1	78.7	83.3	87.0	82.50
3	105.6	105.9	105.7	104.4	102.9	104.90
4	97.1	94.5	92.3	90.7	93.7	93.66
5	91.2	90.0	82.6	94.1	92.6	90.10
6	63.9	66.8	67.4	66.4	67.0	66.30
7	77.7	68.1	76.1	76.9	71.4	74.04
8	99.6	84.9	93.0	82.4	94.7	90.92
9	92.4	83.9	91.8	86.3	87.1	88.30
10	92.2	93.7	89.0	90.3	85.3	90.10
11	79.0	86.0	86.5	82.1	77.6	82.24
12	96.9	92.9	93.8	91.5	95.4	94.10
13	90.2	84.7	86.6	90.3	89.8	88.32
14	98.9	93.8	99.6	102.8	100.1	99.04
15	82.5	86.2	86.4	82.1	85.1	84.46
16	92.7	91.1	95.5	92.0	91.9	92.64
17	79.5	82.9	82.1	79.9	80.3	80.94
18	93.6	88.6	88.9	92.8	95.1	91.80
19	109.2	110.2	102.8	116.4	113.8	110.48
20	94.3	94.5	94.4	91.7	92.0	93.38
21	76.4	74.9	74.2	74.1	75.0	74.92
22	84.3	85.5	81.7	82.5	83.9	83.58
23	87.1	91.8	90.7	93.3	89.6	90.50
24	95.0	99.8	90.6	105.7	97.1	97.64
25	95.0	101.8	96.0	102.7	96.4	98.38
26	101.7	87.4	99.8	94.0	101.0	96.78
27	90.5	99.4	88.4	99.5	94.3	94.42
28	101.6	99.3	100.3	95.6	94.8	98.32
29	*					
30	82.8	85.3	79.9	86.1	83.5	83.52
31	86.0	82.7	80.5	84.9	83.2	83.46
32	80.8	78.8	76.7	75.9	76.7	77.78
33	77.0	74.7	77.2	69.1	76.3	74.86
34	84.4	80.8	86.7	82.5	81.5	83.18
35	76.2	73.1	73.0	73.3	76.0	74.32
36	*					
37	*					
38	*					
39	66.8	64.9	69.0	65.5	65.8	66.40
40	*					
41	*					
42	*					

* No Delamination

Table A7. Delamination Diameter Measurements for CP3.

Indentation Identification Number	a_1 (μm)	a_2 (μm)	a_3 (μm)	a_4 (μm)	a_5 (μm)	a_{ave} (μm)
1	153.7	148.6	135.9	135.4	142.7	143.26
2	164.0	155.5	168.5	140.0	157.4	157.08
3	194.7	191.5	189.5	184.2	191.3	190.24
4	160.2	160.3	154.9	151.7	154.6	156.34
5	165.4	166.7	159.8	158.8	164.5	163.04
6	151.1	154.6	149.8	150.8	152.8	151.80
7	152.4	166.8	160.1	159.0	157.2	159.10
8	129.7	136.4	131.6	128.2	133.9	131.96
9	150.5	160.6	145.7	151.0	153.6	152.28
10	149.0	147.7	144.9	145.6	149.4	147.32
11	127.4	135.8	124.0	134.8	130.6	130.58
12	152.0	148.2	145.7	139.4	144.2	145.90
13	177.5	165.5	160.0	178.8	177.0	171.76
14	121.5	117.3	112.9	120.4	127.4	119.90
15	140.9	141.8	147.7	129.1	139.3	139.76
16	148.3	122.7	141.8	150.4	156.8	144.0
17	171.3	174.5	184.8	167.3	166.7	172.92
18	150.2	154.8	155.3	150.5	155.5	153.26
19	150.1	153.8	161.0	141.1	146.3	150.46
20	152.2	168.7	155.6	157.2	158.0	158.34
21	143.6	151.0	133.0	143.2	138.6	141.88
22	135.2	124.7	126.1	129.8	133.3	129.82
23	152.8	157.3	147.5	141.0	157.2	151.16
24	140.4	135.5	133.5	131.9	139.8	136.22
25	134.4	136.0	133.9	131.1	128.8	132.84
26	137.9	138.9	138.1	132.8	135.7	136.68
27	122.1	130.3	125.0	122.5	120.3	124.04
28	124.4	118.7	115.6	113.2	122.1	118.80
29	148.7	147.4	135.1	140.8	144.9	143.38
30	149.1	146.7	151.5	138.5	144.4	146.04
31	137.6	142.4	132.8	130.9	139.1	136.56
32	143.7	176.1	157.8	152.4	146.1	155.22
33	148.0	156.0	152.2	144.1	144.8	149.02
34	142.8	152.0	155.3	141.0	150.2	148.26
35	168.0	163.3	151.1	172.5	164.7	163.92
36	140.7	135.7	133.8	139.1	139.7	137.80
37	121.7	114.6	105.8	115.0	122.7	115.96
38	107.9	110.6	110.7	108.8	107.2	109.04
39	121.8	131.2	119.3	118.4	119.5	122.04
40	97.5	113.3	115.5	107.3	95.5	105.82

Table A7. (continued)

Indentation Identification Number	a_1 (μm)	a_2 (μm)	a_3 (μm)	a_4 (μm)	a_5 (μm)	a_{ave} (μm)
41	147.7	146.0	155.7	146.6	145.9	148.38
42	144.9	153.0	145.9	153.3	153.5	150.12
43	170.7	153.4	150.4	164.7	174.2	162.68
44	146.9	148.6	138.6	145.5	143.4	144.60
45	130.5	134.3	122.9	130.5	131.2	129.88
46	125.5	122.7	119.6	115.2	122.8	121.16
47	114.4	119.7	116.4	110.0	108.3	113.76
48	116.8	117.3	117.0	118.0	123.1	118.44
49	83.2	96.6	84.9	84.3	79.8	85.76

Table A8. Delamination Diameter Measurements for CP6.

Indentation Identification Number	a_1 (μm)	a_2 (μm)	a_3 (μm)	a_4 (μm)	a_5 (μm)	a_{ave} (μm)
1	114.2	114.4	115.6	114.5	115.0	114.75
2	95.1	96.4	97.7	94.8	93.2	95.44
3	88.1	90.2	87.4	90.1	85.0	88.16
4	158.8	137.5	160.8	161.2	169.9	157.64
5	111.3	104.5	105.6	106.2	108.3	107.18
6	99.4	101.8	101.5	92.6	101.7	99.40
7	117.1	109.2	117.2	111.7	116.2	114.28
8	79.8	85.8	80.8	82.5	79.2	81.62
9	87.4	94.5	81.5	93.5	89.2	89.22
10	80.4	87.4	84.6	84.8	85.7	84.58
11	93.8	90.4	88.9	94.7	88.4	91.24
12	82.3	83.0	85.1	82.7	82.3	83.08
13	93.8	91.1	95.2	89.7	91.5	92.26
14	88.6	99.3	85.8	97.7	87.6	91.86
15	94.1	95.3	92.5	95.3	95.0	94.44
16	*					
17	90.3	85.3	88.2	89.7	89.2	88.54
18	104.6	106.9	106.0	102.0	104.9	104.88
19	85.2	81.0	81.4	83.1	83.5	82.84
20	67.1	65.6	68.8	65.3	64.8	66.32
21	76.1	73.7	75.7	79.2	79.3	76.80
22	90.4	85.2	85.8	86.7	87.7	87.16
23	98.0	92.2	97.2	93.4	91.0	94.36
24	83.8	88.9	83.9	85.1	83.6	85.06
25	82.5	76.6	74.9	77.9	81.6	78.70
26	91.6	87.3	93.1	92.3	88.0	90.46
27	72.8	74.2	82.3	82.6	77.2	77.82
28	*					
29	*					
30	*					

* No Delamination

Appendix A (continued)

Table A9. Radial Crack Lengths for Uncoated Silicon Specimen Si1.

Indentation Identification Number	$2c_{horz}$ (μm)	$2c_{vert}$ (μm)
1	177.4	171.5
2	170.6	174.0
3	175.2	171.2
4	167.8	162.7
5	166.4	157.5
6	168.9	190.1
7	174.2	181.8
8	189.7	184.2
9	166.5	164.8
10	179.6	163.5

Table A10. Radial Crack Lengths for Uncoated Silicon Specimen Si2.

Indentation Identification Number	$2c_{horz}$ (μm)	$2c_{vert}$ (μm)
1	122.0	110.3
2	128.0	126.0
3	118.9	86.3
4	125.8	120.1
5	131.3	121.8
6	122.5	116.3
7	94.4	116.8
8	116.9	124.9
9	121.1	109.9

Appendix B

Description of Specimen Sites Where Infrared Spectra was Obtained.

Each of the following spectral files was obtained by ratioing infrared spectra of a damaged region on a specimen to an undamaged region on the same specimen. The following list gives the spectra file name along with a description of the specimen and the damaged region studied.

1.SCZS

A disk shaped zinc sulfide specimen 3.75 mm thick was put into compression with a brass specimen holder capable of applying a compressive load to the specimen via a sliding jaw that was tightened with allen screws. The compressive loading resulted in two areas of damage on the specimen each located from the point of contact of the specimen holder to approximately 4.8 mm into the center of the specimen. Infrared spectra was obtained on one of the damaged regions centering the field of view approximately 3.0 mm from the non-chipped contact point.

2.IZS50

This 3.84 mm thick zinc sulfide specimen was indented with a 98 N load. The damaged region studied was in one of the four quadrants formed by the radial cracks and the field of

view of the infrared microscope was centered approximately at 50 microns from the edge of the diamond indentation impression.

3.NP1NI6

Diamond coated silicon specimen NDFP1 contained a cross pattern of 9.8 N Vicker's indentations. This file contains FTIR data on indentaion number 6 which had an average delamination size of 174.8 microns. During infrared data aquisition the field of view was centered on the delamination.

4.WDI11

A cross pattern of 9.8 N Vicker's indentations was also made on the diamond coated silicon specimen labeled WDF31. Infrared data contained in this file was obtained on indentation number 11, which had an average delamination size of 95.8 microns. The field of view of the infrared microscope was centered on the delamination.

5.FSI2

This precleaned non-coated silicon specimen, labeled Si2, was indented with a 9.8 N load. The infrared data was obtained by centering the infrared microscope's field of view on the diamond indentation impression for indentation number 2. The horizontal radial crack length, 2c, for this indentaion was 128.0 microns and the vertical radial crack

length was 126.0 microns.

6.FSR2

For this data, the FTIR microscope was focused on a radial crack of indentation number 2 of specimen Si2.

7.FSN2

Infrared data in this file was taken from a region in one of the four quadrants formed by the radial cracks of indentation number 2 on specimen Si2. The field of view was centered at approximately 30 microns from the edge of the diamond shaped indentation impression.

8.2ZS50

The indentation impression was polished off the specimen used to obtain the spectra IZS50. Another infrared spectra was then obtained with the center of the field of view at approximately fifty microns from the previously existing indentaion impression.

Appendix C

Transfer of Idris Data to DOS System

To retrieve data from the Idris system for use in DOS, first format a disk on a DOS system using format a:/8. On the Perkin-Elmer computer type "obey w4:transfer" and put the disk containing IR data in the left drive. The DOS formatted disk should be placed in the right drive. If the information to be transfered is a spectral file type 1 and if it is a data file type 2. Enter the filename with the extension .sp for a spectral file and .da for a data file. The file is converted into an ASCII file on the DOS formatted disk.

Appendix D.

Read1, Program Used to Read IR Data From an ASCII Format File Created by Obey w4:Transfer

```
800 REM        Program to read FTIR data files from DOS disk (in ASCII),
820 REM    and create a new data file with wavenumber, transmittance pairs
840 REM    that (1)  average the transmittance over ten consecutive
850 REM    wavenumbers, (2) record the averaged data with an abritrary
860 REM    interval of wavenumbers (presently 98 cm-1) between the centers
870 REM    of the averaged data.
880 REM
890 REM
920 L1 = 3 : L2 = 12
1020 CLS
1040 DIM T(14), LAMBDA(250),LAMB(50),DIFF(50),AVET(50)
1050 FOR F = 1 TO 15
1070   GOSUB 4000 : REM Read input file label, create output file label
1080   IF F < 15 GOTO 1400
1120   GOSUB 7300 : REM Read FTIR header data
1140   GOSUB 8000 : REM Read wavelength, transmittance data
1160   CLOSE
1200   GOSUB 9300 : REM output
1240   GOSUB 14000 : REM Output
1400   CLOSE
1600 NEXT F
1990 END
4000 REM Read input file label, create output file label
4020 EX$ = ".DAT"
4030 D$ = "."
4050   READ FTIR$
4060   X = INSTR(FTIR$,D$) : REM FIND THE LOCATION OF THE "."
4065   REM IN THE FILE NAME
4070   IF X = 0 THEN DAT$ = FTIR$ + EX$ : REM IF NO EXTENDER.
4075   REM CONCAT DIRECTLY
4080   IF X > 0 THEN DAT$ = LEFT$(FTIR$,X - 1) + EX$ :REM If there is an
         extender, remove period and concat
4090   PRINT F;"   ";FTIR$;"                    ";DAT$
4290 RETURN
7300 REM read header information on FTIR file
7315 OPEN FTIR$ FOR INPUT AS 2
7405    INPUT #2, TITLE$ :PRINT TITLE$
7420    INPUT #2, UNIT1$,UNIT2$ :PRINT UNIT1$,UNIT2$
7430    INPUT #2, XYSTART1$,XYSTART2$ :PRINT XYSTART1$,XYSTART2$
7460    INPUT #2, FINAL1$,FINAL2$ : PRINT FINAL1$,FINAL2$
7500    INPUT #2, FACTOR1$,FACTOR2$ : PRINT FACTOR1$,FACTOR2$
7520    INPUT #2, NPOINT1$,NPOINT2$ : PRINT NPOINT1$,NPOINT2$
7540    INPUT #2, SPECTRUM$ :PRINT SPECTRUM$
7590 RETURN
8000 REM
8005 N = 240 : P = 0! : SCALE = 10000! : D0 = 7!
8020 I$ = "##    ####.#    ##.#####   #####.#   ####.#"
8100 FOR J = 1 TO N
```

```
8120     INPUT #2, LAMBDA(J)
8130     IF LAMBDA(J) < 750 THEN RETURN
8140     IF J >= 2 THEN DD = (LAMBDA(J - 1!) - LAMBDA(J))/2!
8160     IF J >= 2 THEN LL = LAMBDA(J) - DD
8180     IF J = 1  THEN LL = LAMBDA(J) - DD
8220     SUM = 0 :COUNT = 0
8240     FOR K = 1 TO  14
8260        INPUT #2,T(K) : T(K) = T(K)/SCALE
8270        GOSUB 9600 : REM Average data over some interval of wavenumbers
8280     NEXT K
8290   IF J = 1 THEN GOSUB 12000: REM Calculate ave trans for first data line
8300   IF J/7! = INT(J/7!) THEN GOSUB 12000 : REM Calculate
8340 NEXT J
8390 RETURN
9300 REM read header information on FTIR file
9315 OPEN DAT$ FOR APPEND AS 1
9405     PRINT #1, TITLE$
9420     PRINT #1, UNIT1$,UNIT2$
9430     PRINT #1, XYSTART1$,XYSTART2$
9460     PRINT #1, FINAL1$,FINAL2$
9500     PRINT #1, FACTOR1$,FACTOR2$
9520     PRINT #1, NPOINT1$,NPOINT2$
9540     PRINT #1, SPECTRUM$
9560 CLOSE
9590 RETURN
9600 REM Average data over some interval of wavenumbers
9720 IF K < L1 OR K > L2 THEN RETURN
9740 SUM = SUM + T(K): REM PRINT T(K),SUM
9760 COUNT = COUNT + 1
9800 REM IF K = 12 THEN PRINT "SUM = ":SUM
9900 RETURN
12000 REM Calculate
12100 I$ = "##     ####.#     ##.#####    #####.#    ####.#"
12200  P = P + 1!
12220  AVET(P) = SUM/COUNT
12240  DIFF(P) = DD : LAMB(P) = LL
12340  PRINT USING I$:P, LAMBDA(J), AVET(P),LAMB(P),DIFF(P)
12900 RETURN
14000 REM Calculate
14020 OPEN DAT$ FOR APPEND AS 1
14100 PRINT #1,P
14200 FOR C = 1 TO P
14220      AVET(C) = AVET(C)*10!
14340      PRINT #1, AVET(C),LAMB(C)
14360 NEXT C
14500 RETURN
20000 DATA SCZS.SP
20020 DATA IZS50
20040 DATA IZS200
20060 DATA ZSE2
20080 DATA ZSE1.SP
20110 DATA NP1NI7
```

```
20120 DATA NF1NI6.SP
20140 DATA WDI11
20160 DATA FSI2
20180 DATA FSR2
20200 DATA FSN2.so
20220 DATA FSI8.sp
20240 DATA FSN8.so
20260 DATA FSR8.sp
20280 DATA r2zs.sp
```

Appendix E

Fskip, Program Used to Read the Data File Created by Read1 and Conduct a Least-Squares Fitting

```
1000 REM Program to read data file (created from DOS data file by READ1)
1010 REM   and do least-squares fitting on the data.
1040 NFILE = 11 : FF$ = "foood.dat"
1060 C2 = 2 : I2 = 35 : N = 35 : I1 = 1 : SEL = 1
1110 DIM A(C2,C2),B(C2),V(C2),D(C2,I2)
1120 DIM C(C2),Y(I2),X(I1,I2),C3(C2)
1140 DIM STATE(20),A$(15),GUESS1(NFILE),GUESS2(NFILE)
1200 GOSUB 4000  : REM READ DAT FILE LABEL FROM FILE FNAME.DAT
1220 GOSUB 19000 : REM Read guesses for parameter
1250 FOR QQ = 1 TO NFILE
1500    GOSUB 7000  : REM Read data from dat file (disk)
1520    GOSUB 8000  : REM Print data to CRT
1530    GOSUB 9000  : REM Determine number of data points, based on SEL
1540    GOSUB 15000 : REM Initialize for Least-Squares
1560    GOSUB 16000 : REM Least-squares fit
1570    GOSUB 18000 : REM Print fit parameters to guess file
1580    GOSUB 5000  : REM PRINT LEAST-SQUARES RESULTS TO FILE
1700 NEXT QQ
3000 END
4000 REM READ DAT FILE LABEL
4020 OPEN FF$ FOR INPUT AS 1
4025 FOR K = 1 TO NFILE
4030    INPUT #1, A$(K)
4035    PRINT A$(K)
4040 NEXT K
4050 CLOSE
4400 RETURN
5000 REM PRINT LEAST-SQUARES RESULTS TO FILE
5010 FF$ = "LSQ.RES"
5020 OPEN FF$ FOR APPEND AS 2
5100 RR = SQR(ABS(R3))
5230 PRINT #2, DAT$,C(1),C(2),R3,I2
5250 CLOSE
5400 RETURN
7000 REM Read averaged transmission file
7010 DAT$ = A$(QQ) : REM A$ holds the data file names (See SUB 4000)
7020 OPEN DAT$ FOR INPUT AS 2
7030    INPUT #2, TITLE$ :PRINT TITLE$
7040    INPUT #2, UNIT$ :PRINT UNIT$
7050    INPUT #2, XYSTART$:PRINT XYSTART$
7060    INPUT #2, FINAL$ : PRINT FINAL$
7070    INPUT #2, FACTOR$ : PRINT FACTOR$
7080    INPUT #2, NPOINT$ : PRINT NPOINT$
7090    INPUT #2, SPECTRUM$ :PRINT SPECTRUM$
7100 INPUT #2,P : PRINT P
7105 W = 1
```

```
7110 FOR C = 1 TO P
7120      INPUT #2, A,B : REM INPUT #2, Y(C),X(1,C)
7125      IF C/SEL = INT(C/SEL) THEN X(1,W) = B/10000 : Y(W) = A
7140      IF QQ = 3  THEN Y(W) = Y(W)*10
7160      IF QQ = 10 THEN Y(W) = Y(W)*10
7180      IF QQ = 11 THEN Y(W) = Y(W)*10
7600      IF C/SEL = INT(C/SEL) THEN W = W + 1
7730 NEXT C
7735 CLOSE
7740 RETURN
8000 REM Print trans and wavenumber information to CRT
8160 A$ = " ###    ##.####     #####.##### "
8170 FOR C = 1 TO P
8180      PRINT USING A$:C,Y(C),X(1,C)
8200 NEXT C
8210 RETURN
9000 REM Selection of I2, N based on value of SEL
9020 IF SEL = 4 THEN I2 = 8
9040 IF SEL = 3 THEN I2 = 11
9060 IF SEL = 2 THEN I2 = 16
9080 IF SEL = 1 THEN I2 = 34
9100 N = I2
9120 REM Specification of additional parameters
9140 I1 = 1 : REM i1 = number of indedepent variables
9160 C2 = 2 : REM C2 = NUMBER OF FITTING VARIABLES
9900 RETURN
15000 REM Initialize parameters for least-squares procedure
15020 FOR GGG = 1 TO C2
15030   C3(GGG) = 0! : C(GGG) = 0! : B(GGG) = 0! : V(GGG) = 0!
15035 NEXT GGG
15040 RRR = 0! : R2 = 0!: Y5 = 0!
15060 R3 = 0! : V = 0!
15080 V1 = 0! : V2 = 0! : V3 = 0!
15120 OKAY = .95
15140 ITERATION = 10
15200 RETURN
16000 REM
16003 REM C2 = 2 : I2 = 34 : N = 34 : I1 = 1
16010 C1=.000001 : REM c1 is a convergence parameter
16050 REM GOSUB 19000 : REM ReAD initial guess
16160 C(1) = GUESS1(00)  :  C(2) = GUESS2(00)
16180 REM
16200 DEF FNY(I)= C(1)*EXP(-X(1,I)*C(2))
16205 REM DEF FNY(I)= C(1) + C(2)/((1! + C(3)*X(1,I)*X(1,I))^2)
16210 DEF FNW(I)=1
16230 GOSUB 17310
16240 REM
16245 FOR LL=1 TO ITERATION
16250 GOSUB 16310
16260 GOSUB 16420
16270 GOSUB 16540
16280 GOSUB 16660
16290 GOSUB 17070
```

```
16300 NEXT LL
16305 REM
16310 REM calculating the derivative
16320  FOR K=1 TO C2
16330   FOR I=1 TO I2
16340   Y=FNY(I)
16350   C(K)=C(K)*(1.001)
16360   Y5=FNY(I)
16370   D(K,I)=(Y5-Y)/(C(K)*.001)
16380   C(K)=C(K)/1.001
16390   NEXT I
16400  NEXT K
16410 RETURN
16420 REM first initialize the [a] and [b] matrices
16430  FOR K=1 TO C2
16440   FOR J=1 TO C2
16450   B(J)=0 : A(J,K)=0
16460   NEXT J
16470  NEXT K
16480  FOR J=1 TO C2
16490   FOR I=1 TO I2
16500   B(J)=B(J)+(Y(I)-FNY(I))*D(J,I)
16510   NEXT I
16520  NEXT J
16530 RETURN
16540 REM calculating the sums for the
16550  FOR K=1 TO C2
16560   FOR J=1 TO C2
16570    FOR I=1 TO I2
16580    A(K,J)=A(K,J)+FNW(I)*D(K,I)*D(J,I)
16590    NEXT I
16600   NEXT J
16610  NEXT K
16620  FOR J=1 TO C2
16630  A(J,J)=(A(J,J))*(1+C1)
16640  NEXT J
16650 RETURN
16660 N=C2 : Q=0 : V=0
16670 N1=N-1 : J=1
16680  FOR I=1 TO N1
16690  L1=0
16700   FOR P=1 TO N
16710   G=ABS(A(P,I))
16720   IF(G>L1)THEN L1=G : J=P
16730   NEXT P
16740  IF(L1=0)THEN I=N1 : NEXT I
16750 IF(L1=0)THEN RETURN
16760  FOR K=I TO N
16770  T1=A(I,K)
16780  A(I,K)=A(J,K)
16790  A(J,K)=T1
16800  NEXT K
```

```
16810 T1=B(1)
16820 REM
16830 B(I)=B(J)
16840 B(J)=T1
16850 I5=I+1
16860  FOR K=I5 TO N
16870  Q=-A(K,I)/A(I,I)
16880  A(K,I)=0
16890  B(K)=Q*B(I)+B(K)
16900   FOR J=I5 TO N
16910   A(K,J)=Q*A(I,J)+A(K,J)
16920   NEXT J
16930  NEXT K
16940 REM NEXT I
16950 IF(A(N,N))=0 THEN RETURN
16960 V(N)=B(N)/A(N,N)
16970 N6=N+1
16980  FOR K=1 TO N1
16990  Q=0
17000  N5=N-K
17010   FOR J=1 TO K
17020   Q=Q+A(N5,N6-J)*V(N6-J)
17030   NEXT J
17040  V(N5)=(B(N5)-Q)/A(N5,N5)
17050 NEXT K
17060 RETURN
17070 REM update coefficients c(i) and print results
17080 PRINT" "
17090  FOR I=1 TO C2
17100  C(I)=C(I)+V(I)
17110  PRINT"c(",I,")=",C(I)
17120  NEXT I
17130 REM calculating the variance
17140  FOR I=1 TO I2
17150  V=V+FNW(I)*(Y(I)-FNY(I))^2
17160  NEXT I
17170 REM r2 is the sqr of the correlation coefficient
17180 R2=1-(V/I2/V5)
17190 PRINT"corr. coeff. sqr",R2
17200 IF R2<R3 THEN 17250
17210  FOR J1=1 TO C2
17220  C3(J1)=C(J1)
17230  NEXT J1
17240 R3=R2
17250 PRINT"best so far",R3
17260  FOR I=1 TO C2
17270  PRINT"c(i)",I,")= ",C3(I)
17280  NEXT I
17290 PRINT" " : PRINT"best fit corr. sqr=",R3
17300 RETURN
17310 REM
17320  FOR R=1 TO I2
```

```
17330       REM READ Y(R),X(1,R)
17340  NEXT R
17350 REM std dev of y's
17360  FOR I=1 TO I2
17370  V1=Y(I)+V1 : V2=Y(I)^2+V2
17380  NEXT I
17390 V5=V2/I2-(V1/I2)^2
17400 RETURN
18000 REM Record fit as initial guess
18100 GUESS(1) = C(1) : GUESS(2) = C(2)
18110 FILE$ = "guess"
18120 OPEN FILE$ FOR APPEND AS 3
18140 PRINT #3,C(1),C(2)
18200 CLOSE
18400 RETURN
19000 REM Record fit as initial guess
19110 FILE$ = "og"
19120 OPEN FILE$ FOR INPUT AS 3
19140 FOR Z = 1 TO NFILE
19160     INPUT #3, GUESS1(Z),GUESS2(Z)
19170     GUESS1(Z) = 10!*GUESS1(Z) : GUESS2(Z) = GUESS2(Z)
19180 NEXT Z
19200 CLOSE
19400 RETURN
```

REFERENCES

1. Brown, A. S., Aerospace America, 25 [11], 12-37, 1987.

2. Pellicori, S. F., Photonics Spectra, 23 [10], 165-167, 1987.

3. Beaver, M. B., Encyclopedia of Materials Science and Engineering, MIT Press, Massachusetts, 2, 1139, 1986.

4. Angus, J. C., and Hayman, C. C., Science, 241, 913-921, 1988.

5. Deshpandey, C. V., and Bunshah, R. F., J. Vac. Sci. Technol. A, 7 [3], 2294-2302, 1989.

6. Berman, R., Physical Properties of Diamond, Oxford University Press, London, 1965.

7. DeVries, R. C., Ann. Rev. Mater. Sci., 17, 161-187, 1987.

8. Bridgman, P. W., Sci. Am., 193, 42, 1955.

9. Messier, R., Spear, K. E., Badzian, A. R., and Roy, R., Journal of Metals, 39, [9], 8-11, 1987.

10. Matsumoto, S., Sato, Y., Kamo, M., Setaka, N., Jpn. J. of Appl. Phys., 21, 183, 1982.

11. Deryagin, B. V., Fodoseovev, D. V., Lukynovich, V. M., Spitsyn, V. M., Ryabov, V. A., and Lavrenterv, A. V., J. Cryst. Growth, 2, 380, 1968.

12. Matsumoto, S. and Matsui, Y., J. Mater. Sci., 18, 1785, 1983.

13. Yarbrough, W. A., and Messier, R., Science, 247, 688-696, 1990.

14. Kobashi, K., Nishimura, K., Kawate, K., Horuchi, T., Phys. Rev. B, 38, 4067, 1988.

15. Hirabayashi, K., Ikoma, K., Taniguci, Y., Kurihara, N. I., First International Conference on the New Diamond Science and Technology, Program and Abstract, October 24-26 1988, (JNDF, Tokyo, 1988), 96-97, as cited in [13].

16. Ravi, K. V., Peters, M., Plano, L., Yokota, S., Pinneo, M., First International Conference on the New Diamond Science and Technology, Program and Abstract, October 24-26 1988, (JNDF, Tokyo, 1988), 32-33 as cited in [13].

17. Yugo, S., and Kimura, T., First International Conference on the New Diamond Science and Technology, Program and Abstracts, October 24-26 1988, (JNDF, Tokyo, 1988), 130-131 as cited in [13].

18. Yarbrough, W. A., Kumar, A., Roy, Rustum, paper presented at the fall meeting, Materials Research Society, November 31-December 5 1989, Boston, MA, as cited in [13].

19. Mitsuda, Y., Kojima, Y., Yoshida, T., and Akashi K., J. Mater. Sci. Lett. , 6, 1557-1562, 1987.

20. Karawada, H., Mar, K. S., Suzuki, J., Ito, T., Mori, H., Fujita, H., and Hiraki, A., Jpn. J. Appl. Phys., 26 [11], L1903-L1906, 1987.

21. Williams, B. E., and Glass J. T., J. Mater. Res., 4 [2], 373-384, 1989.

22. Knight, D. S., and White, W. B., J. Mater. Res., 4 [2], 385-393, 1989.

23. Matsui, Y., Matsumoto, S., and Setaka, N., J. Mater. Sci. Lett., 2, 532-534, 1983.

24. Vitkavage, D. J., Rudder, R. A., Fountain, G. G., and Markunas, R. J., J. Vac. Sci. Technol. A, 6 [3], 1812-1815, 1988.

25. Setaka, N., J. Mater. Res., 4 [3], 664-670, 1989.

26. Celii, F. G., Pehrsson, P. E., Wang, H. -t., and Butler J. E., Appl. Phys. Lett, 52 [24], 2043-2045, 1988.

27. Frenklach, M. and Spear, K. E., J. of Mater. Res., 3, 133, 1987.

28. Chen, C., Huang, Y. C., Hosomi, S., Yoshida, I., Mat. Res. Bull., 24, 87-94, 1989.

29. Valli, J., J. Vac. Sci. Technol. A, 4 [6], 3007-3014, 1986.

30. Bray, R. C., Quate, C. F., Calhoun, J., and Koch, R., Thin Solid Films, 74, 295, 1980.

31. Loh, R. L., Rossington, C., and Evans, A. G., J. Amer. Ceram. Soc., 69 [2], 139-142, 1986.

32. Burnett, J., and Rickerby, D. S., J. Mater. Sci., 23, 2429-2443, 1988.

33. Scaglione, S., and Emiliani G., J. Vac. Sci. Technol. A, 7 [2], 2303-2306, 1989.

34. Clarke, D. R., and Wolf, D., Materials Science and Engineering, 83, 197-204, 1986.

35. Argon, A. S., Gupta, V., and Cornie, J. A., Materials Science and Engineering, A107, 41-47, 1989.

36. Argon, A. S., Gupta, V., Landis, H. S., Cornie, J. A., J. Mater. Sci., 24, 1207-1218, 1989.

37. Hu, M. S., Thouless, M. D., Evans, A. G., Acta Metall., 36 [5], 1301-1307, 1988.

38. Evans, A. G., Drory, M. D., and Hu, M. S., J. Mater. Res., 3 [5], 1043-1049, 1988.

39 Marshall, D. B., and Evans, A. G., J. Appl. Phys., 56 [10], 2632-2638, 1984.

40. Rossington, C., Evans, A. G., Marshall, D. B., and Khuri-Yakub, B. T., J. Appl. Phys., 56 [10], 2639-2644, 1984.

41. Evans, A. G., and Hutchinson, J. W., Int. J. Solids Structures, 20 [5], 455-466, 1984.

42. Matthewson, M. J., Appl. Phys. Lett., 49 [21], 1426-1428, 1986.

43. Van Der Zwaag, S. and Field, J. E., J. Mater. Sci., 17, 2625-2636, 1982.

44. Case, E. D., Evans, A. G., and Louie, K. M. "Water Impact Damage by Fourier Transform Spectroscopy", Progress Report to Office of Naval Research, July 1985.

45. Case, E. D., Associate Professor, Deparment of Metallurgy Mechanics and Materials Science, Michigan State University, East Lansing, MI, a personal communication, 1990.

46. Debye, P. and Bueche, A. M., J. Appl. Phys., 20, 518-526, 1949.

47. Ohanian, H. C., Physics, W. W. Norton and Co., Inc., New York, 805, 1985.

48. Fowles, R. Introduction to Modern Optics, Holt, Rinehart, and Winston, Inc., New York, 40-45, 1975.

49. McGraw-Hill Encyclopedia of Science and Technology, 15, McGraw-Hill, Inc., 244-247, 1987.

50. Kingery, W. D., Bowen, H. K., and Uhlmann, D. R., Introduction to Ceramics, John Wiley and Sons, Inc., New York, 652-655 & 822-830, 1976.

51. Klein, M. V., Optics, John Wiley and Sons, Inc., New York, 579-581, 1970.

52. McGraw-Hill Encyclopedia of Science and Technology, 1, McGraw-Hill, Inc., 18-24, 1987.

53. Bohren, C. F. and Huffman, D. R., Absorption and Scattering of Light by Small Particles, John Wiley and Sons, Inc., New York, 7-9, 1983.

54. Haraoh, T., Ishikawa, H., Shinkai, N., Mizuhashi, M., J. Mater. Sci., 17, 1493-1500, 1982.

55. Marshall, D. B., Lawn, B. R., and Evans, A. G., J. Amer. Ceram. Soc., 65, 561-566, 1982.

56. Kodre, A. and Strand, J., Amer. J. Phys., 44[2], 181-182, 1976.

57. Case, E. D., Louie, K. M., and Evans, A. G., J. Mater. Sci. Letters, 3, 879-884, 1984.

58. McGraw-Hill Encyclopedia of Science and Technology, 9, McGraw-Hill, Inc., 52-58, 1987.

59. Griffiths, P. R., Chemical Infrared Fourier Transform Spectroscopy, John Wiley and Sons, Inc., New York, 166-169, 1975.

60. Hasselman, D. P. H., J. Amer. Ceram. Soc., 52 [11], 600-604, 1969.

61. Hasselman, D. P. H., J. Amer. Ceram. Soc., 46 [11], 535-540, 1963.

62. Gupta, T. K., J. Amer Ceram. Soc., 55 [5], 249-253, 1972.

63. Matsushita, K., Kuratani, S., Okamoto, T., Shimada, M., J. Mater. Sci. and Letters, 3, 345-348, 1984.

64. Lee, W. J. and Case, E. D., Mater. Sci. and Eng. A, 119, 113-126, 1989.

65. Kern, W. and Puotinen, D. A., RCA Review, 31, 187, 1970.

66. Root, J. and Asmussen, J., Rev. Sci. Instrum., 57(8), 1511-1519, 1985.

67. Roppel, T., Reinhard, D. K., and Asmussen, J., J. Vac. Sci. Technol. B, 4(1), 295-298, 1986.

68. Huang, B., Thesis Proposal, Department of Electrical Engineering, Michigan State University, 1989.

69. Delong, J., Use of the Perkin-Elmer model 1850 FTIR, November, 1988.

70. Perkin-Elmer Model 1800 Series FTIR Manual.

71. Gray, Kevin, Norton Diamond Technology Center, Norton Company, Northboro, Massachusettes, 1990.

72. Hook, Kevin, Composite Materials and Structures Center, Michigan State University, personal communication 1990.

73. Mizokawa, Y., Miyasto, T., Nakamura, S., Geib, K., and Wilmsen, C. W., J. Vac. Sci. Technol., A5, 2809-2813, 1987.

74. Lawn, B. R., Fracture Mechanics of Ceramics, vol. 5, Bradt, R. C., Evans, A. G., Hasselman, D. P. H., and Lange, F. F. eds., Plenum Press, New York, 1-26, 1983.

75. Wiederhorn, S. M. and Ritter, J. E., Fracture Mechanics Applied to Brittle Materials, A.S.T.M. 678, 202, Philadelphia, 1979.

76. Carniglia, S. C., J. Amer. Ceram. Soc., 55 [5], 243-249, 1972.

77. Biswas, Dipak R., Fulrath, Richard M., J. Mater. Sci., 14, 2721-2725, 1979.

78. Good, Roland H. Jr., Nelson, Terence J., Classical Theory of Electric and Magnetic Fields, Academic Press, New York, 380-383, 1971.

79. White, Grady S., Machiando, J. F., Applied Optics, 22 [15], 2308-2312, 1983.

80. Maystre, D., IEEE Antenn, 31 [6], 885-895, 1983.